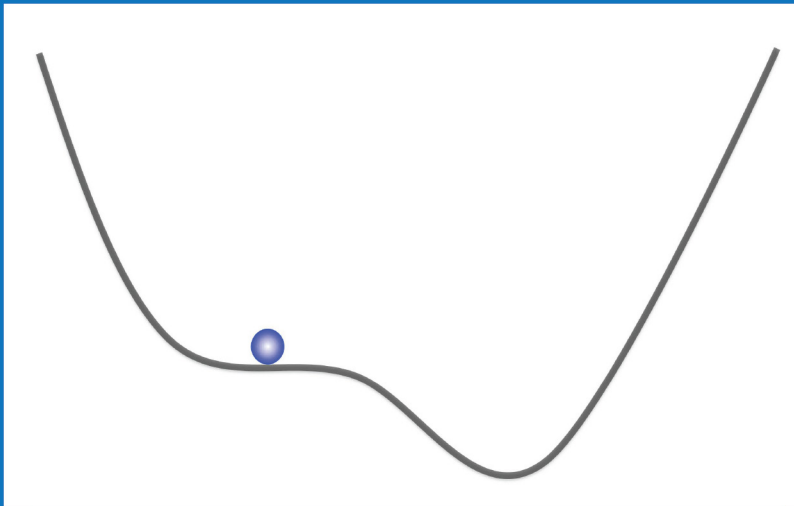


# **Instability,**

the driving force for new physical phenomena



**Zhicheng Zhong**

**INSTABILITY,  
THE DRIVING FORCE FOR NEW PHYSICAL PHENOMENA**

Zhicheng Zhong

## Composition of the Graduation Committee

Prof. Dr. G. van der Steenhoven	University of Twente, Chairman
Prof. Dr. P. J. Kelly	University of Twente, Promoter
Prof. Dr. Ing. A. J. H. M. Rijnders	University of Twente
Prof. Dr. Ir. A. Brinkman	University of Twente
Prof. Dr. Ir. W. G. van der Wiel	University of Twente
Prof. Dr. M. Golden	University of Amsterdam
Prof. Dr. S. Satpathy	University of Missouri

This work was supported by NanoNed, a nanotechnology programme of the Dutch Ministry of Economic Affairs. The use of supercomputer facilities was sponsored by the Stichting Nationale Computer Faciliteiten (NCF) which is financially supported by the Nederlandse Organisatie voor Wetenschappelijk Onderzoek (NWO)

The work described in this thesis is carried out at the Computational Materials Science (CMS) Group, Faculty of Science and Technology (TNW) and the MESA<sup>+</sup> Institute for Nanotechnology of the University of Twente (UT).

Instability, the driving force for new physical phenomena

Zhicheng Zhong

Ph. D. Thesis University of Twente, Enschede

ISBN/EAN: 978-90-365-3253-2

DOI: 10.3990/1.9789036532532

© Zhicheng Zhong, 2011

Printed by: Gildeprint Drukkerijen BV, Enschede, The Netherlands

---

**INSTABILITY,  
THE DRIVING FORCE FOR NEW PHYSICAL PHENOMENA**

DISSERTATION

to obtain  
the degree of doctor at the University of Twente,  
on the authority of the rector magnificus,  
Prof. Dr. H. Brinksma,  
on account of the decision of the graduation committee,  
to be publicly defended  
on Wednesday 12<sup>th</sup> of October 2011 at 16:45

by

**Zhicheng Zhong**

born on December 18<sup>th</sup>, 1982  
in Xinshao county, P. R. China

This doctoral dissertation is approved by:

Prof. Dr. P. J. Kelly      Promoter

This work is dedicated to my wife Yanhui  
to our daughters  
and to my parents



# Contents

<b>1</b>	<b>Introduction</b>	<b>1</b>
1.1	Topics . . . . .	1
1.2	Strategy of my research . . . . .	2
1.3	Density functional theory . . . . .	4
1.3.1	Schrödinger equation . . . . .	4
1.3.2	Kohn-Sham equation . . . . .	4
1.3.3	Exchange-correlation functionals . . . . .	6
1.4	Outlook of this thesis . . . . .	7
<b>2</b>	<b>Bulk perovskite oxides</b>	<b>11</b>
2.1	Perovskite structures . . . . .	11
2.1.1	Cubic structure . . . . .	12
2.1.2	Distorted structure . . . . .	12
2.2	Bulk SrTiO <sub>3</sub> and LaAlO <sub>3</sub> . . . . .	14
2.3	Bulk LaTiO <sub>3</sub> . . . . .	16
2.3.1	Distorted structure . . . . .	16
2.3.2	Influence of distortion on electronic structure . . . . .	17
2.3.3	Single band description . . . . .	20
2.3.4	The distortion is predictable . . . . .	21
2.4	Summary . . . . .	22
<b>3</b>	<b>LaAlO<sub>3</sub> SrTiO<sub>3</sub> interfaces</b>	<b>23</b>
3.1	Introduction . . . . .	23
3.2	Outline . . . . .	25
3.3	Multilayers of LaAlO <sub>3</sub>  SrTiO <sub>3</sub> . . . . .	25
3.3.1	Polar instability . . . . .	26
3.3.2	Charge transfer and atomic relaxation . . . . .	28
3.3.3	Thickness dependence . . . . .	29
3.4	LaAlO <sub>3</sub> thin films grown on a SrTiO <sub>3</sub> substrate . . . . .	30
3.5	The Interface can not be ideal . . . . .	32
<b>4</b>	<b>Polarity-induced oxygen vacancies at LaAlO<sub>3</sub> SrTiO<sub>3</sub> interfaces</b>	<b>35</b>
4.1	Introduction . . . . .	35
4.2	Method . . . . .	36
4.3	Results . . . . .	38



4.3.1	Parallel capacitor model . . . . .	39
4.3.2	Atomic relaxation . . . . .	39
4.3.3	Critical thickness . . . . .	40
4.3.4	Electronic structure . . . . .	41
4.4	Discussion . . . . .	42
4.5	Conclusion . . . . .	43
<b>5</b>	<b>Electronic-structure-induced reconstruction and magnetic ordering at the LaAlO<sub>3</sub> SrTiO<sub>3</sub> interface</b>	<b>45</b>
5.1	Introduction . . . . .	45
5.2	Method . . . . .	46
5.3	Results . . . . .	47
5.3.1	Electronic structure . . . . .	47
5.3.2	Atomic structure . . . . .	49
5.3.3	Discussion . . . . .	50
5.4	Summary and conclusions . . . . .	51
<b>6</b>	<b>Prediction of thickness limits of ideal polar ultrathin films</b>	<b>53</b>
6.1	Introduction . . . . .	54
6.2	Method . . . . .	54
6.3	Results . . . . .	55
6.3.1	Critical thickness of ACuO <sub>2</sub> ultrathin films . . . . .	55
6.3.2	Atomic and electronic structure . . . . .	59
6.4	Conclusion . . . . .	60
<b>7</b>	<b>Magnetic phase diagram of FeAs based superconductors</b>	<b>61</b>
7.1	Introduction . . . . .	61
7.2	Method . . . . .	62
7.3	Results . . . . .	63
7.3.1	Effect of doping . . . . .	64
7.3.2	Density of states driven phase transition . . . . .	65
7.3.3	Effect of $a$ and $d_{\text{Fe-As}}$ . . . . .	65
7.4	Conclusion . . . . .	66
<b>8</b>	<b>Understanding the spin Seebeck effect</b>	<b>69</b>
8.1	Spin Voltage . . . . .	71
8.2	Definition of magnetization potential $H_s^*$ . . . . .	72
8.2.1	Thermodynamic Force . . . . .	72
8.2.2	Difficulties . . . . .	73
8.3	Two-state model system . . . . .	74
8.3.1	Entropy . . . . .	74
8.3.2	Special cases . . . . .	76
8.4	Free electron gas model system . . . . .	77
8.4.1	Equilibrium . . . . .	77
8.4.2	Nonequilibrium . . . . .	80

8.5	Generalized Valet-Fert equation . . . . .	81
8.5.1	Boltzmann Equation . . . . .	81
8.5.2	Differences . . . . .	82
8.6	Summary . . . . .	83
<b>A</b>	<b>Free electron gas model system</b>	<b>85</b>
<b>B</b>	<b>Generalized Valet-Fert Equation</b>	<b>91</b>
	<b>Bibliography</b>	<b>93</b>
	<b>Summary</b>	<b>105</b>
	<b>Acknowledgements</b>	<b>107</b>
	<b>List of publications</b>	<b>109</b>
	<b>Curriculum vitae</b>	<b>111</b>



# Chapter 1

## Introduction

### 1.1 Topics

A central goal of modern materials physics and nanoscience is to control materials at atomic or nano scale precision. In attempting to do so, various new physical phenomena emerge. In this thesis, the following three topics are studied: (1) a conducting interface between two insulating perovskite oxides, (2) FeAs based superconductors, and (3) the spin Seebeck effect.

In 2004, Ohtomo and Hwang found that a  $\text{TiO}_2|\text{LaO}$  interface between two insulating perovskite oxides  $\text{LaAlO}_3$  (LAO) and  $\text{SrTiO}_3$  (STO) was metallic with a high carrier mobility [1]. This interface continues to attract much attention with reports that it can be conducting, magnetic or even superconducting. In contrast to the striking experimental observations, the physical origin of this metallic behavior is still the subject of intense debate. Two types of doping mechanisms are proposed to account for the conducting behavior: pure charge transfer or the formation of oxygen vacancies and other defects. There is experimental support for both mechanisms but conclusive evidence is missing. A major task of our theoretical study is to find a single framework that can naturally reconcile apparently conflicting evidence for these two doping mechanisms.

In 2008, Kamihara *et.al.* reported superconductivity in electron doped  $\text{La}[\text{O}_{1-x}\text{F}_x]$  FeAs with a critical temperature  $T_c$  of 26K [2]. It stimulated a massive experimental and theoretical effort to find other, higher- $T_c$  materials in this completely new family of iron-pnictide superconductors. The undoped parent compound  $\text{LaOFeAs}$  is a poor metal with an ordered antiferromagnetic (AFM) ground state but with increasing F doping the magnetic ordering is suppressed and superconductivity emerges. This strongly suggests that magnetic fluctuations in the iron layers close to the quantum critical point play a fundamental role in the superconducting pairing mechanism. In view of this, so far empirical, correlation between superconductivity and magnetism, it is important to understand how the magnetic (in)stability depends on structural and chemical parameters that are accessible to experiment. That is the subject of chapter 7 of the thesis.

The ordinary Seebeck effect refers to the generation of an electric voltage by

placing a non-magnetic metal in a temperature gradient. In 2008, Uchida *et.al.* carried out an experiment extending the Seebeck effect to spins [3]. According to their observations, a long-range, pure spin voltage is generated inside a ferromagnetic  $\text{Fe}_{19}\text{Ni}_{81}$  alloy (permalloy) thin film when a temperature gradient is applied. The key issue is to understand how a thermally induced spin voltage can persist up to 1 millimeter even though the well-accepted spin flip diffusion length is less than 10 nanometer for permalloy and any spin accumulation should vanish on this length scale.

## 1.2 Strategy of my research

In the topics mentioned above, the physical phenomena cover various aspects of physics, including interface conductivity, superconductivity and long-range spin voltage. The associated materials are oxides, iron-pnictides and permalloy. In spite of the materials being very different, the topics have a common feature: the new physical phenomena arise from tuning existing materials. Tuning some internal or external parameters of materials will lead to phase transitions, and consequently the materials will exhibit essentially new properties. In this thesis, the tunable parameter is a general concept, including making an interface, doping, and applying pressure, an electric field or a temperature gradient. For example,

- In the case of LAO thin films grown on a STO substrate, both starting bulk materials are well-known band insulators with perovskite structure. An insulator-metal transition can be induced by applying an external electric field or by increasing the thickness of the LAO layer.
- Undoped LaOFeAs is a poor metal with an ordered antiferromagnetic ground state. With increasing F doping the magnetic ordering is suppressed and superconductivity emerges.
- Permalloy  $\text{Fe}_{19}\text{Ni}_{81}$  is a conventional ferromagnetic metallic alloy. A long range spin voltage is generated by applying a temperature gradient.

We describe this common feature in a more general way, shown schematically in Figure 1.1. In a steady (time independent) system, the free energy  $F$  of materials with

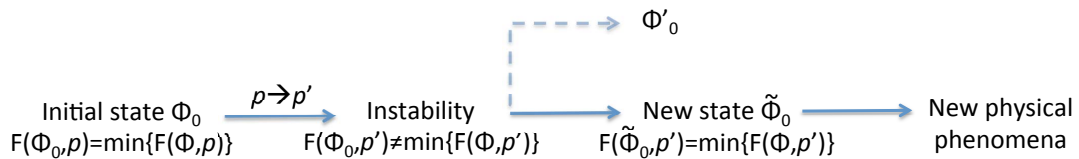


Figure 1.1: Strategy of my studies: looking for new states  $\tilde{\Phi}_0$ .  $F(\Phi)$  denote free energies;  $\Phi_0$  denote initial states;  $\tilde{\Phi}_0$  denote new states;  $p$  denotes tunable internal or external parameters of materials

parameter  $p$  can be defined as  $F(\Phi, p) = E(\Phi, p) - T \cdot S(\Phi, p)$ , where  $E$  denotes total energy,  $T$  denotes temperature,  $S$  denotes entropy, and  $\Phi$  denotes electronic and atomic states determining properties of materials.  $F$ ,  $E$  and  $S$  are functions of  $\Phi$  and parameter  $p$ . The entire system reaches thermodynamic equilibrium and becomes stable only with a specific  $\Phi_0$  that can minimize the free energy  $F(\Phi_0, p) = \min\{F(\Phi, p)\}$  according to the second law of thermodynamics. In principle,  $\Phi_0$  is a complicated thermodynamic and statistical quantity at finite temperature. At zero temperature,  $T=0$ , the entropy term does not contribute to the free energy,  $\Phi_0$  is the ground state and  $F$  is the total ground state energy of the system. In this thesis,  $\Phi_0$  actually represents either initial insulating states of STO and LAO, an AFM state of LaOFeAs, or a uniform magnetization state of permalloy in equilibrium.

Now, we tune some parameter from  $p$  to  $p'$ . For the new parameter value  $p'$ , the initial state  $\Phi_0$  no longer minimizes the free energy,  $F(\Phi_0, p') > \min\{F(\Phi, p')\}$ . Therefore it becomes energetically unfavorable and the free energy minimization principle forces the initial state to change. When the free energy is not strongly affected by parameter  $p$ , a slight modification of the initial state can minimize the free energy, resulting in a state  $\Phi'_0$  with essentially the same properties; however, when the free energy critically depends on the tuning parameter, we should consider possible new states  $\tilde{\Phi}_0$  which can efficiently lower and minimize the free energy. If  $F(\tilde{\Phi}_0, p') < F(\Phi'_0, p')$ , we propose that a transition from  $\Phi'_0$  to  $\tilde{\Phi}_0$  may occur and new physical phenomena emerge.

We summarize the common feature of all topics. The starting materials are well-studied with an initial ground state  $\Phi_0$ , exhibiting specific properties. Tuning some parameter would lead to an instability of  $\Phi_0$  and favor new states  $\tilde{\Phi}_0$  and new physical phenomena. This common feature leads to a basic strategy of my studies:

- First, we try to obtain a thorough and comprehensive understanding of initial states  $\Phi_0$  of the starting materials.
- Second, we try to figure out how tuning a parameter would result in an instability of the initial state.
- Third, this understanding should help us to look for possible new states  $\tilde{\Phi}_0$  that can resolve the instability and consequently minimize the free energy.

In order to judge the stability of these new states, we need to calculate their respective free energies  $F(\tilde{\Phi}_0)$ . In chapter 2-7, since we focus on the properties at zero temperature, the free energy reduces to the ground state total energy. We use first-principles density functional theory (DFT) discussed below to calculate the total energies and interpret our results by using analytical models. In chapter 8, we use a semiclassical thermal and statistical method to study the entropy contribution to the free energy.

## 1.3 Density functional theory

### 1.3.1 Schrödinger equation

The microscopic description of the physical and chemical properties of materials is a complex problem. Any material can be generally regarded as a collection of electrons and nuclei interacting through Coulomb (electrostatic) forces. In principle, the properties of a material consisting of  $N$  electrons and  $M$  nuclei can be derived by solving the many-body Schrödinger equation:

$$H\Psi(\mathbf{r}_1, \mathbf{r}_2, \dots, \mathbf{r}_N; \mathbf{R}_1, \mathbf{R}_2, \dots, \mathbf{R}_M) = E\Psi(\mathbf{r}_1, \mathbf{r}_2, \dots, \mathbf{r}_N; \mathbf{R}_1, \mathbf{R}_2, \dots, \mathbf{R}_M)$$

where  $H$  denotes the Hamiltonian operator,  $E$  is the total energy of the system under study,  $\Psi$  is the many-body wavefunction with electronic  $\mathbf{r}_i$  and nuclear  $\mathbf{R}_i$  coordinates.

The problem can be simplified by making the Born-Oppenheimer approximation, in which the electrons and nuclei are decoupled. The nuclear degrees of freedom appear only in the form of a potential  $V_{ext}(\mathbf{r})$  acting on the electrons, so that the wavefunction depends only on the electronic coordinates. The approximation is possible because nuclei are much heavier than electrons. We now need to solve a many-electron Schrödinger equation:

$$\left[ -\frac{1}{2} \sum_i \nabla_i^2 + \sum_{i \neq j} \frac{1}{|\mathbf{r}_i - \mathbf{r}_j|} + V_{ext}(\mathbf{r}) \right] \Psi(\mathbf{r}_1, \mathbf{r}_2, \dots, \mathbf{r}_N) = E\Psi(\mathbf{r}_1, \mathbf{r}_2, \dots, \mathbf{r}_N)$$

The first term is the kinetic energy operator, the second term is the electron-electron interaction and the third term describes the electron-ion interaction.

### 1.3.2 Kohn-Sham equation

Density functional theory (DFT), developed by Kohn and collaborators in the 1960s [4, 5], is one of the most successful approaches to solve the many-electron problem. The central statement of the DFT (the first Hohenberg-Kohn theorem) is that the exact ground state energy of an interacting many-body system can be expressed as a unique functional of its electron density  $n(\mathbf{r})$ ,

$$E[n(\mathbf{r})] = T[n(\mathbf{r})] + \int d\mathbf{r} n(\mathbf{r}) V_{ext}(\mathbf{r}) + \frac{1}{2} \iint d\mathbf{r} d\mathbf{r}' \frac{n(\mathbf{r})n(\mathbf{r}')}{|\mathbf{r} - \mathbf{r}'|} + E_{xc}[n(\mathbf{r})]$$

The terms on the right hand side describe, from left to right, the kinetic energy of the electrons, the potential energy due to the electron-ion interaction, the Hartree energy from the Coulomb interaction between electrons, and the exchange-correlation energy. In principle, the ground state energy as well as the electron density can be obtained by minimizing the functional with respect to the electron density under the constraint of conserved number of electrons (The second Hohenberg-Kohn theorem). Unfortunately, two terms are unknown: the kinetic energy functional  $T[n(\mathbf{r})]$  and the exchange-correlation energy functional  $E_{xc}[n(\mathbf{r})]$ .

$$\left[ -\frac{1}{2} \nabla^2 + V_{ext}(\mathbf{r}) + \underbrace{\int d\mathbf{r}' \frac{n(\mathbf{r}')}{|\mathbf{r}-\mathbf{r}'|}}_{\text{Effective potential}} + V_{xc}(\mathbf{r}) \right] \varphi_i(\mathbf{r}) = \varepsilon_i \varphi_i(\mathbf{r})$$

all-electron  
 pseudopotential

LDA+U  
 GGA  
 LDA

non-relativistic  
 relativistic

atomic orbitals  
 plane waves

Figure 1.2: The Kohn-Sham equation and some of its choices

Kohn and Sham next suggested a practical scheme to minimize the total energy density functional [5]. In particular, the exact kinetic energy functional  $T[n(\mathbf{r})]$  is replaced by the counterpart of a reference system consisting of non-interacting electrons with the same ground state density as that of a real system. Their difference is merged into the exchange-correlation energy. This treatment actually reduces the many-electron problem to the problem of non-interacting electrons moving in an effective potential, which is described by the so-called Kohn-Sham equations. As shown in Figure 1.2, we list some choices of the KS equation,

- The treatment can be based on the Schrödinger equation (nonrelativistic) or based on the Dirac equation (relativistic) which includes spin-orbit coupling.
- Core electrons can be treated explicitly in all-electron calculations or incorporated, together with  $V_{ext}(\mathbf{r})$ , in a pseudopotential.
- Many choices are available for the exchange-correlation potential that is defined as the functional derivative of the exchange-correlation energy,  $V_{xc}(\mathbf{r}) = \delta E_{xc}[n(\mathbf{r})]/\delta n(\mathbf{r})$ .
- The single-particle wavefunction  $\varphi_i(\mathbf{r})$  can be expanded in many types of suitable basis such as atomic orbitals or plane waves. The electron density is obtained by filling the single-electron states,  $n(\mathbf{r}) = \sum f_i |\varphi_i(\mathbf{r})|^2$ , where  $f$  is the Fermi-Dirac distribution function.

So far, we have reduced the initial  $N$ -electron problem to  $N$  one-electron problems. This reduction greatly simplifies the computational effort. A simple estimate of the reduction is to imagine a real-space representation of the wavefunction  $\Psi$  on a mesh, in which each coordinate is discretized by using 20 mesh points. For  $N$ -electrons  $\Psi(\mathbf{r}_1, \dots, \mathbf{r}_N)$  becomes a function of  $3N$  coordinates (ignoring spin), and  $20^{3N}$  values are required to describe  $\Psi$  on the mesh. In contrast, the  $N$  single-particle wavefunction  $\varphi_i(\mathbf{r})$  in the Kohn-Sham equation require  $20^3 N$  values on the same mesh.



In summary, we have described a theory that is able to solve the complicated many-body electronic ground state problem by mapping exactly the many-body Schrödinger equation into a set of  $N$  coupled single-particle equations. The density of the non-interacting reference system is equal to that of the true interacting system. Up to now the theory is exact. We have not introduced any approximation into the electronic problem. All the ignorance about the many-electron problem has been displaced to the term  $E_{xc}[n(\mathbf{r})]$ , while the remaining terms in the energy are well known.

### 1.3.3 Exchange-correlation functionals

The complex many-body effects are hidden in the exchange-correlation functional  $E_{xc}[n(\mathbf{r})]$ . In the local density approximation (LDA), general inhomogeneous electronic system is considered as locally homogeneous.  $E_{xc}[n(\mathbf{r})]$  depends solely upon the value of the electronic density at each point in space (Generalized Gradient Approximation takes into account the gradient of the density). The most common form of LDA is the Ceperley-Alder form [6] as parameterized by Perdew and Zunger [7].

Although the LDA is very efficient for extended systems such as bulk metals, it fails to produce a correct ground state in strongly correlated systems. Such systems usually contains transition metal (or rare-earth metal) ions with partially filled  $d$  (or  $f$ ) shells. When applying a one-electron method with an orbital-independent potential, like in the LDA, to transition metal compounds, one has a partially filled  $d$  band with metallic-type electronic structure and itinerant  $d$  electrons. In fact, however, the  $d$  or  $f$  states are quite localized and Hubbard model [8] studies show a sizable energy separation between occupied and unoccupied bands due to Coulomb repulsion.

This error can be partly corrected with the LDA+U method, which is essentially a combination of the LDA and a Hubbard Hamiltonian for the Coulomb repulsion  $U$ . The LDA+U method includes an orbital-dependent one electron potential to account explicitly for the important Coulomb repulsions not treated fully in the LDA. Its total energy functional is given by adding the energy  $E_U$  of a generalized Hubbard model for the localized electrons to the LDA functional and by subtracting a double counting energy  $E_{dc}^U$  of the localized electrons described in a mean-field sense,  $E_{LDA+U} = E_{LDA} + E_U - E_{dc}^U$ .

A simplified approach to the LDA+U due to Dudarev [9] is of the following form:

$$E_{LDA+U} = E_{LDA} + \frac{U}{2} \sum [\rho(1 - \rho)]$$

with an orbital occupancy matrix  $\rho$ . Integer occupancy ( $\rho=0, 1$ ) is energetically favorable; partial occupancy ( $\rho=1/2$ ) is unfavorable. In addition, the effective LDA+U potential can be simply regarded as  $V_{LDA+U} = \delta E_{LDA+U} / \delta \rho = V_{LDA} + U(\frac{1}{2} - \rho)$ . This potential will shifts the LDA orbital energy by  $-U/2$  for occupied orbitals ( $\rho = 1$ ) and by  $+U/2$  for unoccupied orbitals ( $\rho = 0$ ), leading to an energy gap. In this thesis, the  $U$  values are treated as adjustable parameters rather than quantities derived from the first-principles calculation such as a constrained DFT approach.

Materials	Initial state $\Phi_0$	Tunable parameters	Driving force	Possible new states $\tilde{\Phi}_0$	New physical phenomena
LaAlO <sub>3</sub>   SrTiO <sub>3</sub> interfaces	Insulator	Varying thickness of LAO	Polar instability	Charge transfer; oxygen vacancy	A conducting interface
	Cubic perovskite	Making double n-interfaces	Structural instability	Rotation of TiO <sub>6</sub> octahedra	GdFeO <sub>3</sub> -type distorted structure
SrCuO <sub>2</sub> ultrathin films	Infinite layer structure	Thickness of thin films	Polar instability	Planar or Chain type of thin films	Thickness limits of ideal ultrathin films
LaOFeAs	S-AFM	Doping and pressure	Magnetic instability	C-AFM; NM	Superconductivity
Permalloy	Equilibrium	Temperature gradient	Non-uniform magnetization	Spin voltage without spin accumulation	Spin Seebeck effect

A common feature of all topics:  
new physical phenomena arise from tuning parameters of existing materials.

## 1.4 Outlook of this thesis

We follow the strategy outlined above to explore the new physical phenomena shown in the table.

In chapter 2 and 3, using first-principles density functional theory (DFT) calculations, we begin our study of LAO|STO by reproducing the band insulating states ( $\Phi_0$ ) of bulk LAO and STO with a cubic perovskite structure. In the case of LAO thin films grown on STO substrates, alternate stacking of positively (LaO<sup>+</sup>) and negatively (AlO<sub>2</sub><sup>-</sup>) charged layers on the non-polar STO substrate would give rise to a huge effective internal electric field if both materials kept the initial state  $\Phi_0$  and nothing else were to happen. The accompanying electrostatic potential would diverge with increasing thickness of LAO, leading to a polar instability. We demonstrate the internal electric field in terms of core level shifts calculated within DFT that are consistent with a parallel plate capacitor model.

Two mechanisms (new states  $\tilde{\Phi}_0$ ) have been suggested to avoid this instability and give rise to conducting behavior: charge transfer, or the creation of oxygen vacancies and other defects. The first mechanism refers to the transfer of electrons from a surface AlO<sub>2</sub> layer to the interface TiO<sub>2</sub> layer by the internal electric field. The excess charge at the interface balances the polar discontinuity and leads to conducting behavior of the interface. The second way to resolve the polar instability is to introduce defects at interfaces. Oxygen vacancies (and other defects) created during the growth of LAO on STO can naturally donate carriers, accounting for the conducting behavior.

In chapter 4, we find a strong position and thickness dependence of the formation energy of oxygen vacancies in LAO|STO multilayers and interpret this with an analytical capacitor model. Oxygen vacancies are preferentially formed at *p*-type

SrO|AlO<sub>2</sub> rather than at *n*-type LaO|TiO<sub>2</sub> interfaces; the excess electrons introduced by the oxygen vacancies reduce their energy by moving to the *n*-type interface. This asymmetric behavior makes an important contribution to the conducting (insulating) nature of *n*-type (*p*-type) interfaces while providing a natural explanation for the failure to detect evidence for the polar catastrophe in the form of core level shifts. Based on these results, the two doping mechanisms as well as the corresponding experimental evidence in their favour are naturally reconciled in a single framework.

In chapter 5, we predict GdFeO<sub>3</sub>-like rotation of TiO<sub>6</sub> octahedra at the *n*-type interface between cubic perovskite LAO and STO. The narrowing of the Ti *d* bandwidth by 1/3 which results means that LDA+U calculations predict charge and spin ordering at the interface for very modest values of U. Recent experimental evidence for magnetic interface ordering may be understood in terms of the close proximity of an antiferromagnetic insulating ground state to a ferromagnetic metallic excited state.

In chapter 6, we study the competition between electronic and atomic reconstruction in a thin film of the polar infinite-layer structure ACuO<sub>2</sub> (A = Ca, Sr, Ba) grown on a non-polar perovskite STO substrate. A transition from the bulk planar structure to a novel chain-type thin film accompanied by substantial changes to the electronic structure is predicted for a SrCuO<sub>2</sub> film thinner than five unit cells thick. An analytical model explains why atomic reconstruction becomes energetically more favourable than electronic reconstruction as the film becomes thinner and suggests that similar considerations should be valid for other polar films.

In chapter 7, we try to identify a magnetic phase diagram of La[O<sub>1-x</sub>F<sub>x</sub>]FeAs as a function of three key parameters: the doping *x*, the FeAs in-plane lattice constant *a*, and the distance *d* between the Fe and As planes. We do this by calculating the energy for non-magnetic (NM), checkerboard AFM (C-AFM) and stripe AFM (S-AFM) orderings. Consistent with experimental observations, our DFT calculated ground state of the undoped parent compound is S-AFM. With increasing electron doping, a sequence of S-AFM → C-AFM → NM ground states is found. Such a magnetic phase transition can be understood in terms of the density of states (DOS) of the parent compound close to the Fermi level. More importantly, we find a coexistence of NM, C-AFM, and S-AFM states at a tricritical point suggesting that spin fluctuations there may be stronger and more interesting.

In chapter 8, we try to understand the thermally induced long range spin voltage [3]. When a temperature gradient is maintained in a metal and no electric current is allowed to flow, there will be a steady-state electrostatic potential difference  $\Delta V$  between high- and low- temperature regions of the sample,  $\Delta V = Q * \Delta T$ , where *Q* is the so-called Seebeck coefficient depending on the electronic structure details. Naively, for a ferromagnetic material placed in a temperature gradient, two spin channels are thought to introduce different thermoelectric voltages  $\Delta V \uparrow$  and  $\Delta V \downarrow$ . At first glance, the experimentally observed long-range spin voltage can be simply attributed to  $\Delta V \uparrow - \Delta V \downarrow$

However, according to the well-established Valet-Fert equation, a spin voltage is expressed in terms of a spin accumulation, which will be strongly suppressed by

spin flip scattering and only exist on short length scales. The spin flip scattering is related to the spin flip diffusion length that is less than 10nm in permalloy. How does the long range spin voltage persist up to 1mm in the presence of strong spin flip? We therefore need to look for new contributions to spin voltage, in addition to spin accumulation.

Using a thermodynamic and statistical method, we find that a magnetization gradient will give rise to an effective long-range spin motive force in terms of entropy production. We therefore propose an explanation for the long-range spin voltage in terms of the magnetization potential associated with the thermally induced magnetization gradient, which has so far been neglected. We generalize the Valet-Fert equation and show that spin flip only suppresses spin accumulation but mediates the thermal generation of spin voltage.



# Chapter 2

## Bulk perovskite oxides

A perovskite structure is any material with the same type of crystal structure as calcium titanium oxide  $\text{CaTiO}_3$ . It is named after Russian mineralogist L. A. Perovski. The perovskite structure is adopted by many oxides that have the chemical formula  $\text{ABO}_3$ , where A and B are two cations of very different sizes, and  $\text{O}^{2-}$  is an anion that bonds to both. Perovskite and perovskite-like materials exhibit many interesting and intriguing properties from both the theoretical and the application point of view. Colossal magnetoresistance ( $\text{La}_{1-x}\text{Ca}_x\text{MnO}_3$ ), ferroelectricity ( $\text{BaTiO}_3$ ), superconductivity ( $\text{La}_{2-x}\text{Sr}_x\text{CuO}_4$ ), charge ordering ( $\text{Nd}_{0.5}\text{Sr}_{0.5}\text{MnO}_3$ ), spin dependent transport ( $\text{La}_{1-x}\text{Sr}_x\text{MnO}_3$ ), high thermopower ( $\text{NaCo}_2\text{O}_4$  and  $n$ -doped  $\text{SrTiO}_3$ ) and the interplay of structural, magnetic and transport properties are commonly observed features in this family [10, 11].

A central goal of our research is to understand and establish a predictive capability for electronic and atomic structures of perovskite oxides. We carry out a systematic study of perovskite oxides  $\text{LaAlO}_3$ ,  $\text{SrTiO}_3$  and  $\text{LaTiO}_3$  within the framework of the local density approximation (LDA) and generalized gradient approximations (GGA) of density functional theory (DFT).  $\text{LaAlO}_3$  and  $\text{SrTiO}_3$  are both band insulators with a cubic perovskite structure, whereas  $\text{LaTiO}_3$  is an antiferromagnetic Mott insulator [11] with a distorted perovskite structure.

In this chapter, we reproduce the band insulating nature of cubic perovskite  $\text{LaAlO}_3$  and  $\text{SrTiO}_3$ . More importantly, we show that the distorted structure of  $\text{LaTiO}_3$  is essentially predictable by the parameter free DFT-LDA calculations. Although the Mott insulating nature of  $\text{LaTiO}_3$  can not correctly be described by LDA, including an on-site Coulomb repulsion term  $U$  will heal this problem.

### 2.1 Perovskite structures

In the family of perovskite  $\text{ABO}_3$  compounds, various distortions of the high-temperature cubic structure are observed as a function of composition and temperature.

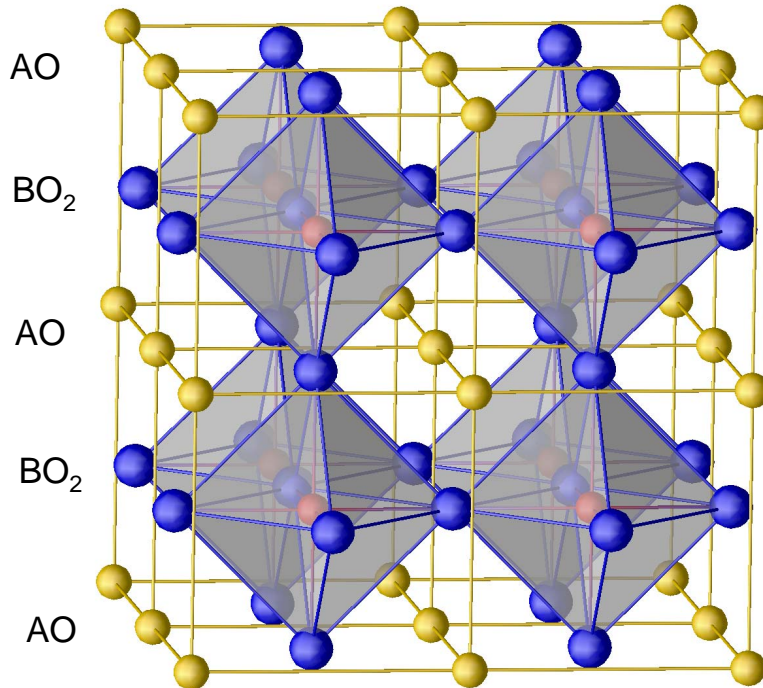


Figure 2.1:  $ABO_3$  with cubic perovskite structure. Oxygen atoms are marked by blue spheres; A atoms are marked by yellow spheres; B atoms are marked by red spheres. The structure can also be described in terms of AO and  $BO_2$  alternate stacking, or in terms of a cubic network of apex-sharing  $BO_6$  octahedra.

### 2.1.1 Cubic structure

We begin with the ideal cubic perovskite structure shown schematically in Figure 2.1. Usually, such a simple structure can be described in three different ways. The first description is: A atoms form a simple cubic structure, with B atoms at the body centers of the cubes and oxygen atoms at the face centers of the cubes. The second description regards the  $ABO_3$  perovskite structure as an alternate stacking of AO and  $BO_2$  layers; this is widely used in describing thin film growth.

In the third description, one B atom together with its six O atoms neighbors form a  $BO_6$  octahedron, in which the B atom is six-fold coordinated and surrounded by an octahedron of oxygen atoms. The entire structure is regarded as a cubic network of  $BO_6$  octahedra, with A atoms filling the holes between those oxygen octahedra. Geometrically, whether or not A atoms fit into the holes is determined by the relative size of ions, and influences the stability of the ideal cubic perovskite structure.

### 2.1.2 Distorted structure

The instability can be qualitatively described by the so-called Goldschmidt tolerance factor [12]

$$t = \frac{R_A + R_O}{\sqrt{2}(R_B + R_O)} \quad (2.1)$$

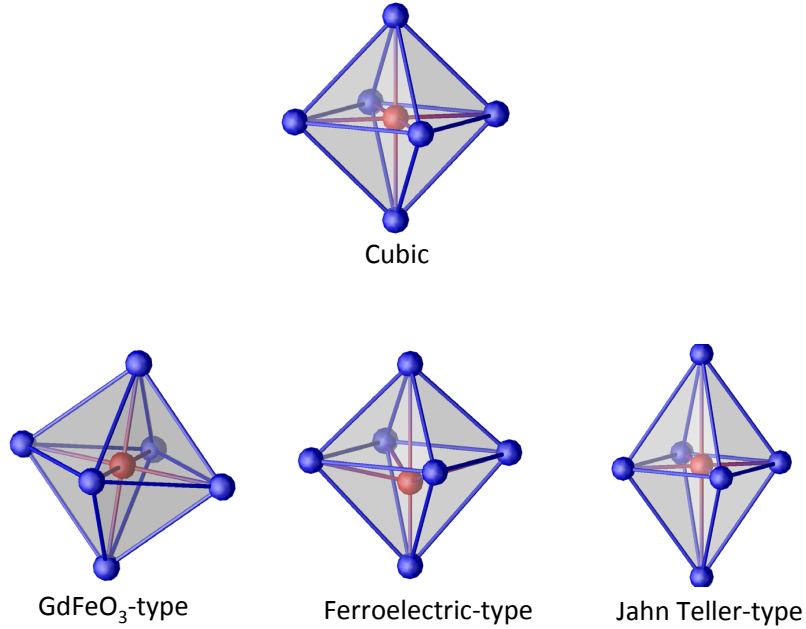


Figure 2.2: Three main types of distortion to the perovskite structure: tilting the  $\text{BO}_6$  octahedron (GdFeO<sub>3</sub>-type); off-center displacement of an undersized B cation (ferroelectric-type); elongation of B-O bonds along one direction and compression of the other B-O bonds (Jahn-Teller type).

where  $R_A$ ,  $R_B$  and  $R_O$  are the ionic radii [13] of the A, B, and O ions respectively. The ideal cubic structure is preserved only when the tolerance factor  $t$  of a perovskite oxide is close to 1. As shown in Table 1, the tolerance factor  $t$  for cubic SrTiO<sub>3</sub> and LaAlO<sub>3</sub> is close to 1. In reality, the tolerance factor of most perovskite materials is either smaller or larger than 1, and consequently a GdFeO<sub>3</sub>-type or a ferroelectric-type of distortion occurs as schematically shown in Figure 2.2. For a material with  $t < 1.0$  such as LaTiO<sub>3</sub>, A atom is smaller than ideal and  $\text{BO}_6$  octahedra will tilt in order to increase the space filling. This is a typical GdFeO<sub>3</sub>-type of distortion. For a material with  $t > 1.0$  such as BaTiO<sub>3</sub>, B atom is smaller than ideal and off-center displacement of an undersized B cation within its octahedron occurs to attain a stable bonding pattern. This is a typical ferroelectric-type of distortion.

Moreover, the perovskite structure is influenced not only by the relative size of

Materials ABO <sub>3</sub>	$R_A$ (Å)	$R_B$ (Å)	$R_O$ (Å)	$t$	Structure
SrTiO <sub>3</sub>	1.44	0.605 (Ti <sup>4+</sup> )	1.35	1.009	cubic
LaAlO <sub>3</sub>	1.36	0.535	1.35	1.016	cubic
LaTiO <sub>3</sub>	1.36	0.670 (Ti <sup>3+</sup> )	1.35	0.949	GdFeO <sub>3</sub> -type distortion
BaTiO <sub>3</sub>	1.61	0.605 (Ti <sup>4+</sup> )	1.35	1.071	Ferroelectric-type distortion

Table 1: Structures and tolerance factors  $t$  of perovskite oxides



radii of A and B as described by the tolerance factor  $t$ , but also by partially filled  $d$  states in transition metal cation B. A notable example is the Jahn-Teller type of distortion, which elongates the B-O bonds along the  $z$  direction while compressing other B-O bonds in the  $x, y$  directions as shown in Figure 2.2. This distortion occurs and lowers the electrostatic repulsion by lifting the degenerate  $d$  states.

## 2.2 Bulk SrTiO<sub>3</sub> and LaAlO<sub>3</sub>

Bulk SrTiO<sub>3</sub> is a paraelectric oxide with a cubic perovskite structure at room temperature. Below 105K it undergoes a symmetry-lowering transition to a tetragonal structure and approaches a ferroelectric phase with a very large dielectric constant. It is an excellent substrate for epitaxial growth of high-temperature superconductors and many oxide-based thin films, because its surface termination can be controlled [14, 15], its lattice constant matches these of numerous oxide materials closely, and because of its commercial availability. Bulk LaAlO<sub>3</sub> is a high  $\kappa$  dielectric oxide with a cubic perovskite structure.

Despite their structural similarity, SrTiO<sub>3</sub> and LaAlO<sub>3</sub> have a crucial difference from the viewpoint of thin film growth. If all ions are assigned formal charges, SrTiO<sub>3</sub> thin films can be regarded as alternate stacking of charge neutral SrO<sup>0</sup> layers and TiO<sub>2</sub><sup>0</sup> layers, while LaAlO<sub>3</sub> thin films consist of positively charged LaO<sup>+</sup> layers and negatively charged AlO<sub>2</sub><sup>-</sup> layers. We will show in chapter 3 that this difference leads to a polar instability of ideal interfaces connecting bulk SrTiO<sub>3</sub> and LaAlO<sub>3</sub>. This polar instability is a driving force for novel interfacial phenomena.

We first calculate the total energy of cubic SrTiO<sub>3</sub> and LaAlO<sub>3</sub> as a function of the lattice constant  $a$ . We determine the optimized lattice constant by minimizing the total energy. Our optimized lattice constants given in Table 2 agree well with experimental values [1]. Based on the optimized lattice constant, we can calculate energy gaps of both materials. The energy gaps are as usual systematically underestimated by DFT-LDA (or -GGA) calculations. For bulk SrTiO<sub>3</sub>, the calculated energy gap is almost half of the experimental value [1].

The fundamental band gap exists between filled O<sub>2p</sub> states and unfilled Ti<sub>3d</sub> states as shown in atomic projected density of states (DOS) in Figure 2.3. It is consistent with the band insulating nature of SrTiO<sub>3</sub>. We note that the projected DOS shows the existence of some moderate hybridization of Ti<sub>3d</sub> and O<sub>2p</sub> states. The hybridization can also be verified by a LDA +U calculation. As shown in Figure

	$a$ (LDA)	$a$ (GGA)	$a$ (exp)	Gap (LDA)	Gap(GGA)	Gap (exp)
SrTiO <sub>3</sub>	3.866 Å	3.945 Å	3.905 Å	1.88 eV	1.97 eV	3.2 eV
LaAlO <sub>3</sub>	3.754 Å	3.810 Å	3.789 Å	3.62 eV	3.68 eV	5.6 eV

Table 2: Calculated and experimental lattice constants and gaps of bulk SrTiO<sub>3</sub> and LaAlO<sub>3</sub>

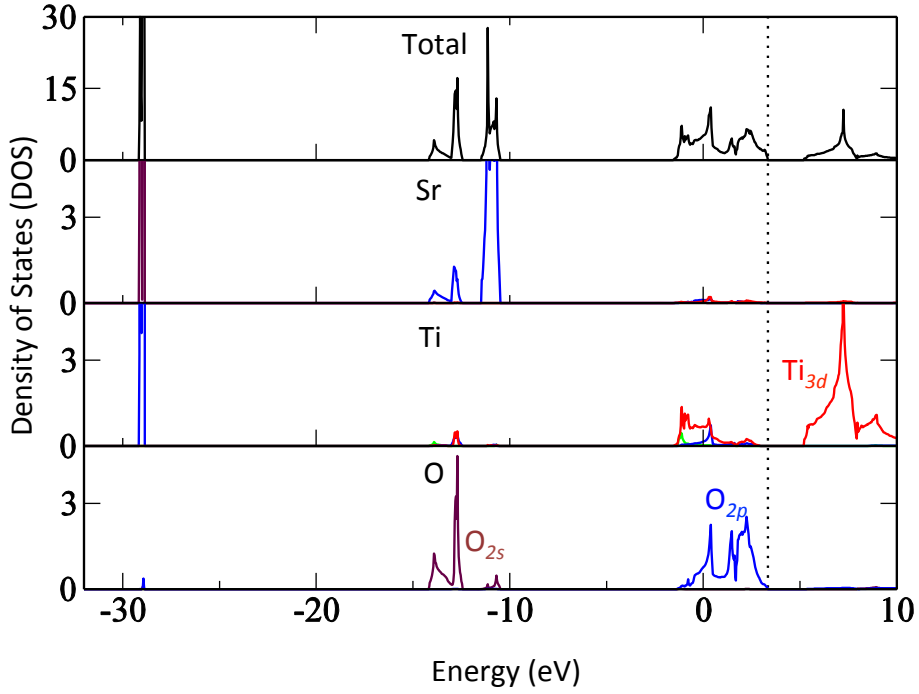


Figure 2.3: Atomic- and orbital- projected density of states (DOS) of bulk SrTiO<sub>3</sub>. *s* state is marked in brown; *p* state is marked in blue; *d* state is marked in red. The highest occupied states are O<sub>2p</sub>; the lowest unoccupied states are Ti<sub>3d</sub>.

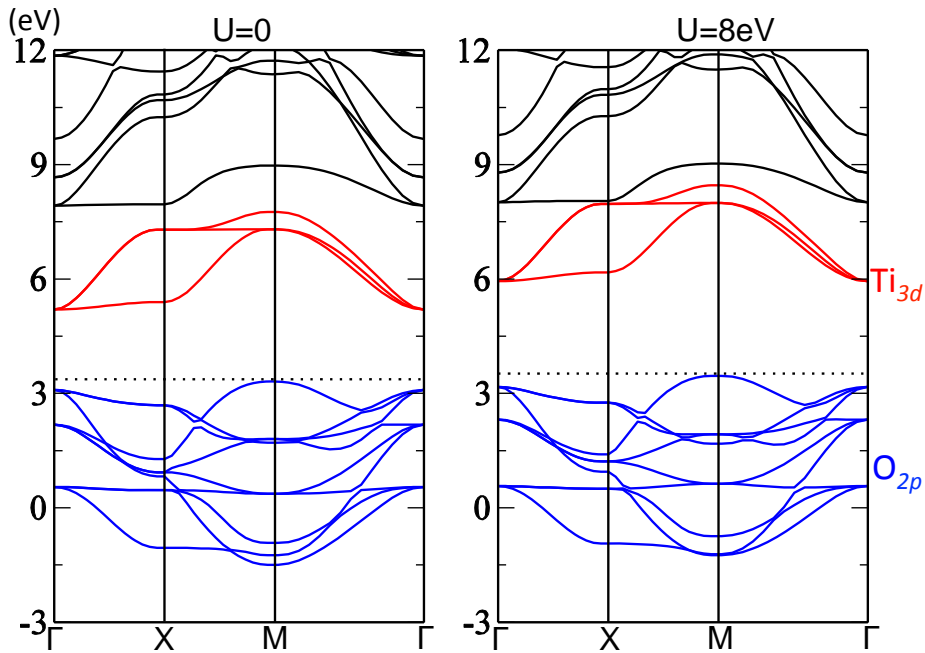


Figure 2.4: LDA and LDA+U calculated band structure of bulk SrTiO<sub>3</sub>. The blue are O<sub>2p</sub> bands; the red are Ti<sub>3d</sub> (*t<sub>2g</sub>*) bands.

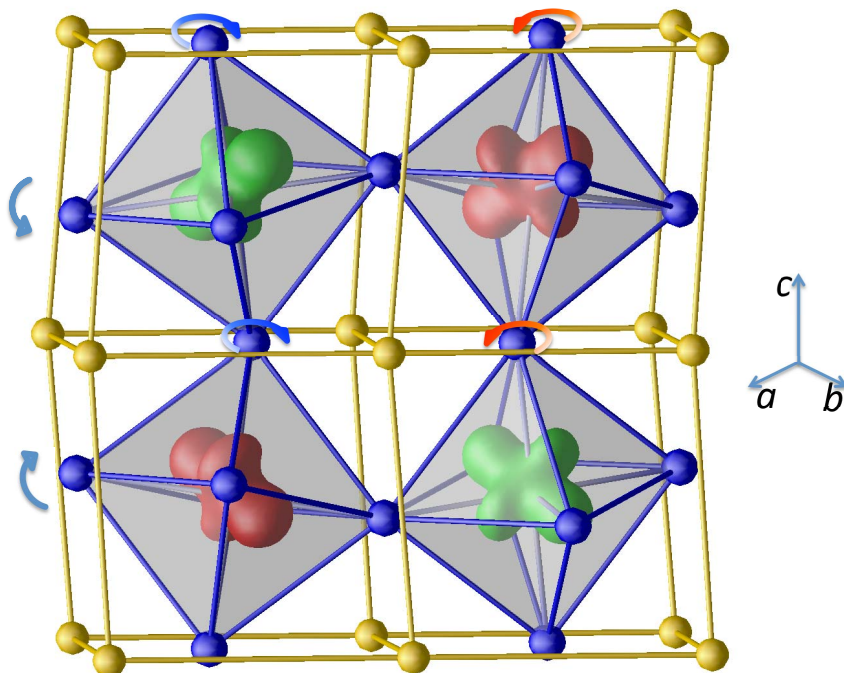


Figure 2.5:  $\text{LaTiO}_3$  with experimentally observed distorted perovskite structure. Oxygen atoms are marked by blue spheres; La atoms are marked by yellow spheres. Red and green represent surfaces of constant magnetization density but opposite sign

2.4, applying on-site coulomb repulsion  $U$  to Ti  $d$  electrons can enlarge the bandgap, suggesting that the  $\text{Ti}_{3d}$  states are not fully empty. (If they are empty,  $U$  will have no effects on the bandgap.) Nevertheless, this effect is relatively small and the band gap is only increased by 0.5eV with a large value of  $U=8\text{eV}$ . We therefore accept the formal valence of  $\text{SrTiO}_3$ :  $\text{Sr}^{2+}$ ,  $\text{O}^{2-}$ , and  $\text{Ti}^{4+}$  with empty  $d$  shell. In this sense,  $\text{SrTiO}_3$  is regarded as a  $d^0$  compound according to the number of electrons on the Ti  $3d$  shell.

Moreover, we also need to pay attention to shallow core states, such as  $\text{O}_{2s}$  and  $\text{Sr}_{5s}$ , which lie far below the Fermi level. Those inert core states are so tightly bound that they do not extend far enough to see the orbitals of neighboring atoms but they do see the electrostatic potentials. Any internal or external electric field applied to a material will result in a shift of those states in the DOS. In chapter 3, we will use the shift to indicate internal electric fields in thin films.

## 2.3 Bulk $\text{LaTiO}_3$

### 2.3.1 Distorted structure

Experimentally,  $\text{LaTiO}_3$  is a G-type antiferromagnetic Mott insulator with a Neel temperature of 146K [16–18] and a band gap of 0.2eV [19]. Compared to a divalent  $\text{Sr}^{2+}$  ion in  $\text{SrTiO}_3$ , a trivalent  $\text{La}^{3+}$  ion in  $\text{LaTiO}_3$  donates an additional electron

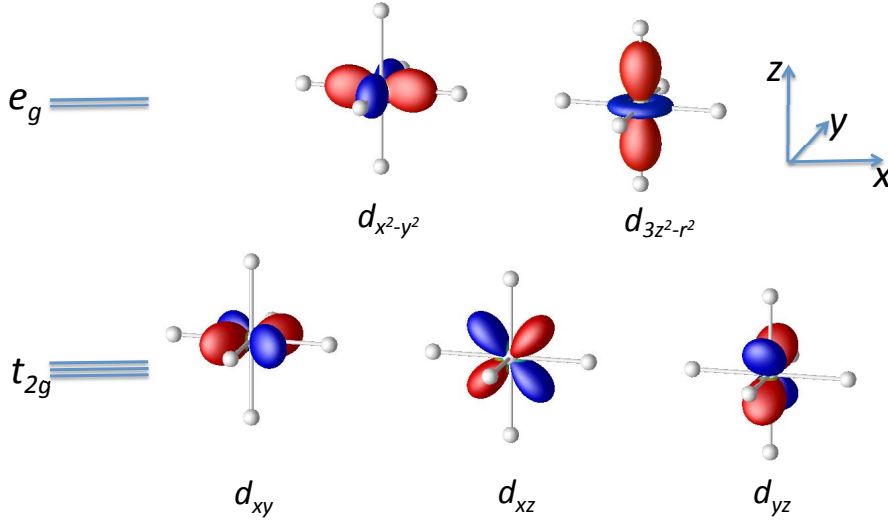


Figure 2.6: A graphical representation of 3d orbitals in a TiO<sub>6</sub> octahedron. The top two orbitals are  $e_g$ ; the bottom three are  $t_{2g}$ . Grey spheres represent oxygen atoms.

which goes into the unoccupied states with the lowest energy that have predominantly Ti<sub>3d</sub> character. Naively, the excess electron clouds surround the Ti ions, leading to an ionic radius  $R_{\text{Ti}^{3+}} = 0.670\text{\AA}$  larger than that for Ti<sup>4+</sup> ions,  $R_{\text{Ti}^{4+}} = 0.605\text{\AA}$ . Meanwhile the ionic radius of La<sup>3+</sup> is smaller than that of Sr<sup>2+</sup>. Therefore the Ti<sup>3+</sup> ion is too large and La<sup>3+</sup> is too small to maintain the cubic structure according to the Goldschmidt criterion as shown in Table 1. It leads to a GdFeO<sub>3</sub>-type crystal structure (space group  $Pbnm$ ) which can be derived from the ideal perovskite cubic structure by tilting essentially ideal TiO<sub>6</sub> octahedra about the orthorhombic  $b$ -axis followed by a rotation about the  $c$ -axis, as shown in Figure 2.5.

### 2.3.2 Influence of distortion on electronic structure

Before studying the electronic structure of  $d^1$  LaTiO<sub>3</sub> with one electron localized on each Ti site, we will use crystal field theory [20] to analyze characters of  $d$  orbitals in perovskite materials. With the theory, the interactions between metal ions (such as Ti atoms) and ligands (such as O atoms) are purely electrostatic; the bonding between them is completely ignored; oxygen atoms are regarded as point charges. For LaTiO<sub>3</sub>, one Ti atom together with its six O atoms neighbors form a TiO<sub>6</sub> octahedron, in which the Ti atom is surrounded by an octahedron of oxygen atoms. Therefore, the  $d$  electrons on the Ti site will mainly feel an octahedral crystal field created by its neighboring O<sup>2-</sup> point charges. Because the O<sup>2-</sup> will repel electron, the  $d$  electrons closer to O<sup>2-</sup> have a higher Coulomb energy than those further away. As a result, the crystal field split the initial five-fold degenerated orbitals of Ti  $d$  electrons as shown in Figure 2.6: three orbitals  $d_{xy}$ ,  $d_{xz}$  and  $d_{yz}$  go down in energy, forming triply degenerate  $t_{2g}$  orbitals; the other two degenerate orbitals  $e_g$  go up.

We turn to study the influence of structural distortion on electronic structure of

LaTiO<sub>3</sub>. Using LDA and LDA+U calculations, we will study electronic properties of bulk LaTiO<sub>3</sub> with a hypothetical cubic structure and the experimental structure. For the cubic structure, LDA gives a non-magnetic metallic ground state; including an on-site Coulomb repulsion term  $U_d^{\text{Ti}}=5\text{eV}$ , LDA+U gives a ferromagnetic metallic (FM-M) ground state. As shown in Figure 2.7, the calculated band structures in both cases contain a quite similar character: three-fold degenerate Ti<sub>3d</sub> ( $t_{2g}$ ) bands. The degeneracy is due to the octahedral crystal-field of the cubic perovskite structure, thus it is not lifted by including U. Since there is only one  $d$  electron per Ti site, the  $t_{2g}$  bands can only be partially filled, leading to a metallic behavior that is inconsistent with experimental observation.

For the experimental structure, LDA calculation gives a non-magnetic metallic ground state. LDA+U calculation with  $U_d^{\text{Ti}}=5\text{eV}$  reproduces the experimentally observed G-type antiferromagnetic insulator (AFM-I) ground state with a calculated bandgap of 1.0eV and local magnetic moment on Ti ions of  $0.8\mu_B$ . The band structures are shown in Figure 2.8. A remarkable feature of the LDA+U calculated band structure is: one  $t_{2g}$  band splits off completely from other two  $t_{2g}$  bands and a gap opens up for a half-filling (spin-polarized). The splitting state will be fully occupied by the excess Ti<sub>3d</sub> electron, which is spin polarized and anti-ferromagnetic coupled with the nearest Ti<sub>3d</sub> electrons. The orbitals of the  $d$  electrons on four Ti sites in a unit cell are different:  $0.55|xy\rangle \pm 0.35|yz\rangle \pm 0.76|xz\rangle$ . Therefore, the  $d$  electrons, occupying the splitting  $t_{2g}$  state, are spatially orbital ordered and anti-ferromagnetic coupled. This is apparent in the surfaces of constant magnetization density plotted in Figure 2.5.

Using the experimental (distorted) structure, we obtain an AFM-I ground state, consistent with experimental observations; in contrast, using the cubic (undistorted) structure, we obtain a metallic ground state. This different result is attributed to structural distortion. As stated in the section 2.3.1, the experimental structure is regarded as a distorted cubic structure with tilting (and rotation) of TiO<sub>6</sub> octahedra. We argue that this distortion will influence the electronic structure in two ways: by lifting the degeneracy of  $t_{2g}$  orbitals and by enhancing on-site Coulomb repulsion effects. First, tilting TiO<sub>6</sub> octahedra will not affect the shape of TiO<sub>6</sub>, and the crystal field created by O<sup>2-</sup> will be unchanged; however, the tilting will significantly lower the symmetry of the crystal field that is created by La<sup>3+</sup>. Thus, in the distorted structure with tilting of TiO<sub>6</sub> octahedra, the degeneracy of three  $t_{2g}$  orbitals will be lifted by the crystal field of La<sup>3+</sup> with low symmetry.

Second, the tilting of TiO<sub>6</sub> octahedra results in a Ti-O-Ti buckling, which narrows Ti  $d$  bands and effectively enhances the on-site Coulomb repulsion effects of Ti  $d$  electrons. We further investigate the effects by varying the value of  $U_d^{\text{Ti}}$  from 2eV to 7eV. As shown in Figure 2.9, below a critical U around 3eV, the ground state is non-magnetic metallic; above 3eV, it would be AFM-I. Further increasing U will enhance local magnetic moment, increase band gap but not change the essential features of electronic structures such as AFM-I and  $t_{2g}$  orbital ordered states.

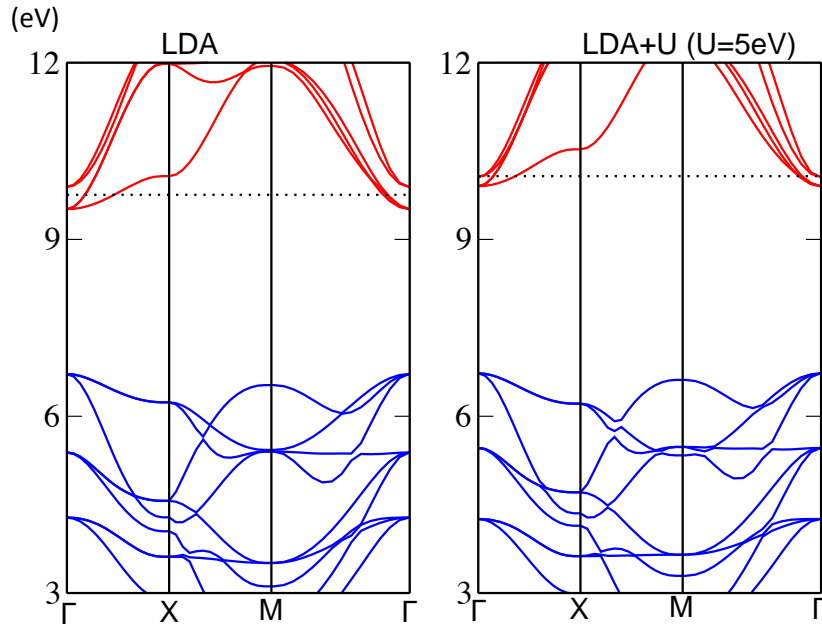


Figure 2.7: LDA and LDA+U calculated bands of bulk LaTiO<sub>3</sub> with the cubic structure. The blue are O<sub>2p</sub> bands; the red are Ti<sub>3d</sub> (*t<sub>2g</sub>*) bands

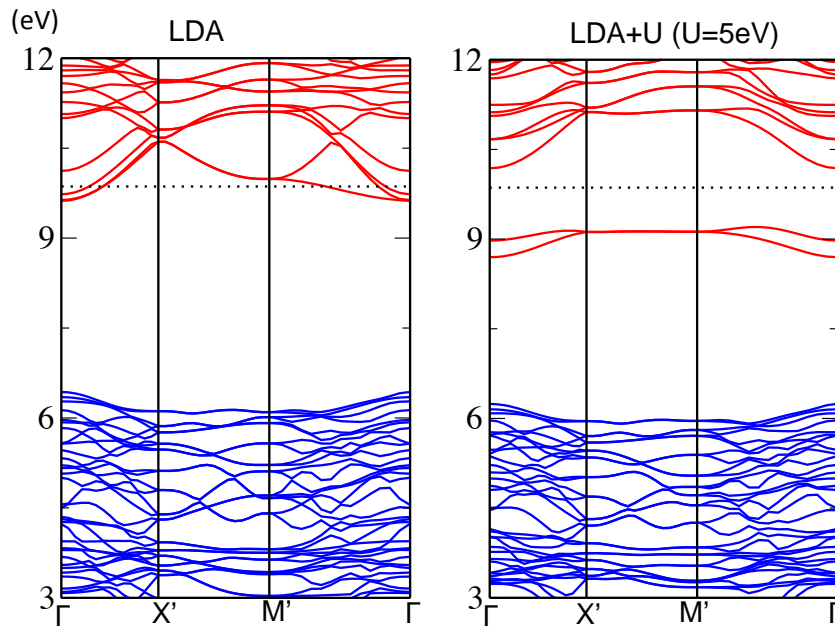


Figure 2.8: LDA and LDA+U calculated bands of bulk LaTiO<sub>3</sub> with the experimental structure. The blue are O<sub>2p</sub> bands; the red are Ti<sub>3d</sub> (*t<sub>2g</sub>*) bands. Because the experimental unit cell contains 20 atoms in contrast to a 5-atoms cubic unit cell, the bands of the two cells are comparable only when the bands of cubic cell in Figure 2.7 are folded.

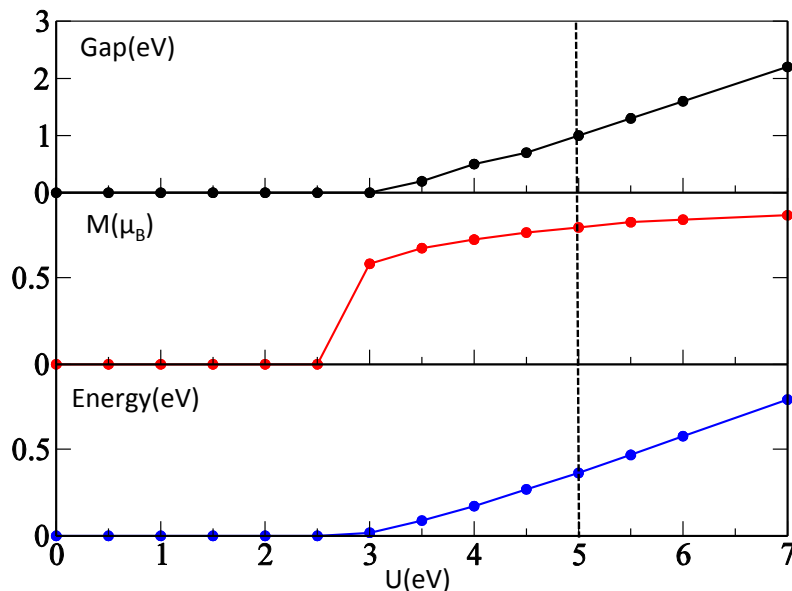


Figure 2.9: Band gap, localized magnetic moment on Ti ions, and magnetization energy as a function of  $U_d^{Ti}$ . The magnetization energy is defined as  $E_{\text{NM}} - E_{\text{AFM}}$  per formula unit.

### 2.3.3 Single band description

Our LDA+U results support a single band (the splitting  $t_{2g}$  state) description for  $d^1$   $\text{LaTiO}_3$ , consistent with previous DMFT [21] and model calculations [22]. Based on the single band description, we will try to understand the electronic properties of  $d^1$   $\text{LaTiO}_3$  with one electron localized on each Ti site. Step by step, we will show how charge, spin, orbital and lattice degrees of freedom are coupled.

- Without considering electron-electron interactions, the  $d$  band is half filled and electrons can freely move among Ti sites, thus the system is metallic.
- However, two electrons sitting on the same site would feel a large Coulomb repulsion, which would split the band in two: the lower band is formed from electrons that occupied an empty site and the upper one from electrons that occupied a site already taken by another electron. With one electron per site, the lower band would be full, and the system is an insulator.
- Further taking the spin freedom into consideration, the magnetic ordering of the material is determined by the competition between an intra-site and an inter-site magnetic interaction. The intra-site magnetic interaction originates from Hund's rule and favors FM ordering. The inter-site magnetic interaction originates from exchange interaction via oxygen atoms and favors AFM ordering. Often, in a single orbital model, exchange interaction is much stronger and hence AFM ordering will be the ground state.

- In  $d$  electron perovskite oxides, orbital degeneracy, such as three-fold  $t_{2g}$  and two-fold  $e_g$  states, is important and unavoidable source for complicated behavior. The orbital degeneracy will suppress the AFM and favor FM ordering. Therefore we can ascribe our calculated FM-M ground state of cubic LaTiO<sub>3</sub> to the degeneracy of  $t_{2g}$  orbitals because of the cubic symmetry of the crystal field.
- For LaTiO<sub>3</sub> with distorted structure, the orbital degeneracy is lifted by tilting of TiO<sub>6</sub> octahedra via the crystal field of La<sup>3+</sup>. On each site, a fully occupied  $t_{2g}$  orbital splits from the rest of  $t_{2g}$  states by lowering electrostatic energy. The basic characters of the split  $t_{2g}$  orbital on each site depend on the local tilting of TiO<sub>6</sub> octahedron. Consequently an orbital ordered pattern is established and magnetic ordering is sensitive to the orbital ordering details.

In summary, using DFT calculations and analysis, we have simply clarified how charge, spin, orbital and lattice interplay with each others for bulk LaTiO<sub>3</sub>. The structural distortion is crucial to properly describe the ground state of LaTiO<sub>3</sub>. If we ignore the lattice distortion and use a cubic structure, we will obtain an FM-M ground state with degenerate  $t_{2g}$  orbitals; if we use a distorted structure, we will obtain an AFM-I ground state with  $t_{2g}$  orbital ordering, consistent with experimental observations.

### 2.3.4 The distortion is predictable

In the previous section, we show that the electronic properties of  $d^1$  perovskite oxides (LaTiO<sub>3</sub>) are sensitive to the GdFeO<sub>3</sub>-type structural distortion. A question naturally arises. Is it possible to calculate and predict structural distortions such as GdFeO<sub>3</sub>-, ferroelectric- and Jahn Tell- type of distortions as mentioned in section 2.1.2? The structural distortions depend not only on relative radii of ions according to the empirical Goldschmidt criterion, but also on spatial distributions of

Material LaTiO <sub>3</sub>	$a(\text{\AA})$	$b(\text{\AA})$	$c(\text{\AA})$	La ( $x,y,z$ )	O(1) ( $x,y,z$ )	O(2) ( $x,y,z$ )
LDA	5.526	5.4763	7.7746	0.994, 0.038, 0.25	0.062, 0.490, 0.25	0.713, 0.285, 0.033
LDA+U (G-AFM)	5.6435	5.5885	7.9006	0.991, 0.051, 0.25	0.083, 0.496, 0.25	0.711, 0.292, 0.044
exp	5.6675	5.5867	7.9079	0.993, 0.049, 0.25	0.081, 0.494, 0.25	0.709, 0.294, 0.042

Table 3: LDA, LDA+U calculated and experimental structural parameters for bulk LaTiO<sub>3</sub> with the  $Pbnm$  symmetry



*d*-electrons such as orbital characters. In principle, the two factors are included at self-consistent level in first-principles DFT calculations. We therefore expect that DFT calculation should explain and even predict the structural distortions.

First of all, we start with bulk  $\text{LaTiO}_3$  with a cubic structure as well as the experimental observed distorted structure. We perform LDA calculations to fully relax both structures respectively. We find the relaxation processes only optimize relative atomic positions and lower total energy without altering the initial structural symmetry. For the cubic structure, the atomic relaxation will optimize its lattice constant and keep the cubic symmetry; for the distorted structure, the atomic relaxation will only slightly reduce but not eliminate the tilting of  $\text{TiO}_6$  octahedra shown in Table 3, comparing to the initial experimental structures.

More importantly, the total energies of two optimized structures indicate their respective stabilities. We find that the total energy of the relaxed distorted structure is 175meV/f.u. lower than that of the relaxed cubic structure. It implies that the distorted structure is more energetically favorable than the cubic structure. Therefore LDA calculation is able to reproduce and essentially predict the experimental structure of bulk  $\text{LaTiO}_3$  quite well except slightly underestimating the tilting of  $\text{TiO}_6$  octahedra. The underestimation mainly originates from the fact that LDA calculation improperly describes the spatial distribution and orbital character of the excess *d* electron, which considerably affects structural distortion from the viewpoint of electrostatic energy.

This discrepancy can be solved by including an on-site Coulomb repulsion term *U*, because LDA+*U* calculations can properly provide an orbital ordered AFM-I ground state. As expected, the LDA+*U* results shown in Table 3 are even closer agreement with experiment, which shows that the orbital character of *d* electrons also have moderate contribution to the structural distortion.

## 2.4 Summary

In this chapter, we use first principles DFT calculations to study the electronic and atomic structures of bulk  $\text{SrTiO}_3(d^0)$ ,  $\text{LaAlO}_3(d^0)$  and  $\text{LaTiO}_3(d^1)$ . For  $\text{SrTiO}_3$  and  $\text{LaAlO}_3$ , our calculated lattice constants agree well with the experimental values; the band insulating nature can be well reproduced but with an as usual underestimated bandgap. For  $\text{LaTiO}_3$ , parameter-free LDA calculation can essentially reproduce the experimentally observed distortion but with a slightly reduced octahedra rotation. Including an on-site Coulomb repulsion term *U* will lead to an orbital ordered AFM-I state, consistent with experimental observation. Moreover LDA+*U* will considerably improve the calculated crystal structure and fit the experimental value better. Our results show that first principles DFT calculation can essentially predict atomic structure of perovskite oxides. Including repulsion term *U* can properly describe electronic structure of correlated perovskite oxides, as well as its interplay with atomic structure.

# Chapter 3

## LaAlO<sub>3</sub>|SrTiO<sub>3</sub> interfaces

### 3.1 Introduction

When growing thin films of oxides, ABO<sub>3</sub> perovskite oxides can be regarded as an alternate stacking along a (001) direction of AO and BO<sub>2</sub> layers. Looked at in this way, SrTiO<sub>3</sub> (STO) consists of charge neutral SrO<sup>0</sup> and TiO<sub>2</sub><sup>0</sup> layers, while LaAlO<sub>3</sub> (LAO) consists of positively charged LaO<sup>+</sup> and negatively charged AlO<sub>2</sub><sup>-</sup> layers. LAO thin films can be grown on an STO substrate with high quality interfaces because of the structural similarity and small lattice mismatch between them. Because the surface of an STO substrate can be controlled to be terminated by a TiO<sub>2</sub> or a SrO layer [1, 14, 15], two types of interfaces, schematically shown in Figure 3.1, are formed: a metallic *n*-type (LaO|TiO<sub>2</sub>) interface and an insulating *p*-type (AlO<sub>2</sub>|SrO) interface [1]. The conducting *n*-type interface has been reported to have a number of appealing properties, including a high electron mobility, superconductivity, magnetoresistance and spin-orbit coupling [23–32]. Why *n*-type interfaces are conducting while *p*-type interfaces are not is the subject of intense debate [33–51] and two types of doping mechanisms are proposed to account for the conducting behaviour: pure charge transfer [33] or the creation of oxygen vacancies [35, 39] and other defects [38, 40, 45].

The first mechanism originates from the so-called polarity discontinuity [1, 33] between polar LAO and non-polar STO. An alternate stacking of positively (LaO<sup>+</sup>) and negatively (AlO<sub>2</sub><sup>-</sup>) charged layers on the non-polar STO substrate would give rise to an effective internal electric field  $E$ . As estimated using a simple parallel plate capacitor model,  $E$  is as large as  $\frac{1}{\epsilon} 1.2 \times 10^{11}$  V/m or  $\frac{47}{\epsilon}$  V/unit cell, where  $\epsilon$  is the dielectric constant of LAO. The electrostatic potential diverges with increasing thickness of LAO, leading to an instability. In response to the instability, electrons will be transferred from a surface AlO<sub>2</sub> layer to the interface TiO<sub>2</sub> layer by the internal electric field. The excess charge at the interface balances the polar discontinuity and leads to conducting behavior of the interface. This intrinsic-type doping mechanism is strongly supported by the experimental observation of a critical thickness behavior [24]: for LAO thickness of (or below) 3 unit cell, the *n* interface is insulating; an insulator-metal transition can be induced by applying an external

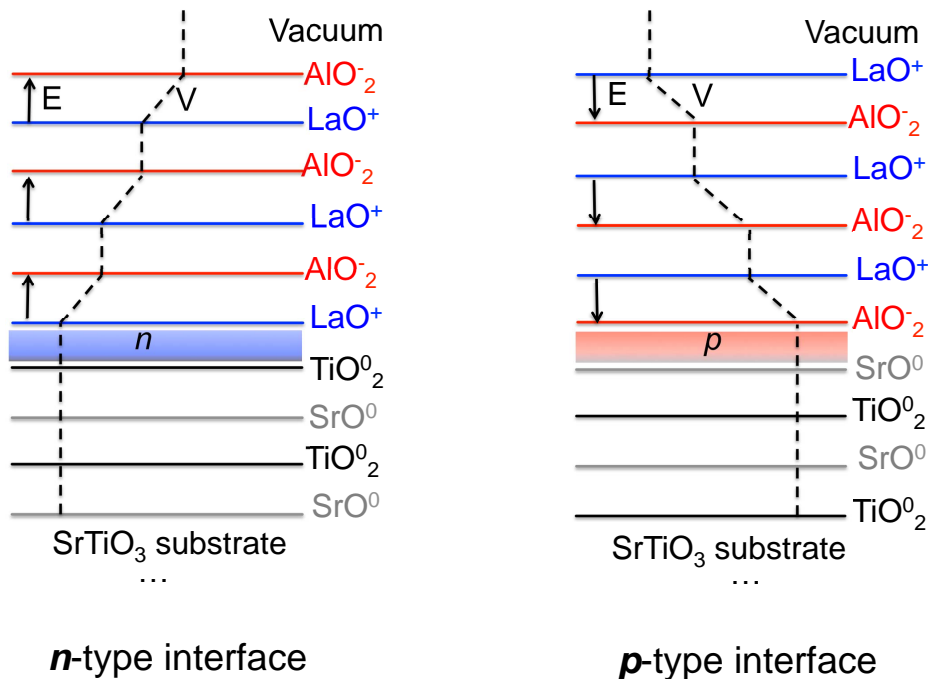


Figure 3.1: Schematic figures of LAO thin films grown on an STO substrate with a single  $n$  type interface (left) or a single  $p$  type interface (right). The induced internal electric field  $E$  is indicated with arrows; the electrostatic potential  $V$  is marked by the dashed line.

electric field or by adding LAO thin films. This critical thickness behavior is almost exactly expected by the intrinsic-type doping mechanism. However, direct experimental evidence of charge transfer, in the form of core level shifts, has not yet been found [37, 43]. The insulating behavior of the  $p$ -type interface [1] is also not readily accommodated in this picture.

The second mechanism refers to the creation of oxygen vacancies and other defects. It is well known that high energy pulsed laser deposition growth can easily create oxygen vacancies and other defects such as La-Sr intermixing. Each oxygen vacancy will donate two electrons, and this accounts naturally for the conducting behavior. This extrinsic-type doping mechanism is supported by several experimental observations. For instance, the conductivity depends sensitively on the growth conditions, in particular on the oxygen pressure, immediately suggesting the presence of oxygen vacancies [25, 35, 39]; the long-relaxation time of the electric-field-induced insulator-metal transition [27] suggests the possibility of interface defect diffusion. However, this mechanism can not easily explain the thickness dependence of transport behavior [23, 24], as well as an insulating behavior of an STO|STO interface [52]. The STO|STO interface is formed by growing STO thin films on an STO substrate under the same experimental conditions as LAO thin film growth. Unlike the LAO|STO interface, the STO|STO interface was found to be insulating. This was used as evidence that oxygen vacancies are not formed during growth.

Usually, the two mechanisms are considered to be mutually exclusive and are classified as intrinsic and extrinsic mechanisms [34]. From this point of view, oxygen vacancy formation and other defects are regarded as the result of imperfect experiments, and improved experimental techniques could eventually eliminate these defects to realize ideal interfaces with pure charge transfer. For example, the concentration of oxygen vacancies should be reduced by increasing the oxygen pressure during growth or annealing; therefore it should be possible to exclude oxygen vacancies by using sufficient high oxygen pressures.

## 3.2 Outline

Contrary to what is usually believed, we will argue that oxygen vacancy formation is intrinsic and can be induced by a polar instability. Two doping mechanisms are thereby coupled and naturally reconciled into a single framework in response to the polar instability. The coupling and competition between the two mechanisms is the source of puzzling behavior in LAO|STO. To reveal this coupling and competition is a major goal of our study.

In this chapter we will use first-principles density functional theory (DFT) calculations to study the properties of ideal LAO|STO interfaces. Consistent with the parallel plate capacitor model, our results confirm the existence of a large internal electric field, as probed by energy levels of core states. For LAO thin films with thickness below a certain critical value, charge transfer does not occur and the internal electric will be almost constant; as the thickness of LAO films increases, the accompanying electrostatic potential increases; for thick films, charge transfer occurs, the internal electric field will be suppressed, and the accompanying electrostatic potential saturates at the bandgap of STO. The internal electric field will drive a thickness dependent insulator-metal transition, which is exactly expected by the intrinsic doping mechanism.

Here, we need to emphasize that like most theoretical studies in the literature [44, 53–69], this argument is based on an ideal interface assumption. In the case of ideal interfaces, the internal electrostatic energy can be reduced and the polar instability can be resolved by charge transfer. However, there is a serious inherent problem with this picture. In the section 3.5, we will try to show that LAO|STO interfaces cannot be ideal.

## 3.3 Multilayers of $\text{LaAlO}_3|\text{SrTiO}_3$

There are two basic LAO|STO configurations of current experimental interest: LAO films grown on STO substrates and LAO|STO multilayers. The former configuration, shown in Figure 3.1, contains a single *n*-type or *p*-type interface. The latter configuration, shown in Figure 3.2, contains periodically repeated *np*, *nm*, or *pp* interfaces. Because *n*-type is of greatest interest, we focus on three systems: (1) multilayers with *np* type interfaces, (2) LAO thin films grown on an STO substrate

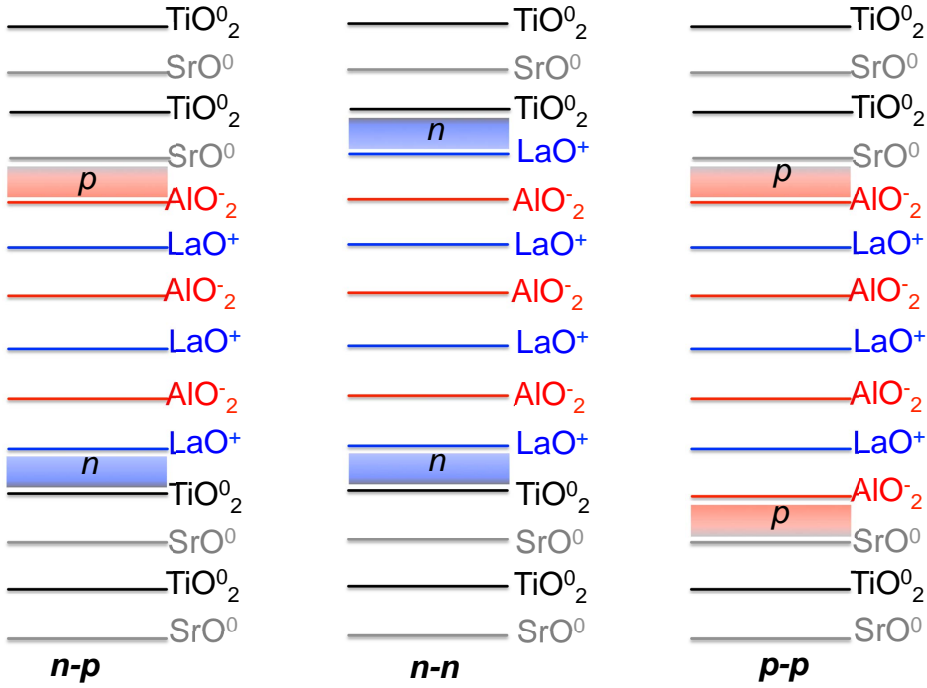


Figure 3.2: Schematic figures of multilayers of LAO|STO with repeated  $np$  (left),  $nn$  (middle),  $pp$  (right) interfaces

with a single  $n$ -type interface, and (3) multilayers with  $nn$  type interfaces (in chapter 5).

Though most experimental studies have been made on samples consisting of STO substrates covered with several layers of LAO, we have chosen to first study multilayers of LAO|STO in detail and later briefly discuss LAO thin films. Multilayers have the advantage that they have fewer degrees of freedom and there is a considerable amount of experimental information about their structures available. If we regard the surface of LAO as a pseudo- $p$  type interface, the physics of LAO thin film should be similar to that of multilayers. In this chapter, we argue that much of the physics of the polar instability that can be learned from the case of multilayers is applicable to the case of LAO surface.

### 3.3.1 Polar instability

We focus on  $(m,m)$  LAO|STO multilayers containing  $m$  layers each of LAO and STO with alternating  $p$ - and  $n$ -type interfaces. Each layer consists of a  $1 \times 1$  unit cell in the plane of the interface. We will vary  $m$  to study the thickness dependent behaviors.

In LAO|STO multilayers without any interfacial reconstruction, LAO and STO are separated by asymmetric positively charged  $n$ -type  $\text{LaO}^+|\text{TiO}_2^0$  and negatively charged  $p$ -type  $\text{SrO}^0|\text{AlO}_2^-$  interfaces. We therefore model LAO|STO as alternating positive and negative sheet of charge with areal charge density  $\pm\sigma = \mp e/a^2$ , where

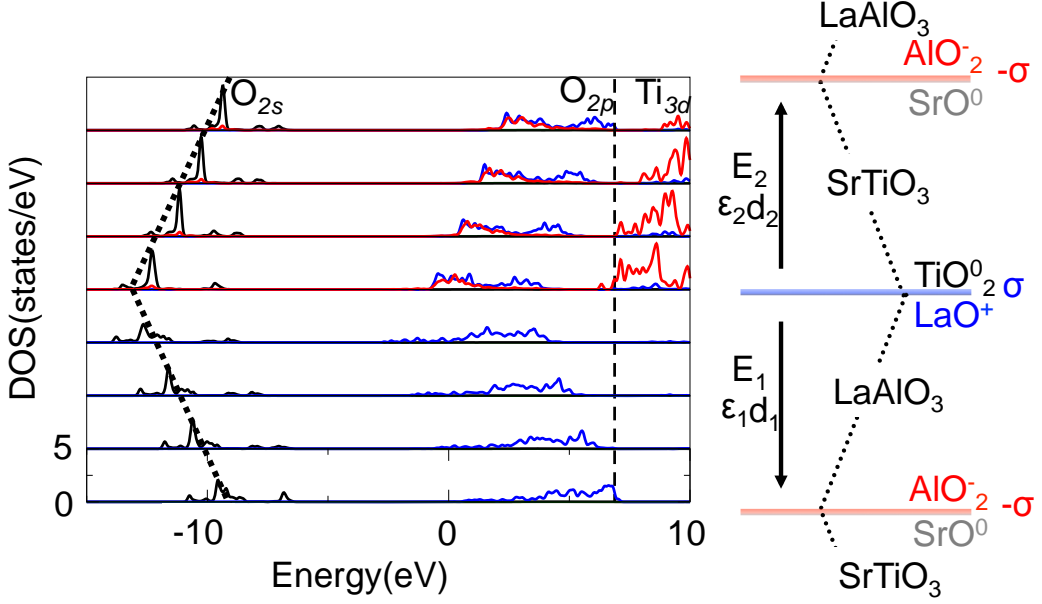


Figure 3.3: Layer projected density of states, including  $O_{2s}$  semi-core states (black),  $O_{2p}$  states (blue) and  $Ti_{3d}$  states (red), of an unrelaxed (4,4) LAO|STO multilayer. A schematic of the capacitor model is shown in the right panel. The electrostatic potential profile for the vacancy-free structure is shown as a dotted line.

$a$  is the lattice constant of bulk STO and the charge of electron is  $-e$ . As sketched in Figure 3.3, the plates of the capacitor are separated by a thickness  $d_1$  ( $d_2$ ) of insulating LAO (STO) with dielectric constants  $\epsilon_1$  ( $\epsilon_2$ ) determined by the electronic- as well as atomic- polarization. Based on this simple planar capacitor model, there will be an internal electric field  $E$ , pointing from positively charged  $n$ -type to negatively charged  $p$ -type interfaces. It can be expressed as  $E = \frac{\sigma/\epsilon_0}{\epsilon_1 d_2 + \epsilon_2 d_1}$ , where  $\epsilon_0$  is the dielectric constant of vacuum. For simplicity we set  $d_1 = d_2$ , then the internal electric field will be  $\frac{\sigma/\epsilon_0}{\epsilon_1 + \epsilon_2}$ . If this is correct, the estimated internal electric fields are huge,  $\frac{1}{\epsilon_1 + \epsilon_2} 1.2 \times 10^{11} \text{V/m}$ , independent of the thickness  $m$ . Consequently the electrostatic potentials inside LAO and STO layers are expected to exhibit a simple symmetric triangular form.

The internal electric field and the associated electrostatic potential can be probed by examining the energy levels of core states in LDA calculations in the absence of ionic relaxation. We show layer projected density of states (DOS) of a (4,4) LAO|STO multilayer in Figure 3.3. The layer projected  $O_{2s}$  core level that we use to represent the local electrostatic potential, shifts roughly 0.9V per unit cell or 3.6V in total between the  $n$  and  $p$ -type interface. According to the core level shift, we could estimate the dielectric coefficient  $\epsilon_1 + \epsilon_2 = 52$  roughly. Experimentally, bulk LAO is a high dielectric insulator with  $\epsilon_1 = 27$ , and bulk SrTiO<sub>3</sub> is nearly ferroelectric insulator with  $\epsilon_2 \gg \epsilon_1$ . However, in this polar thin film structure, the internal electric field is so large that we are not in the linear response regime. Ionic relaxation is not allowed and only the electronic contribution to dielectric constant is included, thus

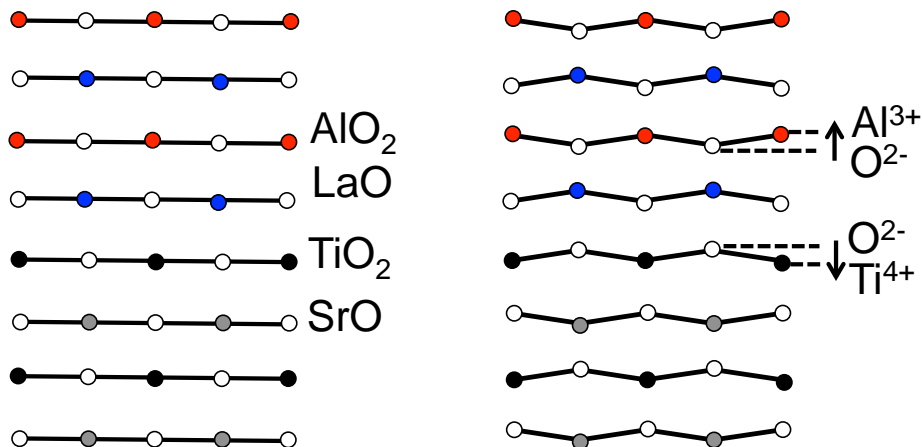


Figure 3.4: (left) Before atomic relaxation, A and O atoms are in the same AO plane; B and O atoms are in the same BO<sub>2</sub> plane. (right) After relaxation, zigzag Ti-O type of buckling occurs

the estimated  $\epsilon_1 + \epsilon_2$  is still plausible.

In summary, a simple planar capacitor model suggests an internal electric field in LAO|STO. Our DFT calculation manifests the electric field in the form of core level shifts, confirming that a polar instability should exist in LAO|STO. In literatures, a terminology “polar catastrophe” [33] is widely used to describe that the accompanying electrostatic potential diverges with increasing thickness of LAO because of the internal electric field. In this thesis, we try to introduce the terminology “polar instability” from the viewpoint of electrostatic energy. The accompanying electrostatic energy,  $\frac{1}{2}\epsilon E^2 \times Volume$ , will cause an instability of LAO|STO. In section 3.5, analyzing the polar instability, we point out an inherent problem of the assumption of ideal LAO|STO. This problem can not be seen by the polar catastrophe.

### 3.3.2 Charge transfer and atomic relaxation

The internal electric field will exert a force on the electrons and atoms (ions), causing them to move. This motion generates compensating electric fields in response to the instability. When all the atomic positions are fixed and only electrons are allowed to move, the response to the internal electric field is charge transfer: O<sub>2p</sub> valence electrons at the *p*-type interface are transferred to Ti<sub>3d</sub> unoccupied states at the *n*-type interface as shown in the DOS plotted in Figure 3.3. This charge transfer leads to electron doping of the *n*-type interface and hole doping of the *p*-type interface. It also produces a compensating electric field thereby suppressing the polar instability.

We next consider atomic relaxation. The unrelaxed LAO|STO multilayer consists of AO and BO<sub>2</sub> layers, in which A and O (or B and O) atoms are planar. When atoms are also allowed to move, A and O (or B and O) are not in the same plane anymore. The most striking feature of atomic relaxation is the Ti-O type of buck-

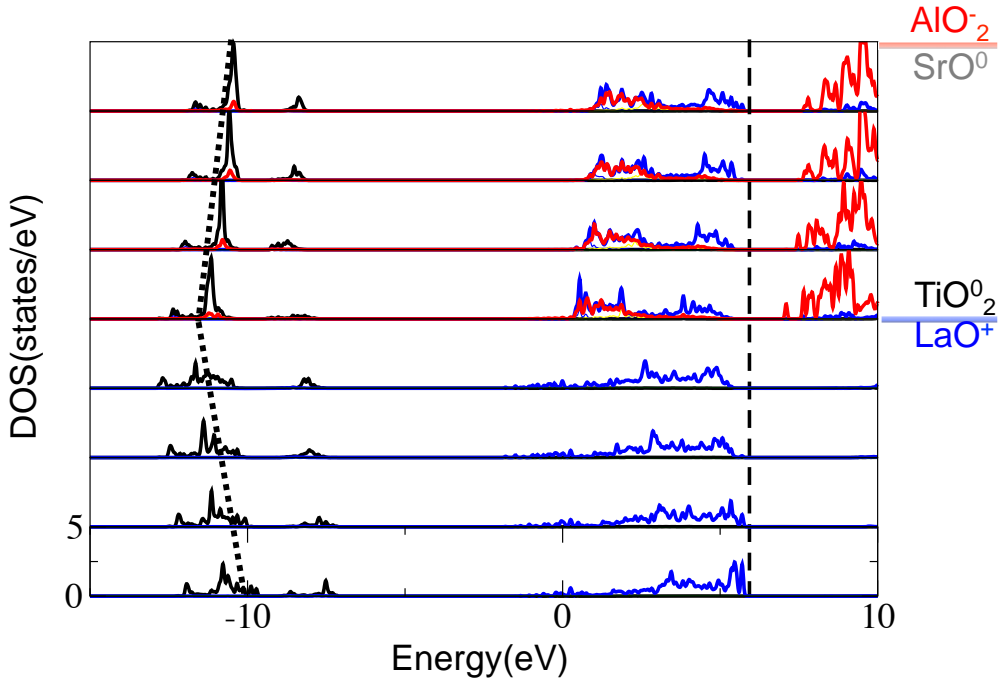


Figure 3.5: Layer projected density of states of a relaxed (4,4) LAO|STO multilayer

ling shown in Figure 3.4. The relative displacement of Ti and O atoms along the  $z$  direction is of order of  $0.1\text{\AA}$ . We find that the signs of the buckling in LAO and STO are opposite in LAO and STO layers, consistent with the orientation of the internal electric field.

The buckling will split the initial planar AO (or  $\text{BO}_2$ ) layer into two effective charged plates such as  $\text{Ti}^{4+}$ ,  $\text{O}_2^{2-}$ . The induced charged plates sequence leads to a compensating electric field and screen the polarity. This screening effects can be seen in Figure 3.5 of a relaxed (4,4) LAO|STO. The  $\text{O}_{2s}$  core level shift, as a direct measure of the internal electric field, is reduced from  $0.9\text{eV}/\text{layer}$  to  $0.22\text{eV}/\text{layer}$ . Therefore,  $\text{O}_{2p}$  bands will not cross the Ti  $d$  bands at the  $n$  type interface and consequently no charge transfer occurs. The whole system is insulating with an energy gap of  $1.2\text{eV}$ . In this sense, atomic relaxation will enhance the dielectric constant, and become a more energetically favorable way to suppress the polar instability. Charge transfer would not occur at low thickness limits.

### 3.3.3 Thickness dependence

For  $(m,m)$  LAO|STO thin films where thickness  $m$  is below a certain critical value, charge transfer does not occur and the entire system can be described as a planar capacitor with fixed charge density. Therefore the electric field is constant and the electrostatic potential increases as the plate separation LAO thickness is increased. Our calculation confirms this thickness dependence. The internal electric field can be measured by the average value of the Ti-O type zigzag buckling as well as by the



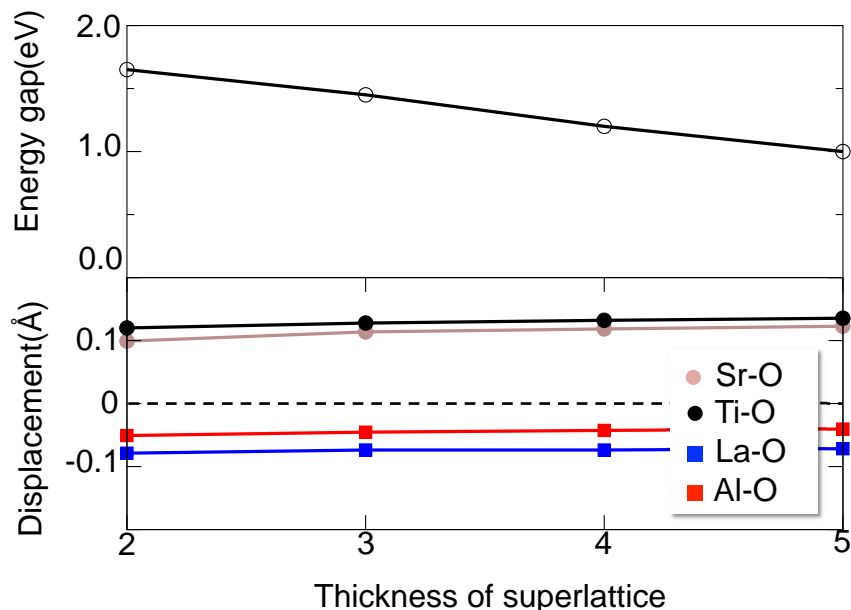


Figure 3.6: Thickness dependence of the energy gap and averaged displacements

core level shift, and this is plotted as a function of  $m$  in Figure 3.6. As expected, it is almost a constant and independent of thickness  $m$ .

When the internal electric field is a constant, the electrostatic potential will be proportional to thickness  $m$ . The energy gap will therefore decrease as  $m$  increases as shown in Figure 3.6. The rate of decrease is about  $0.2\text{eV/unit cell}$ , consistent with the core level shift. So, we can expect the energy gap to disappear at a critical thickness  $m \cong 10$ . Above this critical thickness, the internal electrostatic potential is sufficiently large to drive charge transfer and induce an insulator-metal transition.

### 3.4 $\text{LaAlO}_3$ thin films grown on a $\text{SrTiO}_3$ substrate

In the previous section, we studied  $(m,m)$  LAO|STO multilayers containing  $m$  layers each of LAO and STO with alternating  $p$ - and  $n$ -type interfaces. We demonstrated the existence of polarity in terms of core level shifts and zigzag Ti-O atomic relaxation. The atomic relaxation and charge transfer act together in response to the polar instability. In this section, we will study LAO thin films grown on an STO substrate with a single  $n$ -type interface. The single  $n$  type interface is of most experimental interest, because it exhibits a number of appealing properties, including a high electron mobility, superconductivity, magnetoresistance and spin-orbital coupling.

We use 7 unit cells of  $\text{SrTiO}_3$  to model the substrate terminated with a  $\text{TiO}_2$  layer. When LAO thin films are grown on this substrate, a LaO layer is the first stacking layer so an  $n$  type interface will be formed. An  $\text{AlO}_2$  layer will terminate the thin films and become the surface layer. The thickness of LAO is varied from 0 to 7 unit cells. We fix the in-plane lattice constant at the calculated equilibrium value of STO but allow all other atomic relaxation. We ignore complexities and

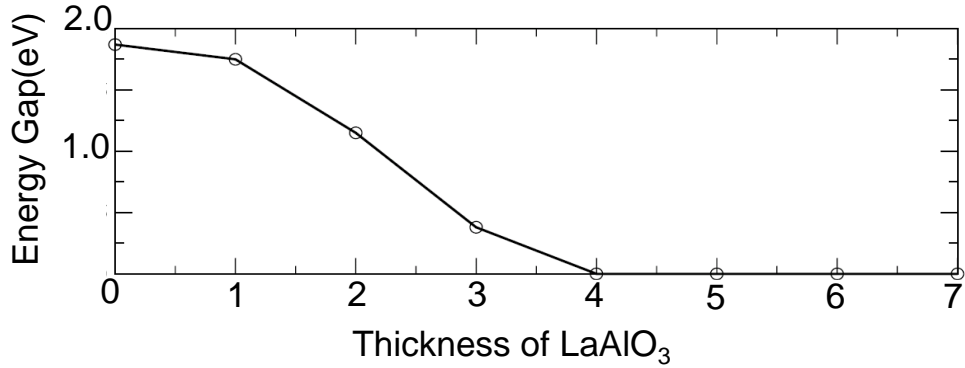


Figure 3.7: Thickness dependence of gap of LAO thin films grown on an STO substrate

uncertainties of the LAO surface and assume it is clean. If we regard it as a pseudo- $p$  type interface, we expect the polar instability for multilayers to be valid for LAO thin films. For LAO|STO multilayers, using the parallel plate capacitor model and DFT calculations, we found an internal electric field of order 0.2V/unit cell. We can simply extend the model according to the electrostatic boundary condition of the growing LAO thin films. The internal electric field will be twice as in the multilayer case; it will be about 0.4V/unit cell and the associated critical thickness should be about 5 unit cells.

This expectation is qualitatively verified by DFT calculations. As shown in Figure 3.7, the bandgap of a TiO<sub>2</sub> terminated STO substrate is roughly 1.8eV; it is considerably reduced by adding LAO to STO. The bandgap is predicted to disappear and an insulator-metal transition occurs, when the LAO thin film is thicker than 4 unit cells. We note that it is more or less a coincidence that the calculated critical

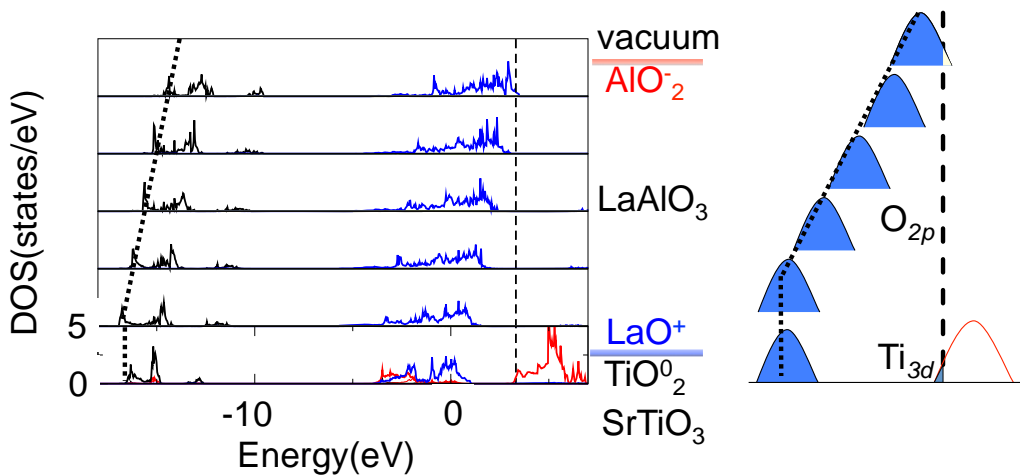


Figure 3.8: Layer projected DOS of LAO thin films with thickness  $m=5$  grown on an STO substrate

thickness is the same as the experimental observation, considering the underestimation by the LDA of STO and LAO bandgaps.

We can analyze the physics of the bandgap reduction using projected DOS. Just as in the case of multilayers, the projected DOS of LAO thin films exhibit a clear core level shift as a manifestation of the internal electric field. The highest occupied states of bulk LAO and STO have O<sub>2p</sub> character. The O<sub>2p</sub> valence band state of LAO at the interface are matched with the O<sub>2p</sub> valence band state of STO substrate. The internal electric field shift the LAO valence band of towards high energy. When LAO is thicker than 4 unit cells, the LAO surface valence band crosses the STO bandgap and the surface O<sub>2p</sub> valence electrons will be transferred to Ti<sub>3d</sub> conduction bands of STO. This is almost exactly expected by the intrinsic doping picture. However, we note that the core level shift, as a key evidence of charge transfer, is not experimentally observed [43].

### 3.5 The Interface can not be ideal

Using DFT calculations and a planar capacitor model, we study LAO|STO multilayers as well as LAO thin films grown on an STO substrate. For both two cases, we find a large internal electric field  $E$  that originates from the polar discontinuity at LAO|STO interfaces. The internal electric field  $E$  (or the accompanying electrostatic energy  $\frac{1}{2}\epsilon E^2 \times Volume$ ) gives rise to the polar instability of the whole system.

What is the energetically most favorable way to resolve the polar instability? This question actually represents the essence of the debate about two doping mechanisms (charge transfer and formation of oxygen vacancies). In this chapter, we have studied ideal interfaces with charge transfer and atomic relaxation. When the thickness  $m$  of LAO thin films is greater than four, the uncompensated internal electric field leads to occupied O<sub>2p</sub> bands at a  $p$ (or pseudo- $p$ ) interface rising in energy and crossing unoccupied Ti<sub>3d</sub> bands at an  $n$  interface. Charge transfer therefore occurs and interfaces become conducting. If we assume ideal interfaces, our DFT calculations support the charge transfer doping mechanism.

However, the interfaces can not be ideal. It is not because of any deficiency of the experimental techniques, but is an intrinsic limitation. For ideal interfaces, all theoretical studies (including our DFT calculations in this chapter) agree that there should be a large internal electric field which can be suppressed by charge transfer. However, all the studies ignore a simple fact: the internal electric field can not be fully compensated by the charge transfer so a residual internal electric field exists. For example, as shown in Figure 3.8, although the charge transfer indeed happens for LAO thin films with  $m=5$ , the residual internal electric field indicated by the core level shift of O<sub>2s</sub> does not vanish. It is of order 1V/unit cell. (If we assume charge transfer indeed occurs for ideal LAO thin films thicker than 3 unit cells, the residual internal electrostatic potential at least exceeds the bandgap of the STO substrate,  $3.2V/3$  unit cell  $\sim 1V$ /unit cell). Such a large residual internal electric field will result in a large electrostatic energy  $\frac{1}{2}\epsilon E^2 \times Volume \cong 0.3eV$  per unit cell, which is much larger than other characteristic energies such as thermal energy  $kT \sim 0.03eV$

and chemical potential dependence on oxygen pressure. In short, despite that we consider charge transfer, the residual electric field (or the accompanying electrostatic energy) is so large that the ideal interfaces can not be stable.

Since charge transfer is not an energetically favorable way to resolve the polar instability, we need to take oxygen vacancies and other defects into consideration. A major task of chapter 4 and 6 is to deal with charge transfer and formation of oxygen vacancies and other defects within a single framework and then unravel their competition.



# Chapter 4

## Polarity-induced oxygen vacancies at $\text{LaAlO}_3|\text{SrTiO}_3$ interfaces

Using first-principles density functional theory calculations, we find a strong position and thickness dependence of the formation energy of oxygen vacancies in  $\text{LaAlO}_3|\text{SrTiO}_3$  (LAO|STO) multilayers and interpret this with an analytical capacitor model. Oxygen vacancies are preferentially formed at  $p$ -type  $\text{SrO}|\text{AlO}_2$  rather than at  $n$ -type  $\text{LaO}|\text{TiO}_2$  interfaces; the excess electrons introduced by the oxygen vacancies reduce their energy by moving to the  $n$ -type interface. This asymmetric behavior makes an important contribution to the conducting (insulating) nature of  $n$ -type ( $p$ -type) interfaces while providing a natural explanation for the failure to detect evidence for the polar catastrophe in the form of core level shifts.

### 4.1 Introduction

Extremely high carrier mobilities have recently been observed when interfaces consisting of  $\text{LaO}$  and  $\text{TiO}_2$  layers are formed between insulating  $\text{LaAlO}_3$  and  $\text{SrTiO}_3$  perovskites [1]. Even though the physical origin of this metallic behavior is still under debate [33–35, 37, 39, 40, 43], most experimental [23–28, 36, 38, 42, 47, 51, 70] and theoretical [44, 53, 60–62, 64, 68, 71, 72] studies have reached a consensus that the so-called *polarity discontinuity* between these materials plays a crucial role; in the absence of any relaxation mechanism, alternate stacking of positively ( $\text{LaO}^+$ ) and negatively ( $\text{AlO}_2^-$ ) charged layers on the non-polar STO substrate would give rise to a huge effective internal electric field, leading to a divergence of the electrostatic potential with increasing thickness of LAO. Reflecting general developments in the field of polar oxides [73], three mechanisms have been suggested to avoid this instability: charge transfer [33], atomic relaxation [44, 51, 53, 60, 70, 71], or the creation of oxygen vacancies [35, 39] and other defects [38, 40].

The first mechanism refers [33] to the transfer of electrons from a surface  $\text{AlO}_2$  layer to the interface  $\text{TiO}_2$  layer by the internal electric field. The excess charge at the interface balances the polar discontinuity and leads to conducting behavior of the interface. This mechanism is strongly supported by the observation of an

insulator-metal transition induced by either an external electric field or by increasing the thickness of the LaAlO<sub>3</sub> layer [24]. However, direct experimental evidence of charge transfer, in the form of core level shifts, has not yet been found [37, 43]. The insulating behavior of the *p*-type interface [1] is also not readily accommodated in this picture.

The second mechanism, atomic relaxation in the presence of the internal electric field, that is analogous to the buckling of Ti-O-Ti chains in an external field in SrTiO<sub>3</sub>, has been discussed by a number of authors [44, 51, 53, 60, 70, 71]. It can eliminate the diverging potential by introducing a compensating electric field. A third way to resolve the polar instability is to introduce defects at interfaces. Oxygen vacancies (and other defects) created during the growth of LAO on STO are invoked by Herranz *et al.* [35] and Kalabukhov *et al.* [39] to understand the high mobility carriers. The long-relaxation time of the electric-field-induced insulator-metal transition [27] suggests the possibility of interface defect diffusion.

While the first two mechanisms have received much theoretical attention [44, 53, 60–62, 64, 68, 71], the relationship between the creation of defects and polarity has not been clarified theoretically. To demonstrate the coupling of polarity and oxygen vacancy formation and throw some light on the interplay with atomic relaxation and charge transfer, we calculate from first-principles the formation energy of oxygen vacancies in LAO|STO multilayers as a function of their location in the multilayer.

## 4.2 Method

We focus on (*m, m*) LAO|STO multilayers containing *m* layers each of LAO and STO with alternating *p*- and *n*-type interfaces. Because samples are grown on STO substrates, we fix the in-plane lattice constant at the calculated equilibrium value of STO and calculate the out-of-plane lattice constant by minimizing the total energy of strained bulk LAO. Oxygen vacancies are modelled in a 2 × 2 lateral supercell and for each vacancy position all atoms are allowed to relax with the volume of the structure fixed. Most of the results reported below were obtained with the 159 atom 2 × 2 × (4, 4) supercell depicted in Figure 4.1 containing a *p* and *n* interface. The periodically repeated single oxygen vacancy in a layer consisting of 2 × 2 unit cells should be compared to the ~25% oxygen vacancy concentration in a layer suggested by experiment [33]. The local density approximation (LDA) calculations were carried out with the projector augmented wave method [74] as implemented in the Vienna Ab-initio Simulation Package (VASP) [75]. A kinetic energy cutoff of 500 eV was used and the Brillouin zone of the 159 atom supercell was sampled with an 8 × 8 × 2 k-point grid in combination with the tetrahedron method. Inclusion of correlation effects (LDA+U) would modify the electrostatic potential profile slightly but not change our main conclusion which is dominated by the polarity of the system.

In thermodynamic equilibrium, the concentration of oxygen vacancies is determined by the free energy for vacancy formation,  $\Omega^{\text{Vac}} = E_{\text{SC}}^{\text{Vac}} - E_{\text{SC}} + \mu_{\text{O}}(T, p_{\text{O}_2})$  [76, 77]. The energies *E* can be calculated from first principles and in the present

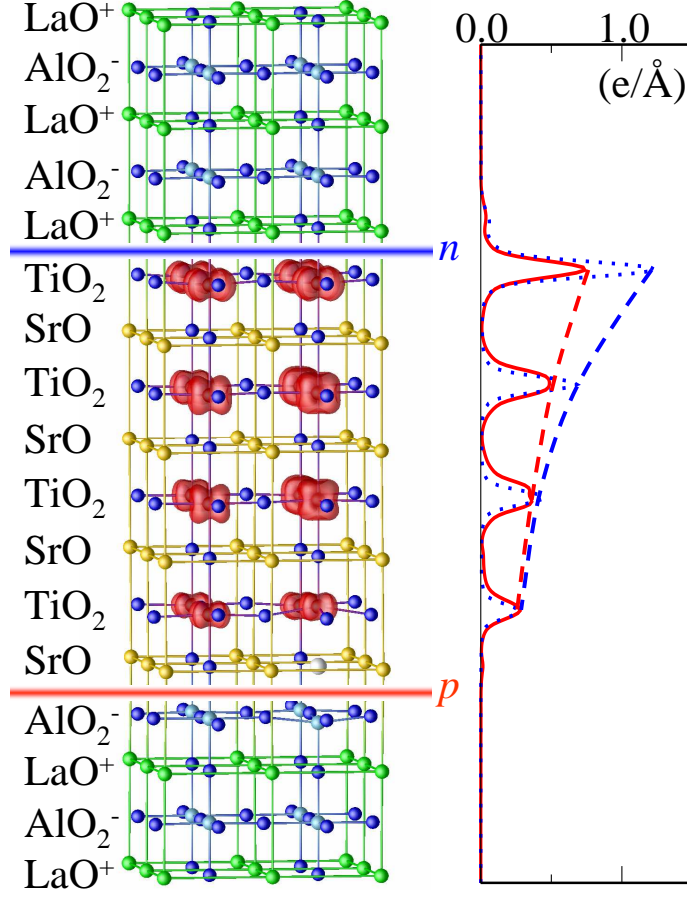


Figure 4.1: Left panel: the unit cell of a  $2 \times 2 \times (4 + 4)$  LAO|STO multilayer with an oxygen vacancy at the  $p$ -type interface. Blue spheres represent oxygen atoms and the oxygen vacancy is marked by a white sphere. Charge density isosurfaces corresponding to a value of  $0.015 e/\text{\AA}^3$  for occupied states in the conduction bands are coloured red. Right panel: plane-averaged charge density as a function of  $z$  for oxygen vacancies at  $p$ - (red) or  $n$ - (blue) type interfaces.

case where we use periodic supercells,  $E_{\text{SC}}^{\text{Vac}}$  and  $E_{\text{SC}}$  are the energies of supercells with and without an oxygen vacancy.  $\mu_{\text{O}}(T, p_{\text{O}_2})$  is the chemical potential of oxygen that depends on the temperature  $T$  and oxygen pressure  $p_{\text{O}_2}$  during growth or annealing. Unfortunately, there is no reliable way of determining the absolute value of  $\mu_{\text{O}}$  during LAO thin film growth by pulsed laser deposition. However, thin films of STO grown on STO substrates under the same experimental conditions as LAO thin films on STO can be used as a reference system to study oxygen vacancies [35, 39, 52]. In this paper we define the formation energy of an oxygen vacancy in an LAO|STO multilayer with respect to that in bulk STO,  $\Delta\Omega^{\text{Vac}} = \Omega_{\text{LAO|STO}}^{\text{Vac}} - \Omega_{\text{STO}}^{\text{Vac}}$ . If we assume that the oxygen chemical potential  $\mu_{\text{O}}$  for LAO thin film growth is the same as that during growth of STO thin films under the same experimental conditions, then the oxygen chemical potentials  $\mu_{\text{O}}$  cancel in the expression for  $\Delta\Omega^{\text{Vac}}$  that then



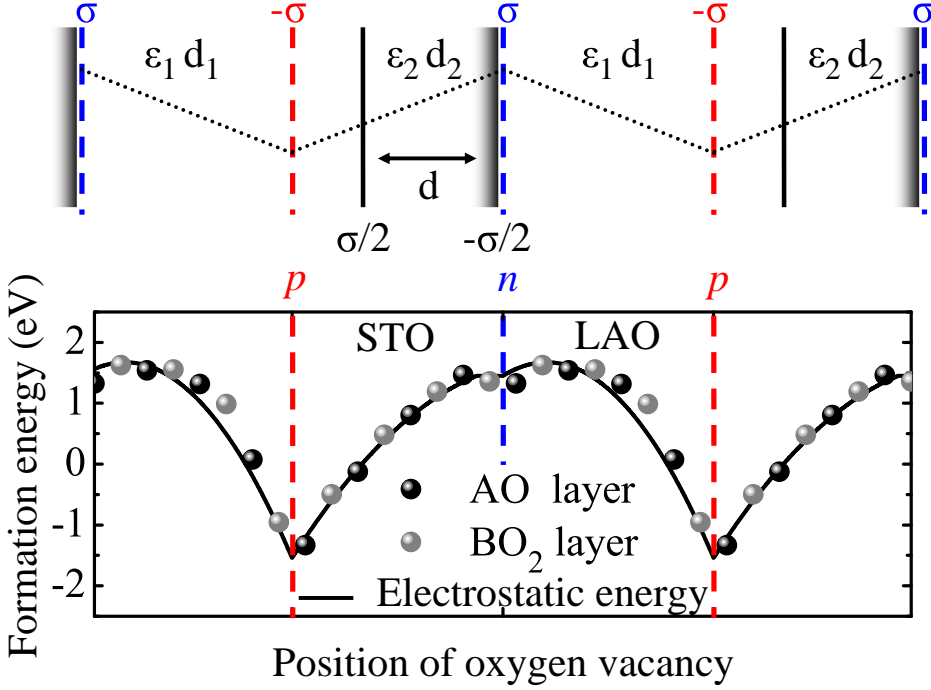


Figure 4.2: Position dependence of the formation energy of an oxygen vacancy in a  $2 \times 2 \times (4 + 4)$  LAO|STO multilayer calculated from first principles without relaxation (symbols) and using an analytical capacitor model (solid line).  $n$  and  $p$  interfaces are indicated by vertical red and blue dashed lines. A schematic diagram of the capacitor model is shown in the upper panel. The electrostatic potential profile for the vacancy-free structure is shown as a dotted line. The vertical black line at a distance  $d$  from the  $n$  interface represents the oxygen vacancy layer. Two excess electrons are transferred to the TiO<sub>2</sub> layer at the  $n$  interface (shaded grey line).

describes oxygen vacancy formation induced by LAO with reference to STO. It is worth noting that though  $E_{\text{STO}}^{\text{Vac}}$  converges only slowly with the size of supercell [78], this does not alter the conclusions we will draw.  $\Delta\Omega^{\text{Vac}}$  will be seen to span a range of  $\pm 1.0$  eV as a result of polarity and this range is much larger than the uncertainty in  $E_{\text{STO}}^{\text{Vac}}$  which is converged to  $\pm 0.09$  eV.

### 4.3 Results

We begin by calculating  $\Delta\Omega^{\text{Ov}}(z)$  as a function of the position ( $z$ ) of an oxygen vacancy without atomic relaxation. The most striking feature of the results shown in the lower panel of Figure 4.2 is the asymmetry for forming a vacancy at the  $n$  and  $p$  interfaces.  $\Delta\Omega^{\text{Ov}}$  is lowest when the oxygen vacancy is at the  $p$  interface, highest close to the  $n$  interface and is nonlinear in  $z$ . It spans a range of about 3 eV between the two interfaces and differs in the LAO and STO layers. We can capture the essential behaviour of  $\Delta\Omega^{\text{Ov}}(z)$  in terms of a modified parallel-plate capacitor

model.

### 4.3.1 Parallel capacitor model

The average electrostatic potential of defect-free LAO|STO multilayers, as probed by the energy levels of core states in LDA calculations, exhibits a simple symmetric triangular form as if the  $n$  and  $p$  interfaces were positively and negatively charged with charge density  $\pm\sigma = \mp e/a^2$  where  $a$  is the lattice constant of bulk STO. As sketched in the top panel of Figure 4.2, the plates of the capacitor are separated by a thickness  $d_1$  ( $d_2$ ) of insulating LAO (STO) with dielectric constants  $\epsilon_1$  ( $\epsilon_2$ ) determined by the electronic polarization only in the absence of ionic relaxation. Such a model was recently used to describe the evolution of the dielectric properties of LAO|STO multilayers with increasing layer thickness resulting in an insulator-metal transition [68]. Based on this simple capacitor model, the estimated internal electric fields are huge,  $\frac{1}{\epsilon} 1.2 \times 10^{11} \text{V/m}$  or  $\sim 0.9 \text{V/unit cell}$  in LAO, and the electrostatic potential (dotted line in Figure 4.2) diverges with increasing thickness of LAO.

We extend this model to encompass the layer of vacancies constructed in our supercell approach. Because oxygen is divalent, removal of a neutral oxygen atom in a bulk insulating material such as LAO or STO leaves two excess electrons in the conduction band weakly bound to the oxygen vacancy. In an LAO|STO multilayer, the potential energy of the electrons in the internal electric field far exceeds this binding energy and the total energy can be reduced by moving the two electrons to the conduction band minimum at the  $n$  interface leaving a sheet of positive charge at the oxygen vacancy plane a distance  $d$  away. Assuming that the excess electrons are on Ti ions at the  $\text{TiO}_2|\text{LaO}$  interface, independent of where the oxygen vacancies were formed, we can calculate the  $d$  dependent change in the electrostatic energy to be  $\frac{\sigma^2/\epsilon_0}{d_1\epsilon_2+d_2\epsilon_1} \{-d_1 + \frac{\epsilon_1}{\epsilon_2}(d_2 - d)\}d$ . It comprises two parts: the energy to insert a sheet of positive charge density  $\sigma/2$  in the LAO|STO capacitor background,  $-\frac{2\sigma^2/\epsilon_0}{d_1\epsilon_2+d_2\epsilon_1}d_1d$ , and the potential energy of the positively and negatively charged sheets  $\frac{\sigma^2/\epsilon_0}{d_1\epsilon_2+d_2\epsilon_1} \{d_1 + \frac{\epsilon_1}{\epsilon_2}(d_2 - d)\}d$ . The calculated LDA core level shifts of  $\sim 0.9\text{V/unit cell}$  can be used to estimate  $\epsilon_1 + \epsilon_2 \sim 52$  leaving one free parameter in the model, the ratio  $\epsilon_2/\epsilon_1$ . Taking this to be 1.5 results in the solid curve in Figure 4.2. The good fit of this simple model makes it clear that the internal fields induced by the polar layered structure can lower the formation energy of oxygen vacancies at the  $p$  interface very substantially and that the origin of the asymmetry between LAO and STO (the lack of reflection symmetry in the vertical dashed lines in Figure 4.2) is the difference in their dielectric constants. The residual interaction between the field-ionized oxygen vacancies and electrons accounts for the nonlinear behavior of the formation energy.

### 4.3.2 Atomic relaxation

Atomic relaxation can be expected to strongly suppress the polarity. Nevertheless, when our structures are fully relaxed, some essential features of  $\Delta\Omega^{\text{Ov}}(z)$  are un-

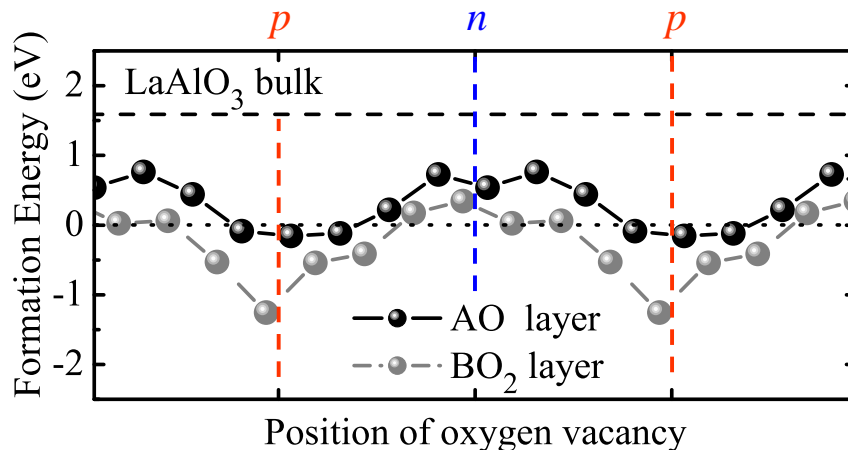


Figure 4.3: Position dependence of the formation energy of an oxygen vacancy in a  $2 \times 2 \times (4 + 4)$  LAO|STO multilayer relative to that of a vacancy in bulk STO (horizontal dotted line) calculated from first principles with relaxation. Black and grey symbols are for vacancies in AO and  $\text{BO}_2$  layers respectively. The formation energy of an oxygen vacancy in bulk LAO is shown as a dashed horizontal line.

changed, see Figure 4.3. In particular, the formation energy has a minimum at the  $p$  interface and a maximum close to the  $n$  interface while the minimum formation energy is more than 1 eV lower than in bulk STO. Including atomic relaxation differentiates between vacancy formation in AO and  $\text{BO}_2$  layers; the latter are energetically more favourable though the behaviour as a function of  $z$  is essentially the same. The lower formation energy in  $\text{BO}_2$  layers can be understood in terms of the types of relaxations possible within the constraints imposed by stacking the different layers in a multilayer. To simplify the discussion, we focus on the *less* favourable case of oxygen vacancies in AO layers so that our conclusions will also be applicable for  $\text{BO}_2$ -layer vacancies.

### 4.3.3 Critical thickness

For a capacitor with fixed charge density  $\sigma$ , the electric field is constant and the electrostatic potential increases as the plate separation (LAO thickness) is increased, a feature that is supported by both experimental [24, 27] and theoretical [44, 53, 60, 68, 71] studies. Because of its dependence on the electrostatic potential, we expect the formation energy of oxygen vacancies to depend on the multilayer thickness. Since the minimum and maximum formation energies occur at or close to the  $p$  and  $n$  interfaces, respectively, we focus on these formation energies. We further assume equal thicknesses  $m$  of the STO and LAO layers and plot  $\Delta\Omega^{\text{Ov}}$  as a function of  $m$  in Figure 4.4. At the  $n$  interface it is almost constant in value and  $\sim 0.6$  eV higher than for bulk STO. At the  $p$  interface however, it decreases with increasing  $m$  and becomes negative for a critical value of  $m$  between 3 and 4. Thus, for  $m \geq 4$  oxygen vacancies are preferentially formed at  $p$  interfaces rather than in the bulk of the

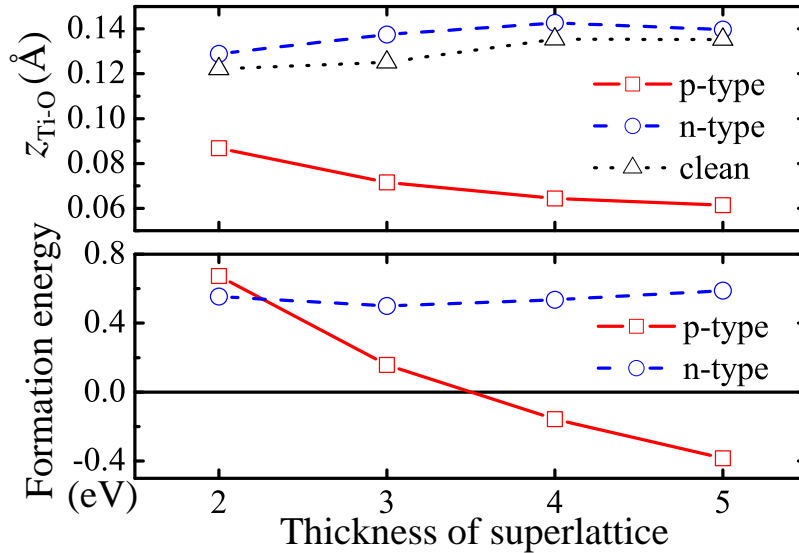


Figure 4.4: Upper panel: projection of the Ti-O-Ti separation along the  $z$  direction due to buckling for clean interfaces ( $\Delta$ ) and when vacancies are formed at the  $p$  ( $\square$ ) and at the  $n$  ( $\circ$ ) interface. Lower panel: formation energy of an oxygen vacancy as a function of the multilayer thickness for  $p$  and  $n$  interfaces in a  $2 \times 2 \times (m + m)$  LAO|STO multilayer with relaxed structure.

materials or at the  $n$  interface. The existence of a critical thickness is evidence for “uncompensated polarity” in thin LAO [79].

For an ideal LAO|STO multilayer without oxygen vacancies, the *zigzag* buckling of Ti-O-Ti and Al-O-Al chains will act to quench the internal electric field [44, 51, 53, 60, 68, 71]. Since oxygen vacancies at a  $p$ -type interface accompanied by charge transfer can strongly suppress polarity, they should also suppress Ti-O ferroelectric type buckling. Figure 4.4 shows that this is indeed the case. Oxygen vacancies at a  $p$ -interface suppress the buckling strongly while vacancies at an  $n$ -interface do not. The core level shifts, which represent the internal electric field, are reduced from 0.9 to 0.15 V/unit cell; the shift of  $\text{O}_{2p}$  states shown in Figure 4.5 is small. In this sense, oxygen vacancy formation, charge transfer and atomic relaxation act together in response to polar catastrophe.

#### 4.3.4 Electronic structure

A single oxygen vacancy donates two electrons to the system and the distribution and character of these excess electrons will dominate its transport properties. In a clean LAO|STO multilayer, the electrostatic potential at the  $p$  interface is lower than at the  $n$  interface so even if oxygen vacancies are generated at the  $p$  interface, the excess electrons will be driven by the electrostatic potential to the  $n$  interface, as shown in Figure 4.5. The charge distribution of the occupied conduction band states is plotted in Figure 4.1. Consistent with previous studies [47, 64], these have Ti  $d_{xy}$ -orbital character if the Ti ions are close to the interface, otherwise they consist

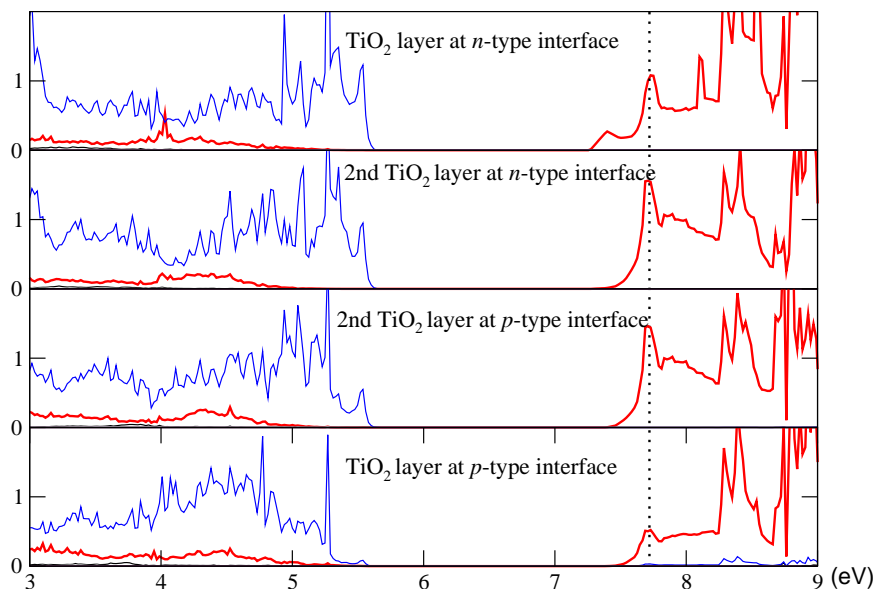


Figure 4.5: Layer projected density of states with an oxygen vacancy at the  $p$ -type interface. Fermi level is marked by a vertical dashed line.

of a mixture of Ti  $d_{xz}$ - and  $d_{yz}$ -orbital character. Though the introduction of oxygen vacancies represents a major change to the atomic structure, the change to the electronic structure is minor compared to a clean LAO|STO multilayer with only  $n$ -type interfaces.

## 4.4 Discussion

Even though it is energetically favourable to form oxygen vacancies at a  $p$  interface, the excess electrons are transferred to the  $n$  interface which will tend to be conducting while the  $p$  interfaces will be insulating. This asymmetry implies a spatial separation between impurity scattering and transport regions which, by analogy with proximity doping in semiconductor heterostructures, can give rise to a high mobility at LAO|STO interfaces. This result agrees with recent experimental data [33] which shows evidence for the presence of oxygen vacancies at the  $p$  interface while the mobile carriers are at the  $n$  interface.

The formation of oxygen vacancies can be suppressed by applying high oxygen pressures either during growth or in a post-growth anneal step. To confirm that polarity could induce oxygen vacancies at LAO|STO interfaces grown under high oxygen pressures of order  $10^{-3}$  mbar, we need to relate the calculated  $\Delta\Omega^{\text{Vac}}$  to thin film or multilayer growth conditions in a more practical way. As discussed in Section 4.2, the oxygen vacancy formation energy  $\Omega^{\text{Vac}}$  depends on the oxygen chemical potential  $\mu_{\text{O}}(T, p_{\text{O}_2})$  during growth or annealing. Even though the absolute value of  $\mu_{\text{O}}$  is unknown, its dependence on temperature and pressure is reasonably described by  $1/2kT \ln(p_{\text{O}_2})$  [77]. This tells us how raising the oxygen pressure increases the oxy-

gen chemical potential and suppresses the formation of oxygen vacancies. For example, STO thin films grown on an STO substrate at oxygen pressure above  $10^{-6}$  mbar are insulating while below  $10^{-6}$  mbar they are conducting. [39, 52] If we associate the conductivity with doping by oxygen vacancies, this implies that  $10^{-6}$  mbar is a threshold pressure for oxygen vacancy formation in STO thin films at which the formation energy becomes small enough to account for a measurable concentration of carriers. The smaller this threshold energy is, the closer  $\mu_{\text{O}}(p_{\text{O}_2} = 10^{-6} \text{ mbar})$  approaches  $E_{\text{STO}} - E_{\text{STO}}^{\text{Vac}}$ . Assuming the oxygen chemical potential for growth of LAO and STO thin films on STO is the same under comparable experimental conditions, we find  $\Delta\Omega^{\text{Vac}} = \Omega^{\text{Vac}}(p_{\text{O}_2} = 10^{-6} \text{ mbar})$  which implies that our calculated  $\Delta\Omega^{\text{Vac}}$  actually represents the energy to form oxygen vacancies at LAO|STO interfaces grown at an oxygen pressure of  $10^{-6}$  mbar. When the oxygen pressure is increased from  $10^{-6}$  to  $10^{-3}$  mbar, the increase in oxygen chemical potential and  $\Omega^{\text{Vac}}$  is only  $\sim 0.3$  eV which is still relatively small and only sufficient to compensate the polarity-induced reduction in vacancy formation energy at  $p$ -type interfaces when the LAO layer is very thin. Thus we argue that for LAO|STO interfaces grown or annealed at typical high oxygen pressures, the formation of oxygen vacancies induced by polarity of LAO cannot be excluded.

Though most experimental studies have been made [1, 24, 33] on samples consisting of STO substrates covered with several layers of LAO which only contain a single  $n$  interface, the conclusions of this paper about the position and thickness dependence of the formation energy of oxygen vacancies should be qualitatively applicable to the single interface case if we regard the surface of LAO as a pseudo- $p$  type interface [80–82]. Several experiments suggest [38, 40] the possibility of cation intermixing at interfaces. We calculated the energy cost of Sr-La interface mixing and found it to be energetically favourable at  $n$  interfaces. This implies that  $n$  interfaces should be rougher than  $p$  interfaces [33].

## 4.5 Conclusion

Using first-principles calculations, we show how oxygen vacancy formation, charge transfer and atomic relaxation in response to polar discontinuity at LAO|STO interfaces are strongly coupled. Oxygen vacancies are preferentially formed at  $p$  rather than  $n$  interfaces and the thickness-dependent formation energy provides an alternative explanation for the critical thickness observed in experiments while simultaneously explaining the failure to observe core level shifts. The conduction electrons produced when an oxygen vacancy is formed at a  $p$  interface move to the  $n$  interface where their interaction with the vacancies is minimal explaining the observed high mobilities.



# Chapter 5

## Electronic-structure-induced reconstruction and magnetic ordering at the $\text{LaAlO}_3|\text{SrTiO}_3$ interface

Using local density approximation (LDA) calculations we predict  $\text{GdFeO}_3$ -like rotation of  $\text{TiO}_6$  octahedra at the  $n$ -type interface between  $\text{LaAlO}_3$  and  $\text{SrTiO}_3$ . This results in a narrowing of the Ti  $d$  bandwidth by 1/3 so that LDA+U calculations predict an antiferromagnetic, charge- and spin-ordered groundstate for very modest values of  $U$ . Recent experimental evidence for magnetic interface ordering may be understood in terms of the close proximity of an antiferromagnetic insulating ground state to a ferromagnetic metallic excited state.

### 5.1 Introduction

Transition metal (TM) oxides in bulk form exhibit a huge range of physical properties. Heterostructures of TM oxides offer the prospect of greatly enhancing these properties or of combining them to realize entirely new properties and functionalities. The recent finding that a  $\text{TiO}_2|\text{LaO}$  interface between the insulating oxides  $\text{LaAlO}_3$  and  $\text{SrTiO}_3$  can be metallic with an extremely high carrier mobility [1] has triggered a surge of experimental and theoretical studies of this interface [23–26, 34–36, 38, 39, 53, 55]. The valence mismatch at the interface leads to the transfer of half an electron per unit cell from  $\text{LaAlO}_3$  (LAO: bandgap 5.6 eV) to  $\text{SrTiO}_3$  (STO: bandgap 3.2 eV), from the LaO interface layer to the  $\text{TiO}_2$  layer. For a defect-free interface, the concentration of these “intrinsic” sheet carriers is  $n_{\text{sheet}} \approx 3.3 \times 10^{14} \text{cm}^{-2}$ . For samples prepared under low oxygen pressure ( $< 10^{-4}$  mbar), the carrier density is much larger than this intrinsic value, suggesting their properties are determined by extrinsic carriers related to oxygen vacancies formed in the STO substrate during the growth of the LAO film.

Samples prepared under increasing oxygen pressure exhibit a large increase of



the sheet resistance [1, 25, 27, 35]. A sheet resistance which decreases on increasing the temperature from 10K to 70K, large negative magnetoresistance and magnetic hysteresis at low temperatures were found in Ref. [25] and these properties are presumably characteristic of intrinsic interfaces. The partial filling of the Ti  $d$  states at the  $n$ -type interface means that locally the electronic structure is intermediate between orthorhombic LaTiO<sub>3</sub> (Ti<sup>3+</sup>) and cubic SrTiO<sub>3</sub> (Ti<sup>4+</sup>). LaTiO<sub>3</sub> (LTO) is a G-type antiferromagnetic (AFM) Mott insulator with a Neel temperature of 146 K [16–18] and a band gap of 0.2 eV [19]. Compared to cubic STO, the additional electron in the  $t_{2g}$  conduction band state on the Ti ion leads to a GdFeO<sub>3</sub>-type crystal structure (space group  $Pbnm$ ) which can be derived from the ideal perovskite cubic structure by tilting essentially ideal TiO<sub>6</sub> octahedra about the  $\mathbf{b}$ -axis followed by a rotation about the  $\mathbf{c}$ -axis (see Figure 5.1). The La ions are displaced mainly along the  $\mathbf{b}$  axis with a small component along the  $\mathbf{a}$  axis [21, 22, 83].

In this paper we suggest that GdFeO<sub>3</sub>-type distortions at LAO|STO interfaces play an essential role in reducing the bandwidth of the occupied interface Ti  $d$  state by a third, making it more sensitive to on-site Coulomb correlations and stabilizing an antiferromagnetic ground state. Surprisingly little attention has been paid to the possibility of such distortions at the LAO|STO interface. Theoretical studies have been largely concerned with explaining the metallic behavior of  $n$ -type and the insulating character of  $p$ -type interfaces [53–55, 84, 85] with most emphasis being placed on the charge transfer between the LaO and TiO<sub>2</sub> interface layers.

Though LDA total energy calculations describe equilibrium crystal structures with good accuracy and have been applied extensively to non-metallic TM oxides [86], we are not aware of them being used to predict the structures of open shell correlated solids. To establish a predictive capability for the LAO|STO system, we carried out a systematic study of the crystal structure of the  $3d^1$  perovskites CaVO<sub>3</sub>, SrVO<sub>3</sub>, YTiO<sub>3</sub> and LaTiO<sub>3</sub>. We could show that LDA calculations reproduce the well-documented [87] GdFeO<sub>3</sub>-type distortions in this system very well. To study various types of magnetic ordering, we took account of the Coulomb interaction of the partially filled  $d$ -shell using a local Coulomb interaction parameter  $U_d^{\text{Ti}}$  [88] which has been shown to describe the ground state of YTiO<sub>3</sub> and LaTiO<sub>3</sub> qualitatively correctly [89]. The LDA+U results are in even closer agreement with experiment as shown in chapter 2.

## 5.2 Method

We model the LAO|STO interface using a periodically repeated  $(m, n)$  supercell containing  $m$  layers of LAO and  $n$  layers of STO. Most of the results to be reported below were obtained with the 40 atom  $c(2 \times 2) (\frac{3}{2}, \frac{5}{2})$  supercell depicted in Figure 5.1 containing two  $n$ -type interfaces, and did not change significantly when a  $(\frac{5}{2}, \frac{7}{2})$  supercell was used instead. To study AFM ordering the above supercell was doubled in the  $xy$  plane leading to a  $p(2 \times 2)$  unit cell containing 80 atoms.

The LDA and LDA+U calculations were carried out using the projector augmented wave (PAW) method [74, 75] and a plane wave basis as implemented in the

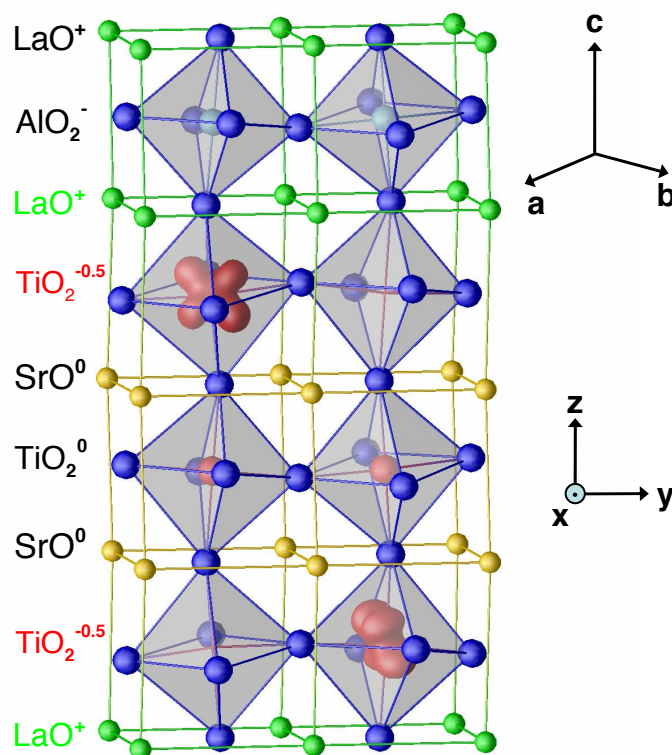


Figure 5.1: Relaxed  $\text{LaAlO}_3|\text{SrTiO}_3$  interface structure and charge density isosurface of the surplus electron for the charge ordered ferromagnetic state. The orthorhombic translation vectors are  $\mathbf{a}$ ,  $\mathbf{b}$ ,  $\mathbf{c}$ .

Vienna Ab initio Simulation Package (VASP) [90, 91]. A kinetic energy cutoff of 500 eV was used and the Brillouin zone of the 40 atom supercell was sampled with a  $6 \times 6 \times 4$  k-point grid in combination with the tetrahedron method [92]. Compared to the LDA, the LDA+U approach gives an improved description of  $d$  electron localization [88]. We use the rotationally invariant LDA+U method [9] with, unless stated otherwise,  $U_d = 5$  and  $J_d = 0.64$  eV for Ti  $d$  states. The La  $f$  states are forced to lie higher in energy by imposing a large  $U_f = 11$  eV and  $J_f = 0.68$  eV [93].

## 5.3 Results

### 5.3.1 Electronic structure

Because samples are grown on STO substrates, we fix the in-plane lattice constant at the experimental value for STO. This imposes a strain on LAO with a 3% smaller bulk lattice constant. Our starting point is a fully relaxed, tetragonal, non-magnetic metallic (RT-NMM)  $p(1 \times 1)$  configuration. We then remove symmetry constraints to obtain, in order of increasing energy gain (Figure 5.2a): a  $c(2 \times 2)$  distorted non-magnetic metallic (D-NMM) structure; a metastable spin-polarized, non charge-ordered (NCO) state, with a single interface-Ti charge state, obtained by

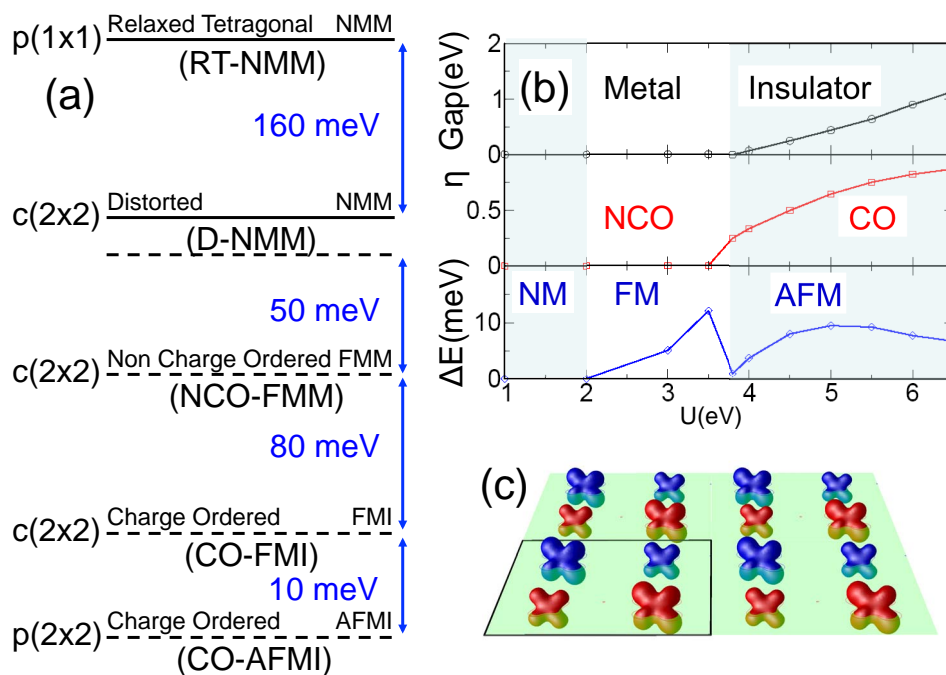


Figure 5.2: (a) Energy gained per surplus electron by relaxing symmetry constraints. The LDA+U energies (dashed lines) and energy differences calculated here with  $U_d = 5\text{ eV}$  depend on the value of  $U$  used and so are just indicative. (b) Phase diagram as function of value of  $U_d^{\text{Ti}}$ . Top: energy gap. Middle: disproportionation order parameter  $\eta = |n_1 - n_2| / (n_1 + n_2)$  where  $n_i$  is the occupation of the Ti  $d$  states on ion  $i$ . Bottom:  $\Delta E = |E_{\text{COFM}} - E_{\text{COAFM}}|$ . (c) Spatial magnetic distribution of the COAFM states ( $U_d = 4\text{eV}$ ) at the interface.

switching on  $U_d^{\text{Ti}}$ , a charge-ordered ferromagnetic insulating (CO-FMI) state with an energy gap of 0.44 eV in which the Ti sites are not equivalent (Fig. 5.1); a  $p(2 \times 2)$  charge-ordered anti-ferromagnetic insulating state (CO-AFMI).

The charge transferred from LAO to the smaller bandgap STO is bound close to the interface. As predicted by Okamoto and Millis [84] and confirmed for LTO|STO interfaces using calculations similar to those presented here [93], the effect of lattice relaxation is to smooth the potential discontinuity and allow charge to leak into the bulklike STO. For our NCO-FMM state, the occupied part of the bottom of the conduction band is almost 1eV wide and we confirm the occurrence of charge leakage at the LAO|STO interface.

The NCO-FMM state is unstable with respect to charge disproportionation [55] into inequivalent  $\text{Ti}^{3.2+}$  and  $\text{Ti}^{3.8+}$  interface ions as a result of the Coulomb repulsion and spin polarization on the Ti ions favoring integer occupancy; the transferred electron is localized on the nominally 3+ interface  $\text{Ti}^{3+}$  ions with little leakage into bulk STO (Figure 5.3). The atoms relax to accommodate the charge ordering: small displacements of the oxygen atoms surrounding the  $\text{Ti}^{3+}$  ion lead to that  $\text{TiO}_6$  octahedron expanding while the other one contracts. The combination of this distortion with the potential barrier and reduced symmetry at the interface

leads to one of the Ti  $t_{2g}$  states splitting off completely from the bottom of the STO conduction band and a gap opening up for quarter filling. The transferred electron remains strongly localized at the interface with essentially no leakage into the bulk layer. Because of the GdFeO<sub>3</sub>-type interface distortion, the occupied Ti  $t_{2g}$  state has  $0.35|xy\rangle + 0.14|yz\rangle + 0.92|xz\rangle$  orbital character (Figure 5.1).

In a  $p(2 \times 2)$  geometry, the kinetic energy can be further reduced by flipping the spins of equivalent Ti ions in a checkerboard pattern. The bandwidth is narrowed from 0.7 to 0.4 eV and the energy gap of the CO-AFMI state increased compared to the CO-FMI state. The total energy is lowered but the energy gain  $\sim 10$  meV is small, close to the limit of our accuracy.

The effect of varying  $U_d^{Ti}$  between 2 and 7 eV, keeping  $J$  fixed at 0.64 eV, is shown in Figure 5.2b. Between 3.5 and 4 eV, charge disproportionation takes place, AF ordering becomes more favourable and a metal insulator transition occurs. Increasing  $U_d$  leads to a larger CO gap and with increasing charge disproportionation the stripe charge and AF ordered pattern shown in Figure 5.2c evolves into a checkerboard pattern. The energy difference between CO-FMI and CO-AFMI states reaches a maximum at  $U_d = 5$  eV, the effect of increasing  $U$  being to suppress the exchange coupling between neighbouring spins. The most important result of this study is that the TiO<sub>6</sub> rotation reduces the bandwidth of the split-off band by about a 1/3 (consistent with results found for the bulk  $3d^1$  oxides, Ref. [87]) so that very modest values of  $U_d$  result in FM and AFM ordering and a metal insulator (MI) transition close to the FM-AFM phase boundary.

### 5.3.2 Atomic structure

Because the LAO lattice constant is 3% smaller than that of STO, LAO might be expected to shrink in the  $z$  direction when it is forced to match in-plane to STO. However, at the interface, we find that the La and Sr planes are separated by  $4.003\text{\AA}$  which is substantially larger than  $(3.905 + 3.789)/2$ , the arithmetic average of the LAO and STO lattice constants, and somewhat larger than the lattice constant of a fictitious cubic LTO phase with the same volume as the experimentally observed orthorhombic phase, but consistent with recent experiments [51]. By comparing results for  $(\frac{3}{2}, \frac{5}{2})$  and  $(\frac{5}{2}, \frac{7}{2})$  multilayers for the NCO-FMM and CO-FMI states, we find that the GdFeO<sub>3</sub> rotation of the TiO<sub>6</sub> octahedra is confined to the interface. The central STO (LAO) layers in the  $(\frac{5}{2}, \frac{7}{2})$  multilayers are essentially cubic (tetragonal). Compared to a bulk orthorhombic LaTiO<sub>3</sub> with an appropriately scaled lattice parameter, the shift of the La and Sr ions is reduced, presumably as a result of the constraints imposed by  $\frac{5}{2}$  or  $\frac{7}{2}$  layers of cubic STO and the availability of only half an extra electron in the Ti  $d$  states.

Previous LDA and LDA+U calculations found ferroelectric-like displacements of negatively charged O and positively charged Ti ions when the geometry was optimized for  $p(1 \times 1)$  structures [53, 93] resulting in a zigzag pattern of O-Ti-O-Ti-O Ti displacements perpendicular to the interface; see Figure 5.4b. Combining this with the GdFeO<sub>3</sub> rotation of the TiO<sub>6</sub> octahedra (Figure 5.4c) leads to the buckling

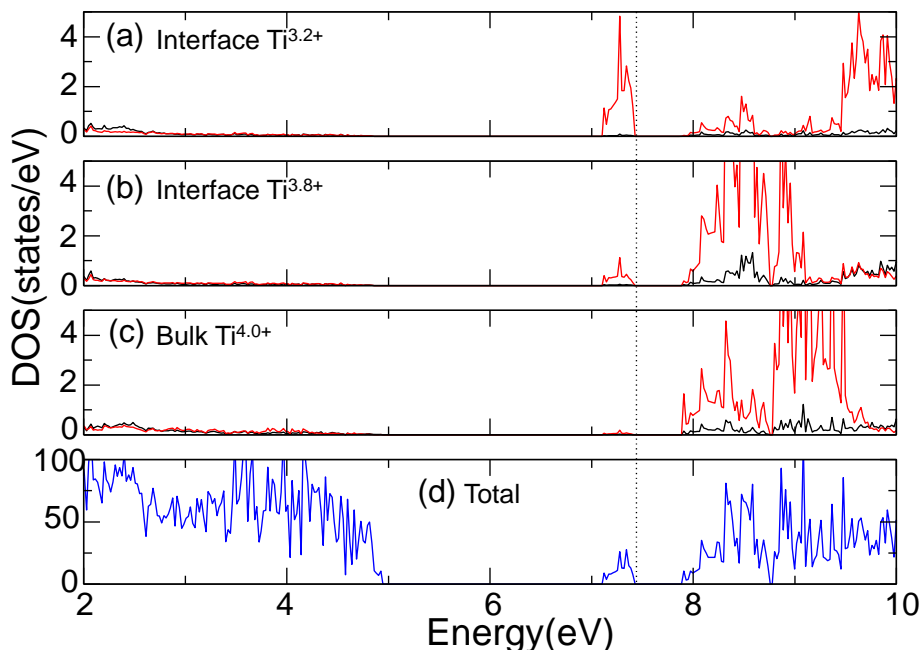


Figure 5.3: Interface densities of states (DoS) for the lowest energy charge ordered antiferromagnetic insulating (CO-AFMI) configuration. (a) and (b) projected  $3d$  DoS of (nominally)  $\text{Ti}^{3+}$  and  $\text{Ti}^{4+}$  interface Ti ions. The transferred electron has  $t_{2g}$  (red) character with the  $e_g$  states (black) far above the Fermi energy; (c) projected  $3d$  DoS of bulk  $\text{Ti}^{4+}$  ions; (d) total DoS.

pattern shown in Figure 5.4d in which one oxygen is displaced by  $\sim 0.15\text{\AA}$  out of an otherwise essentially linear chain.

### 5.3.3 Discussion

To understand the magnetoresistance results reported in Ref. [25], we must assume that we are just on the insulating side of the MI transition in Figure 5.2b i.e.,  $U_d^{Ti} \sim 4$  eV. Our calculations predict that the strong correlation of Ti  $d$  states will lead to electrons transferred from the LaO to the  $\text{TiO}_2$  layer being trapped on the interface Ti ions in an AFMI state. The localization of these intrinsic carriers would explain the high sheet resistance ( $> 10^4 \Omega/\square$ ) and low carrier concentration ( $\sim 10^{13} \text{cm}^{-2}$ ) of samples prepared at high oxygen pressure [1, 25, 34, 35]. The existence of a band gap would explain the decrease of sheet resistance with increasing temperature [25]. Application of an external magnetic field would force the AFMI system into a ferromagnetic insulating state with a smaller band gap, leading to a reduced resistance as observed.

This cannot be the whole picture, however. For example, a simple (doped) semiconductor model would predict carrier freeze-out at low temperatures and this is not observed. The role of oxygen vacancies as well as that of the cation mixing at the interface needs to be clarified. If we focus on the ideal of an intrinsic, abrupt in-

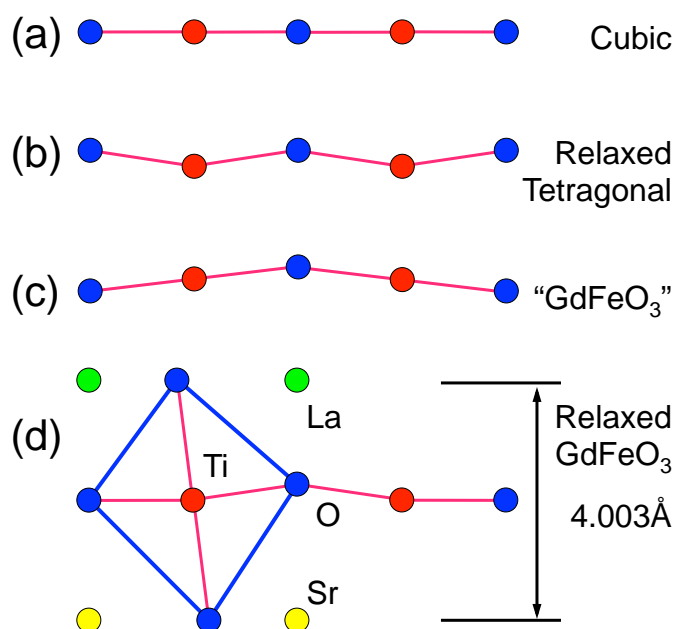


Figure 5.4: Sketch of the vertical displacement patterns of the Ti and O interface atoms for (a) an ideal cubic structure (b) a relaxed  $p(1 \times 1)$  structure (c) an ideal  $c(2 \times 2)$  “GdFeO<sub>3</sub>” structure and (d) the fully relaxed  $c(2 \times 2)$  “buckling” structure.

terface, perhaps the most pressing issue to be resolved experimentally relates to the appropriate value of  $U_d^{\text{Ti}}$  which is a free parameter in our otherwise parameter-free study. A spectroscopic study identifying the existence and size of the predicted CO gap would be invaluable for making further progress.

## 5.4 Summary and conclusions

Using LDA and LDA+U calculations, we have shown that the half electron (per interface Ti ion) transferred from the LaO layer on one side of an LAO|STO interface to the TiO<sub>2</sub> layer on the other side favors a rotation of TiO<sub>6</sub> octahedra just as it does in bulk LTO. As in bulk LTO, the distortion is crucial to the formation of a charge-ordered AFMI ground state and other charge, magnetic and orbital properties, and results in a characteristic buckling of the Ti-O-Ti bonding at the interface. Ionic relaxation plays a crucial role in determining the localization of the extra electron on the interface Ti ions and leakage into the bulk layer. However, charge ordering suppresses this leakage even when relaxation is included and, in the CO states the electrons are strongly localized at the interface. Our calculations suggest an explanation for recent experimental results in terms of the proximity of an AFMI ground state to a FMM excited state (or a FMI state with reduced band gap). With only half an electron trapped in an otherwise empty Ti  $d$  orbital, the LAO|STO interface is an attractive object for quarter-filled Hubbard model studies.



## Chapter 6

# Prediction of thickness limits of ideal polar ultrathin films

A central goal of current research is to realize ideal ultrathin films (one or a few atoms thick) with essentially intrinsic electronic properties without any atomic reconstruction or roughness. It is generally assumed that doing so is only limited by current experimental techniques and that ideal ultrathin films of any material could be made by improving these methods. In this chapter, we deal with the competition between electronic and atomic reconstruction in the growth of thin films of transition metal oxides and identify intrinsic limitations to this endeavour.

In particular, we use first-principles total energy calculations to study the growth of thin films of the polar infinite-layer copper oxide  $ACuO_2$  ( $A = Ca, Sr, Ba$ ) on a non-polar perovskite  $SrTiO_3$  substrate and predict a stoichiometric atomic reconstruction as a function of the film thickness. For fewer than about five unit cells of  $SrCuO_2$  on  $SrTiO_3$ , the widely assumed planar type thin film cannot be stabilized and a novel chain-type thin film becomes energetically favorable. This result is of interest to researchers working on the "polar catastrophe" issue in the  $LaAlO_3|SrTiO_3$  system (where a very recent development has been the introduction of  $SrCuO_2$  layers [94]) that has attracted many publications in high profile journals such as *Physical Review Letters*, *Science* and *Nature*.

However, the subject is much broader than this in two ways. One way is because of the relationship of  $ACuO_2$  to the high temperature cuprate superconductors which have been plagued by poorly understood growth problems. Our results identify two key ingredients that critically influence the growth of thin films of cuprate materials. The second way is because we are able to devise a simple model for our first principles calculations that interprets the numerical results in terms of charge transfer and strain. In this way, our numerical results are made accessible to a much wider audience and the applicability of those results is generalized so they can be applied to the interpretation of many other related materials systems.



## 6.1 Introduction

The lowering of symmetry at surfaces and interfaces frequently results in new or enhanced physical properties. A central goal of transition metal oxide thin film engineering is to exploit this by making interface effects dominate bulk properties in a controlled fashion [1, 84]. When a polar thin film is grown on a non-polar substrate, achieving this control can be very difficult because a polar instability arises that can drive and eventually be suppressed by electronic and atomic reconstruction. In the case of  $\text{LaAlO}_3$  (LAO) thin films grown on  $\text{SrTiO}_3$  (STO) substrates [1, 23–25, 27, 33], the alternate stacking of positively ( $\text{LaO}^+$ ) and negatively ( $\text{AlO}_2^-$ ) charged layers would result in huge internal electric fields if nothing else were to happen; the increasing electrostatic energy gives rise to a “polar instability”. The motion of electrons (charge transfer or leakage) and ions (atomic relaxation and reconstruction) generates compensating electric fields in response to the instability [33, 73, 95]. Whereas charge transfer and atomic relaxation result in atomically sharp interfaces and ideal thin films with essentially intrinsic properties [58, 62, 65, 68, 96, 97], atomic reconstruction can result in the formation of structures with entirely different intrinsic properties, or extrinsic atomic disorder and local stoichiometry change such as oxygen vacancy formation [35, 98] and ionic intermixing [40]. The competition between electronic charge transfer and atomic relaxation and reconstruction in oxide thin films is the source of much very puzzling behaviour [33, 35, 40, 98].

To unravel the details of this competition is a challenge for experiments because of the limited resolution of interface sensitive measurements and low visibility of oxygen atoms in most techniques [33]; it is also a challenge for theoretical studies to describe the nonstoichiometric atomic reconstruction that results from subtly different experimental conditions [27, 63, 65]. In this paper, we use first-principles total energy calculations to predict a stoichiometric atomic reconstruction in thin films of the polar infinite-layer copper oxide  $\text{ACuO}_2$  ( $A = \text{Ca}, \text{Sr}, \text{Ba}$ ) grown on a non-polar perovskite STO substrate. As the parent compound of cuprate high-temperature superconductors (HTS),  $\text{ACuO}_2$  has been intensively studied [99–101]. The recent discovery of a scavenging property of  $\text{SrCuO}_2$  (SCO) thin films [94] and theoretical proposal for electron-hole liquids [102] has led us to reexamine its structural and electronic properties. Our finding of chain-type formation in thin films as a result of a polar instability and atomic reconstruction provides a better understanding of the growth of thin films of cuprate HTS.

## 6.2 Method

We study  $\text{ACuO}_2$  thin films in three forms: grown on an STO substrate; in multilayers with STO; and freestanding. The thickness of  $\text{ACuO}_2$  is varied from one to six unit cells while keeping the STO thickness fixed at five unit cells. The in-plane lattice constants of all thin films are fixed at the equilibrium value of the bulk STO substrate calculated to be  $a_{\text{STO}} = 3.87\text{\AA}$  and all atoms are allowed to relax fully. The

local density approximation (LDA) calculations were carried out with the projector augmented wave method [74] as implemented in the Vienna Ab-initio Simulation Package (VASP) [75]. Using the generalized gradient approximation (GGA) does not change our main conclusions. To include correlation effects, we use the rotationally invariant LDA+U method [9] with  $U-J=6.5$  eV [103] for Cu  $d$  electrons.

## 6.3 Results

Bulk STO is a well-studied band insulator and a popular substrate for growing thin oxide films. It has a typical perovskite structure in which Sr and  $\text{TiO}_6$  form a CsCl lattice and the  $\text{TiO}_6$  unit consists of an oxygen octahedron with Ti at its center and the oxygen atoms at the centers of the Sr cube faces. Assigning the formal ionic charges  $\text{Sr}^{2+}$ ,  $\text{Ti}^{4+}$  and  $\text{O}^{2-}$ , it can be also be described as an alternate stacking of uncharged  $\text{SrO}^0$  and  $\text{TiO}_2^0$  layers [1].

The copper oxide  $\text{ACuO}_2$  with infinite layer structure [99] depicted in Figure 6.1 can be regarded as a defect perovskite with ordered oxygen vacancies. It consists of positively charged  $\text{A}^{2+}$  and negatively charged  $\text{CuO}_2^{2-}$  layers. Because all of the oxygen sites in the AO plane are vacant, there are Cu-O bonds in the  $xy$  plane but none in the  $z$  direction. The missing atoms and bonds lead to a reduction of the lattice constant in the  $z$  direction, reducing the symmetry from cubic in STO to tetragonal in  $\text{ACuO}_2$ . The lattice constant of  $\text{ACuO}_2$  increases as the ion radius increases in the series  $\text{A} = \text{Ca}, \text{Sr}, \text{Ba}$ . The calculated values given in the Table 1 agree well with experiment [100, 104] and  $\text{SrCuO}_2$  (SCO) is seen to have the smallest lattice mismatch with STO. Though a complex orthorhombic structure for SCO can also be synthesized [105], only the infinite layer structure is taken into consideration in thin film growth experiments [94, 101, 102, 106], thus we refer to the infinite layer structure as the bulk structure and neglect other possibilities in this paper.

Including an on-site Coulomb repulsion term  $U$  only slightly affects the calculated lattice constant, and can reproduce the observed antiferromagnetic insulator (AF-I) state [107] with an energy gap located between filled oxygen  $p$  bands and an unfilled spin minority Cu  $d_{x^2-y^2}$  band [103]. Because its nodes point toward neighbouring oxygen atoms, the  $d_{x^2-y^2}$  orbital hybridizes strongly with the oxygen  $p$  states and is pushed up in energy. The resulting  $\text{Cu}^{2+} d^9$  configuration corresponds to all Cu  $d$  orbitals being filled except for the minority spin  $d_{x^2-y^2}$  orbital. This is apparent in the surfaces of constant magnetization density plotted in Figure 6.1 where the spin density on the oxygen atoms also illustrates the AF superexchange coupling between neighbouring Cu ions. The hybridization is mainly confined to the  $\text{CuO}_2$  plane and does not affect the ionic character of the  $\text{A}^{2+}$  and  $\text{CuO}_2^{2-}$  layers so the polar instability of  $\text{ACuO}_2$  thin films still exists by analogy with LAO thin films.

### 6.3.1 Critical thickness of $\text{ACuO}_2$ ultrathin films

When SCO is grown on an STO substrate, it is usually assumed that positively charged  $\text{A}^{2+}$  and negatively charged  $\text{CuO}_2^{2-}$  layers alternate [101]. Because this

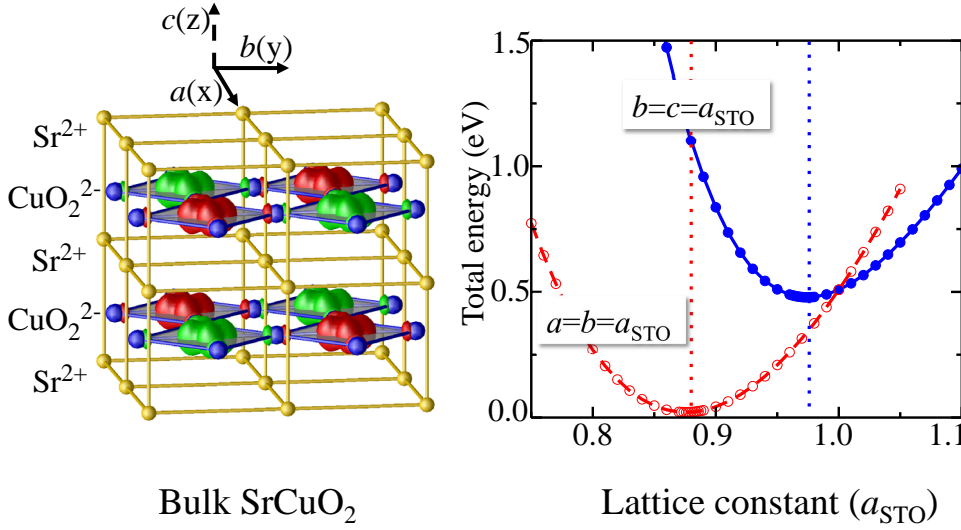


Figure 6.1: Left panel: bulk  $\text{SrCuO}_2$  with infinite-layer structure. Oxygen atoms are marked by blue spheres. Red and green represent surfaces of constant magnetization density but opposite sign. Right panel: the red curve illustrates the strain energy of bulk  $\text{SrCuO}_2$  on varying the lattice constant in the  $c$  direction keeping the in-plane lattice constants  $a$  and  $b$  fixed at  $a_{\text{STO}}$ . When the structure is rotated so that  $a$  and  $c$  are forced to match  $a_{\text{STO}}$  and  $a$  is varied, the resulting strain energy is given by the blue curve.

planar (“ $\text{CuO}_2$ ”) structure will lead to a polar instability, we also consider a chain type (“ $\text{CuO}$ ”) structure that is formed by moving one oxygen atom from the  $\text{CuO}_2^{2-}$  layer to the oxygen vacancy position in the  $\text{A}^{2+}$  layers as illustrated in Figure 6.2 for the case of  $\text{SCO}|\text{STO}$  multilayers. This results in a thin film consisting of uncharged  $\text{SrO}^0$  and chain-type  $\text{CuO}^0$  layers that does not suffer from a polar instability but at the expense of strain (Figure 6.1). For sufficiently thick films such as approaching bulk limits, we expect the planar structure to be most stable. It is not clear *a priori* what will occur for small values of film thickness  $d$ .

	$a^{\text{LDA}}$	$c^{\text{LDA}}$	$a^{\text{GGA}}$	$c^{\text{LDA}}$	$a^{\text{exp}}$	$c^{\text{exp}}$
$\text{SrTiO}_3$	3.87	3.87	3.95	3.95	3.905	3.905
$\text{CaCuO}_2$	3.77	3.08	3.87	3.20	3.853	3.177
$\text{SrCuO}_2$	3.84	3.38	3.95	3.47	3.926	3.432
$\text{BaCuO}_2$	3.92	3.68	4.03	3.84		

Table 1: Lattice constants of perovskite  $\text{SrTiO}_3$  and infinite layer copper oxides  $\text{ACuO}_2$  ( $\text{A}=\text{Ca}, \text{Sr}, \text{Ba}$ ).

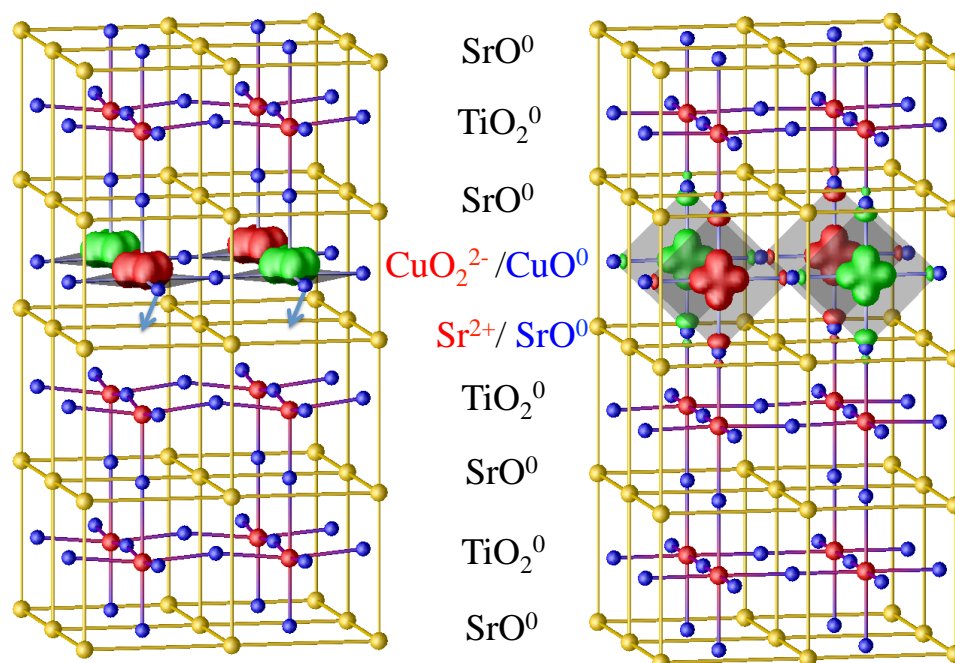


Figure 6.2: Relaxed structures and magnetic isosurfaces of SrCuO<sub>2</sub>|SrTiO<sub>3</sub> multilayers with one unit cell of planar- (left panel) or chain-type (right) SrCuO<sub>2</sub> thin film. For simplicity, only three unit cells of SrTiO<sub>3</sub> are shown. The arrows in the left panel schematically indicate the oxygen displacements that transform the planar into a chain-type structure.

To answer this question, we calculate the energy difference,  $\Delta E = E^{\text{chain}} - E^{\text{planar}}$  as a function of  $d$ . As shown in Figure 6.3,  $\Delta E$  depends strongly on both  $d$  and on the cation A. For SrCuO<sub>2</sub> thin films grown on a lattice matched STO substrate, it increases gradually from -1.2 to 0.05 eV per unit cell, as the thickness increases from one to six unit cells. Since both structures have the same stoichiometry, the sign of  $\Delta E$  is a direct measure of their relative stability. Below a critical thickness of about five unit cells, chain type thin films are energetically favorable; above it, planar type films are more stable. In the cation series Ca→Sr→Ba,  $\Delta E(d)$  decreases but depends on thickness in the same way for all ACuO<sub>2</sub> thin films. Similar behavior is found for multilayers and freestanding thin films so surface or interface effects can be excluded and we can decompose  $\Delta E(d)$  as  $\Delta E = E_C - E_P$ , where  $E_P$  denotes the electrostatic energy induced by the polar instability of planar type thin films;  $E_C$  denotes the chemical bonding energy caused by the oxygen atom moving to form a strained chain-type structure.

The planar thin films are terminated with positively charged Sr<sup>2+</sup> and negatively charged CuO<sub>2</sub><sup>2-</sup> surfaces with nominal area charge densities  $\pm\sigma = \pm e/a^2$  where  $a$  is the in-plane lattice constant. They can be modeled as parallel plate capacitors [33, 63, 65, 68, 73, 95, 102] in which the plates are separated by a thickness  $d$  of bulk material with dielectric constant  $\epsilon$ . The electrostatic energy density associated with the electric field  $\sigma/\epsilon\epsilon_0$  between the plates is  $E_p^0 = \sigma^2/(2\epsilon\epsilon_0)$  or approximately

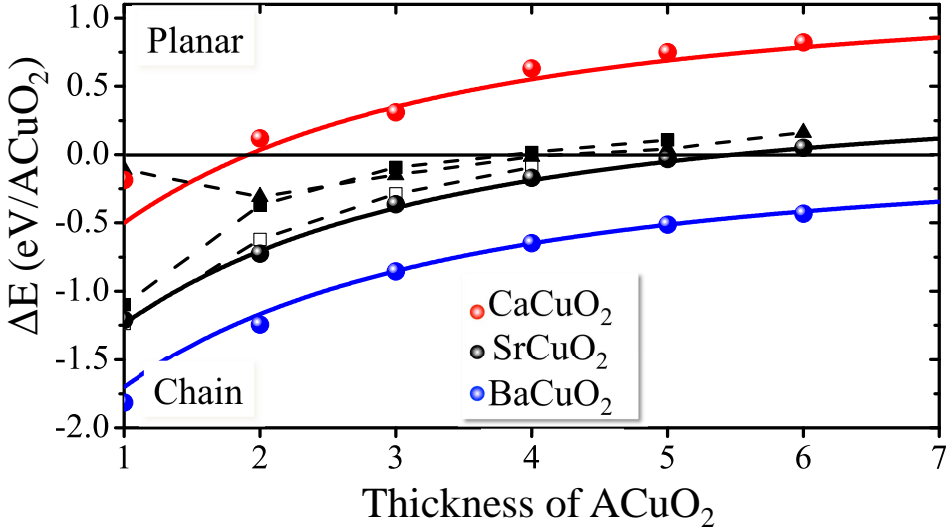


Figure 6.3: Total energy difference  $\Delta E(d)$  between planar and chain-type  $ACuO_2$  thin films as a function of the film thickness  $d$ . Symbols represent  $SrCuO_2$  thin films in three forms: grown on a  $SrTiO_3$  substrate (black spheres), as a multilayer with  $SrTiO_3$  (squares), and freestanding (triangles). The unfilled squares represent LDA+U results for the case of multilayers. The solid black line for  $SrCuO_2$  is based on an analytical model including the electrostatic energy and strain energy discussed in the text. The red and blue solid lines are just simple shifts of the fitting curve according to our calculated straining energies of  $CaCuO_2$  and  $BaCuO_2$ .

$20/\epsilon$  eV per unit cell, where  $\epsilon_0$  is the dielectric constant of vacuum. This reflects a strong polar instability that will drive and be eventually quenched by charge transfer that depends on the thickness and electronic structure of the thin films [102]. If we assume a rigid flat band approximation with constant density of states  $\alpha$ , the transferred charge is  $\sigma/[1 + a^2\epsilon\epsilon_0/(\alpha d)]$ . As a result of the screening by the transferred charge, the residual electrostatic energy becomes  $E_p(d) = E_p^0/[1 + \alpha d/(a^2\epsilon\epsilon_0)]^2$ , where the screening factor clearly depends on  $\alpha$  and thin film thickness  $d$ . For a large gap insulator with  $\alpha = 0$ ,  $E_p$  is a constant; for a good metal with a large  $\alpha$ ,  $E_p$  approaches zero. For a small band gap semiconductor with a moderate  $\alpha$ ,  $E_p$  vanishes when  $d$  is large, consistent with bulk limits; if  $d$  is reduced, less charge will be transferred and consequently  $E_p$  will be enhanced. When the films are sufficiently thin, charge transfer cannot take place to quench the polar instability.

In such a situation,  $E_p$  can instead be quenched by displacing oxygen atoms to form a chain-type structure. But doing this will change the bonding energy  $E_C$  because the structure that results corresponds to a strained  $ACuO_2$  thin film grown in a (100) orientation on a (001) STO substrate (rhs of Figure 6.2), rather than with a conventional (001) orientation (lhs of Figure 6.2). The two types of thin film only differ in terms of strain. To estimate the strain energy of planar type thin films, we fix the in-plane lattice constant of bulk  $ACuO_2$  at  $a_{STO}$  and minimize the total energy with respect to  $c$ . For chain type thin films, we consider  $b$  and  $c$  as the in-plane

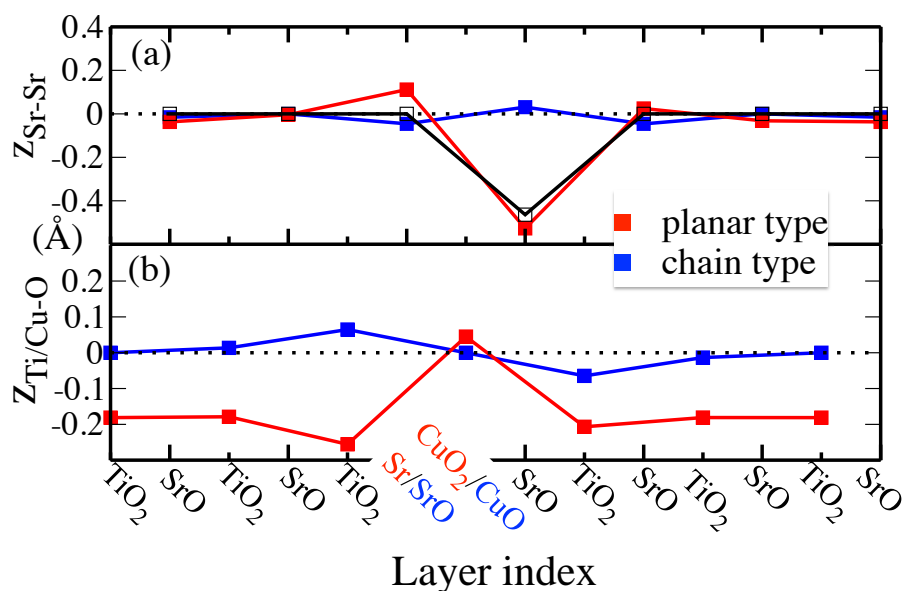


Figure 6.4: (a) Spacings between Sr layers for two types of SCO|STO multilayers in reference of  $a_{\text{STO}}$ . The black squares and line represents ideal stacking without epitaxial strain. (b) The Ti-O or Cu-O corrugation in the  $z$ -direction for each layer in both types of SCO|STO multilayers.

lattice constants, fix them to be equal to  $a_{\text{STO}}$  and minimize with respect to  $a$ , as shown in Figure 6.1. The energy difference per unit cell between the two minima is  $E_C = 0.45$  eV for SrCuO<sub>2</sub>, 1.19 eV for CaCuO<sub>2</sub>, and -0.01 eV for BaCuO<sub>2</sub>.

As shown in Figure 6.3,  $\Delta E(d)$  can be fit very well using  $E_C - E_P$  with values of  $\alpha = 0.1e/V$  and  $\epsilon = 8$  in the modified parallel plate capacitor model and  $E_C$  the calculated strain energy. The very good fit indicates that the competition between the two structures can be represented in terms of electronic and atomic reconstructions and that charge transfer can occur to partly screen the polar instability without altering the atomic structures. However, the screening effects will weaken as the films become thinner. For less than about five unit cells of SCO on STO, the widely assumed planar type thin film cannot be stabilized because of the polar instability. In spite of a considerable cost in strain energy, the chain type thin film should become energetically favorable because of the lowering of the electrostatic polarization energy  $E_P$ .

### 6.3.2 Atomic and electronic structure

To discuss the atomic and electronic properties of the novel chain-type thin films, we focus on the multilayers shown in Figure 6.2 with a single unit cell of SCO sandwiched between five unit cells of STO. By doing this, we avoid having to discuss the effect of dangling bonds at a free surface while the parallel behaviour of the curves (black spheres and squares) in Figure 6.3 indicates that the essential physics is the same. In the chain-type film, there are stiff Cu-O bonds in the growth direction.

Because of this, the multilayer containing chain-type SCO is almost 0.5 Å longer in the  $z$  direction than that containing planar SCO. This is illustrated in Figure 6.4(a) where the spacing between layers containing Sr atoms is plotted. Measurement of this spacing should be possible and would provide experimental evidence for chain type thin films. The strong zigzag Ti-O buckling evident in Figure 6.2 and 6.4(b) that is an indicator of internal electric fields [58, 63, 65, 68] in the planar-type films but is absent in the chain type films should also be observable.

The ground state of the planar-type film is an AF metal. The polar nature of thin films together with the existence of apical oxygen atoms and Cu-O-Ti type bonding scarcely change the  $d_{x^2-y^2}$  orbital character of at interfaces, consistent with a previous DFT calculation [108]. In contrast, the ground state of the chain type film is an AF insulator with a localized magnetic moment of  $0.6\mu_B$  on Cu ions and an enlarged energy gap. Because Cu ions are still in a  $\text{CuO}_4$  square planar configuration surrounded by four oxygen atoms in the  $y$ - $z$  plane rather than the original, bulk  $x$ - $y$  plane, the orbital character will be  $d_{z^2-y^2}$ , as shown in Figure 6.2. Our results suggest an explanation for the observed  $d_{3z^2-r^2}$  interfacial orbital at the YBCO|LMO interface [96]; the polar instability of  $\text{CuO}_2$  planes [102, 106, 109] may be driving oxygen atoms (or vacancies) to move and effectively tilt the  $\text{CuO}_4$  square toward  $z$  direction, which favors orbitals along  $z$  direction.

## 6.4 Conclusion

Using first principles calculations, we predict that a polar instability will lead to chain type structures of  $\text{ACuO}_2$  thin films when the films are sufficiently thin and interpret this with a parallel plate capacitor model including charge transfer. As the polar film is made thinner, less charge can be transferred and consequently the residual electrostatic energy increases. The enhanced polar instability will drive oxygen ions out of polar  $\text{CuO}_2$  planes resulting in chain type structures, out-of-plane Cu  $d$  orbital characters and an expanded epitaxial lattice constant. This result suggests that the polar nature of  $\text{CuO}_2$  planes may play a key role in the structure and properties of ultrathin films of high temperature superconducting cuprates.

# Chapter 7

## Magnetic phase diagram of FeAs based superconductors

The recently discovered high-temperature superconductivity in doped quaternary iron oxypnictides correlates experimentally with a magnetic instability. We have used first-principles calculations to determine a magnetic phase diagram of  $\text{Re}[\text{O}_{1-\delta}\text{F}_\delta]$  FeAs (Re=La–Dy) as a function of the doping  $\delta$ , of the FeAs in-plane lattice constant  $a$ , and of the distance between the Fe and As planes.

### 7.1 Introduction

The recent discovery of superconductivity in electron-doped  $\text{La}[\text{O}_{1-x}\text{F}_x]\text{FeAs}$  with a critical temperature ( $T_c$ ) of 26K [2] has stimulated a massive experimental [110–120] and theoretical effort [59, 121–133] to find other, higher  $T_c$  materials in this completely new family of iron-pnictide superconductors. The undoped parent compound  $\text{LaOFeAs}$  is a poor metal with an ordered antiferromagnetic (AFM) ground state [113, 116] but with increasing F doping [117] the magnetic ordering is suppressed and superconductivity emerges. This strongly suggests that magnetic fluctuations in the iron layers close to the quantum critical point (QCP) play a fundamental role in the superconducting pairing mechanism. Recent experimental [117–120] and theoretical [129–133] results also suggest that spin fluctuations in the vicinity of the QCP mediate the superconductivity as in the cuprates, heavy fermion materials, or ruthenates [134–136]. In view of this, so far empirical, correlation between superconductivity and QCPs, it is important to understand how the magnetic (in)stability depends on structural and chemical parameters that are accessible to experiment. That is the subject of this paper.

Superconducting  $\text{ReOFeAs}$  crystallizes in a tetragonal layered structure with  $P4/nmm$  symmetry and consists of layers of covalently bonded FeAs alternating with layers of more ionically bonded  $\text{ReO}$ . With eight atoms (two formula units) in the unit cell, it can be described using only two internal structural parameters in addition to the lattice parameters  $a$  and  $c$  [137]. One of the internal parameters,  $d_{\text{Fe-As}}$ , describes the separation between planes of Fe and As; the other,  $d_{\text{Re-O}}$ , be-



tween planes of Re and O. The excess electron from the ReO layer is donated to the FeAs layer which is metallic with a number of partly filled bands of mainly Fe  $3d$  character intersecting the Fermi energy [124, 138]. In addition to the four structural parameters, we define a doping  $\delta$  in terms of deviations from this ideal stoichiometry per Fe atom. Electron and hole doping can be achieved, for example, by partially replacing oxygen with fluorine [2] or trivalent La with divalent Sr [139].

Since mapping out the magnetic phase diagram in five dimensions is impossible, we need to identify a smaller number of key independent variables. Clearly the doping  $\delta$  is one. Although the interaction between the ReO and FeAs layers is by no means negligible, it is widely accepted that the superconducting properties of ReOFeAs emerge from the FeAs layers. The main role of the ReO layers is to determine the lattice parameters [137] and to contribute doping electrons while the magnetism and superconductivity are associated with the “active” FeAs layers so we fix  $d_{\text{Re-O}}$  and  $c$  at their calculated equilibrium values for undoped LaOFeAs. The in-plane lattice constant  $a$  and the separation between the Fe and As layers  $d_{\text{Fe-As}}$  [59, 126–128] are the other two key parameters we identify to construct magnetic phase diagrams in the  $(\delta, a = a_{eq}, d_{\text{Fe-As}})$  plane,  $(\delta = 0.3, a = a_{eq}, d_{\text{Fe-As}})$  and  $(\delta = 0.3, a, d_{\text{Fe-As}} = d_{eq})$  lines of this parameter space. We do this by calculating the energy  $E(\delta, a, d_{\text{Fe-As}})$  for non-magnetic (NM), checkerboard AFM (C-AFM) and stripe AFM (S-AFM) orderings, going considerably beyond existing attempts to determine the phase diagrams of FeAs-based materials as a function of doping or pressure [130, 133].

## 7.2 Method

The total energy calculations are carried out within the framework of density functional theory (DFT) using a spin polarized generalized gradient approximation (SGGA) for the exchange-correlation potential (PBE functional). The electronic ground state is calculated by solving the Kohn-Sham equations self-consistently with the projected augmented wave method (PAW) [74] and a cut off energy of 500 eV for the plane wave basis as implemented in the Vienna *ab initio* simulation package (VASP) [91]. The C-AFM and S-AFM states are described in a  $\sqrt{2} \times \sqrt{2} \times 1$  tetragonal structure. Though an orthorhombic distortion is observed [113, 126] for the S-AFM ordered state in the LaFeAsO parent compounds, it is suppressed by doping. Since we are mainly interested in locating the phase boundaries, it can be neglected. The Brillouin zone integrations are performed with the improved tetrahedron method [92] with a sampling grid of  $8 \times 8 \times 6$  k-points. When using pseudopotentials, it has been shown that it is necessary to treat the  $3p$  states of Fe as valence states to reproduce all-electron results [128]. Doping was modelled by adding or subtracting electrons and compensating their charges with a homogeneous fixed background charge [91]. This approximation was checked explicitly using supercell calculations in which a fraction of the oxygen atoms were replaced with fluorine, and proved not to be critical.

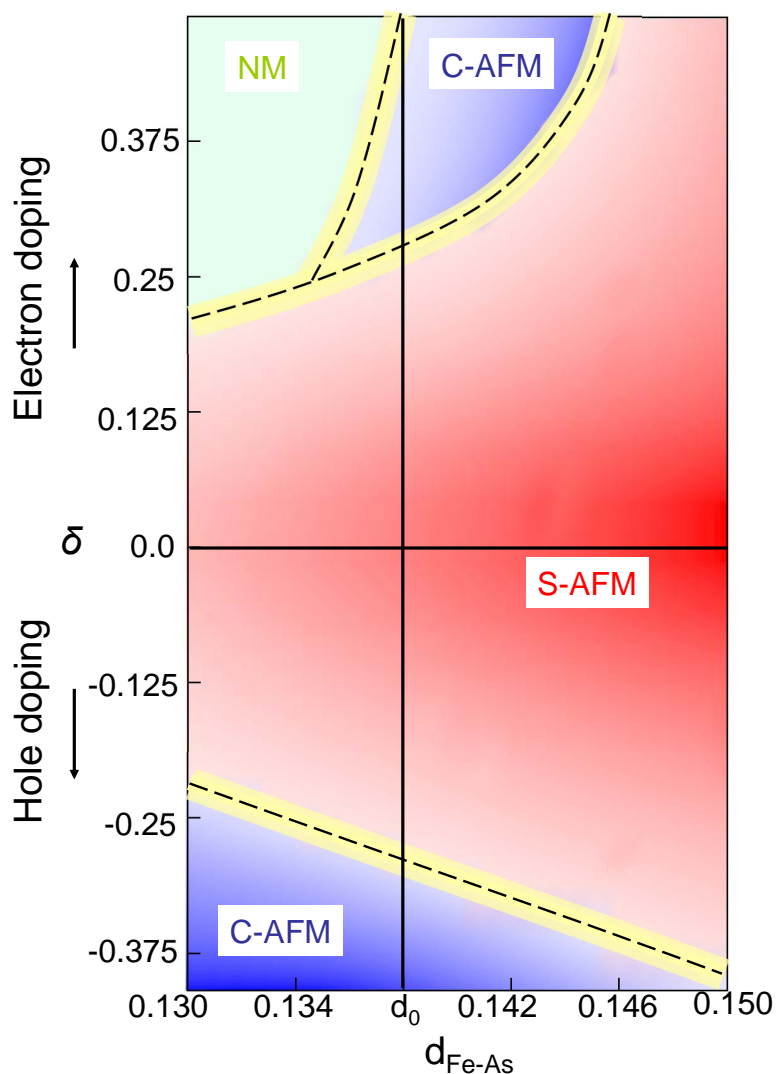


Figure 7.1: Phase diagram of LaOFeAs as a function of doping  $\delta$  and the distance between the Fe and As planes along the  $c$  axis,  $d_{\text{Fe-As}}$  (normalized by  $c$ ). Blue, red and green represent respectively checkerboard AFM (C-AFM), stripe AFM (S-AFM) and nonmagnetic (NM) ordering. In the AFM region, more stable magnetic ordering is described by darker color.  $d_0$  is the calculated equilibrium value of  $d_{\text{Fe-As}}$  for the undoped material.

## 7.3 Results

We begin by determining the ground state of LaOFeAs as a function of  $\delta$  and  $d_{\text{Fe-As}}$ . First of all the energy is minimized with respect to the internal structural parameters  $d_{\text{Fe-As}}$  and  $d_{\text{Re-O}}$  for the undoped parent compound LaOFeAs using the experimental  $a$  and  $c$ . This optimized structure is then frozen and the total energy calculated as a function of  $d_{\text{Fe-As}}$  and  $\delta$  for NM, C-AFM and S-AFM ordering. The phase diagram obtained from these energies is shown in Figure 7.1 where positive and negative  $\delta$  correspond to electron and hole doping, respectively. We propose that

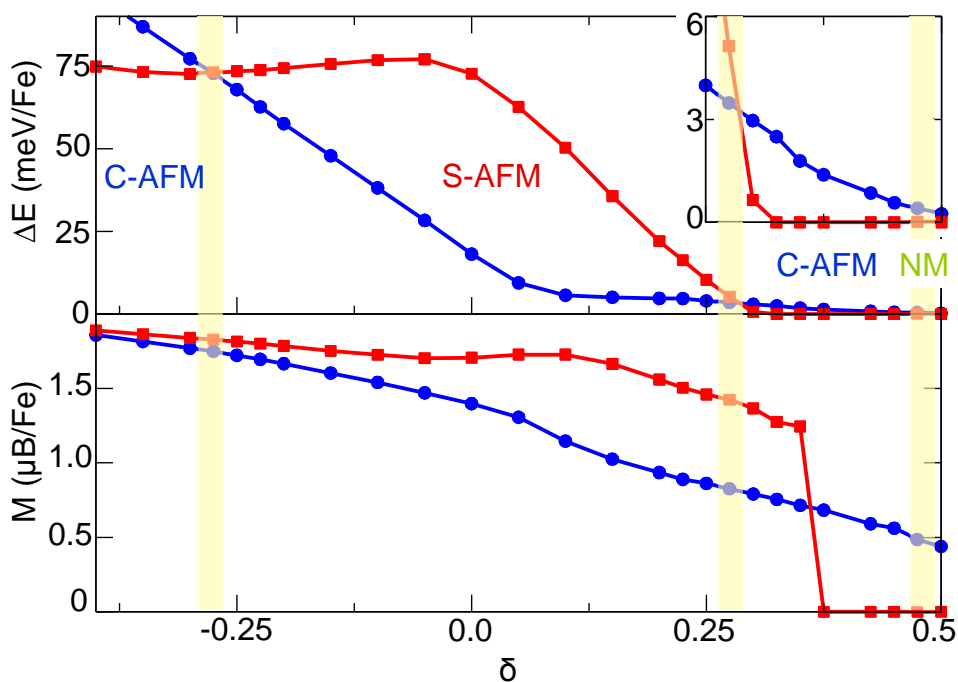


Figure 7.2: Magnetic stabilization energies relative to NM (a) and magnetic moment (b) per Fe atom of C-AFM and S-AFM ordered states as a function of doping for the vertical line  $d_{\text{Fe-As}} = d_0$  in Figure 7.1. The energy difference for high doping region is enlarged in the inset.

this phase diagram describes qualitatively all FeAs based materials since substituting different elements in the Re-O layers only changes the effective doping  $\delta$  and the lattice parameters  $a$  and  $c$ . The effect of changing  $c$ , for example by external uniaxial pressure, is given in our phase diagram in terms of its effect on  $d_{\text{Fe-As}}$ ; changing the Re position has otherwise little effect. The effect of changing  $a$  will be discussed below. Because our phase diagram is calculated as a function of two variables, the boundaries separating regions with different ground states, shown as dashed lines in Figure 7.1, are in general quantum critical *lines* (QCL). The uncertainty in the location of these quantum critical lines resulting from neglecting the effect of differential relaxation specific to the magnetic ordering and doping, and because the SGGA is not exact, is indicated by the broader yellow regions.

### 7.3.1 Effect of doping

The most notable feature of Figure 7.1 is the asymmetry of electron and hole doping. It shows a clear trend that hole doping stabilizes AFM ordering while electron doping weakens AFM ordering (also see in Figure 7.2a). The undoped material exhibits S-AFM ordering for all values of  $d_{\text{Fe-As}}$  (horizontal line,  $\delta = 0$ ) and S-AFM ordering is stabilized by increasing  $d_{\text{Fe-As}}$ . On doping LaOFeAs with electrons (vertical line,  $d = d_0$ ), the S-AFM ordering is weakened and a transition to C-AFM ordering is observed at  $\delta \sim 0.28$ . Furthermore, heavy electron doping will destroy the

AFM ordering and cause a phase transition from C-AFM to NM ordering at  $\delta \sim 0.5$ . The suppression of magnetic ordering by electron doping is consistent with previous first-principles calculations [130, 133]. When the structure is doped with holes, a transition to C-AFM ordering occurs at  $\delta \sim -0.28$ . Contrast to electron doping case, higher hole doping strengthens C-AFM ordering.

The magnetic phase transition with doping in Figure 7.1 implies that S-AFM and C-AFM ordered states have different dependence on doping. Then, we choose vertical line ( $d = d_0$ ) in Figure 7.1 as an example to investigate magnetic moments as well as energy as a function of doping, see Figure 7.2. A sequence of S-AFM  $\rightarrow$  C-AFM  $\rightarrow$  NM ground states is generated with increasing electron doping. For C-AFM ordered state, magnetic moment decreases smoothly with gradual decreasing of stabilization energy. For S-AFM ordered state with electron doping under  $\sim 0.4$ , magnetic moment reduces almost the same rate compared with C-AFM case while energy drops much faster. It should be noticed that though magnetic stabilization energy is rather small ( $< 3\text{meV}/\text{Fe}$ ) for S-AFM ordered state at high doping region (from  $\sim 28\%$  to  $\sim 40\%$ ), the magnetic moment is still large ( $\sim 1.4\mu_B$ ), which also implies magnetic instability is strong.

### 7.3.2 Density of states driven phase transition

Magnetic phase transition with doping can be understood in terms of the density of states (DOS) of the parent compound close to the Fermi level. We examine the Fe projected DOS shown in Figure 7.3 for C-AFM and S-AFM ordering for undoped and 30% electron doping. For both undoped AFM ordered states, the majority-spin states are located well below  $E_F$ , whereas most of the minority-spin states occur close to  $E_F$  and remain partially filled. This leads to doped electron has priority to occupied minority channel which results in magnetic moments reducing smoothly with electron doping. For S-AFM ordering, the Fermi energy in the undoped case is situated in a pseudogap for both spin channels. On doping with electrons, the pseudogap has to be crossed before a high density of mainly minority-spin states peak with  $d_{xy}$  character can be populated. This is energetically unfavourable. For C-AFM ordering, no such peak exists and the doping electrons can be accommodated in mainly minority-spin states close to the undoped Fermi level. Then, a clear physical picture can be drawn from point view of DOS: magnetic moments for C-AFM and S-AFM show similar behavior with doping while respective magnetic stabilization energies change is different significantly. This result strongly suggests that magnetic ordering in LaOFeAs is driven by DOS other than superexchange in cuprates.

### 7.3.3 Effect of $a$ and $d_{\text{Fe-As}}$

The effect of structure parameters  $a$  and  $d_{\text{Fe-As}}$  to the phase diagram at a fixed electron doping is shown in Figure 7.4. The main features of these phase diagrams are that the effect of increasing  $a$  is similar to that of increasing  $d_{\text{Fe-As}}$ : it stabilizes AFM ordering. For LaOFeAs with equilibrium lattice  $a_0$  at 0.3 electron doping

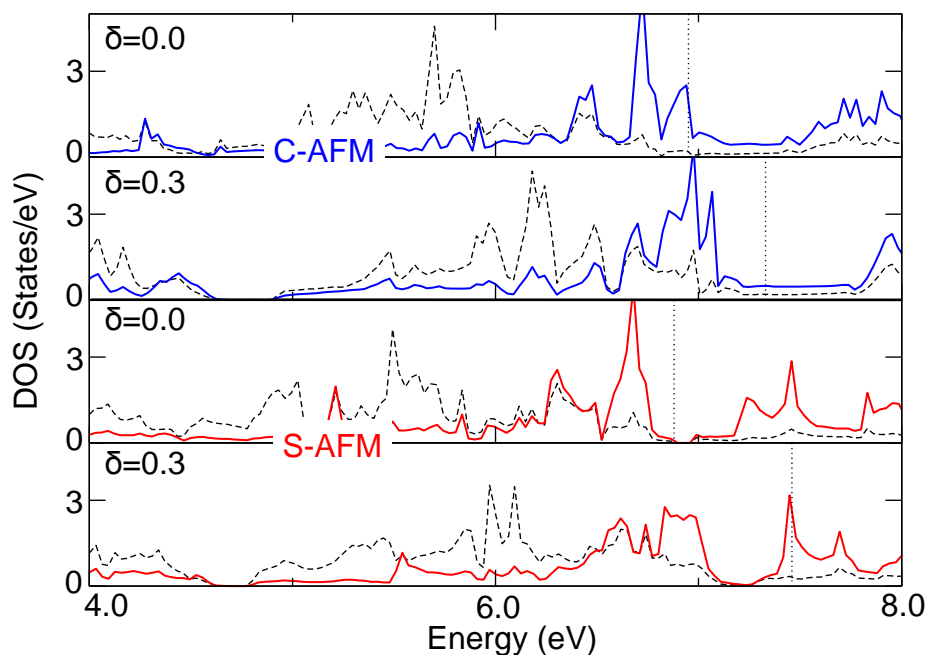


Figure 7.3: Projected densities of states of Fe calculated for C-AFM ordering undoped and 30%-doped LaOFeAs; for S-AFM ordering undoped and 30%-doped LaOFeAs. Dashed line represents for majority channel and solid line for minority channel. The Fermi energy is shown by the vertical dotted line.

(Figure 7.4a), the existence of a small C-AFM region sandwiched NM and S-AFM around  $d_{\text{Fe-As}} \sim d_0$  is consistent to our previous phase diagram. In Figure 7.1, the boundary separating NM and C-AFM states meets the boundary separating C-AFM and S-AFM states for an electron doping of  $\delta \simeq 24\%$  and  $d_{\text{Fe-As}} \simeq 0.98d_0$  in a tricritical point (TCP) where NM, S-AFM, and C-AFM states coexist. The coexistence of different magnetic phase at the TCP suggests that spin fluctuations there may be stronger and more interesting.

This C-AFM region represents an area where spin fluctuations are expected to be large. As shown in Figure 7.4b, for LaOFeAs with  $d_{\text{Fe-As}} = d_0$  at 0.3 electron doping, changing  $a$  shows very similar behavior as  $d_{\text{Fe-As}}$ . It should be noticed that, ground state is extremely sensitive to lattice parameters  $a$  and  $d_{\text{Fe-As}}$ . Only very small difference in structure parameters,  $\sim 1\%$ , might give rise to magnetic phase transition. Such small change can be achieved in experiments by applying external [110] and chemical pressure [137]. For example, chemical pressure in LaOFeAs by substituting La by Sm will shrink  $a$  about 2.3%. About  $\sim 1\%$  change in  $a$  is induced by applying 4GPa external pressure.

## 7.4 Conclusion

In conclusion, we propose that the electronic structures and magnetic properties of FeAs-based superconductors such as LaOFeAs, BaFe<sub>2</sub>As<sub>2</sub> and LiFeAs are domi-

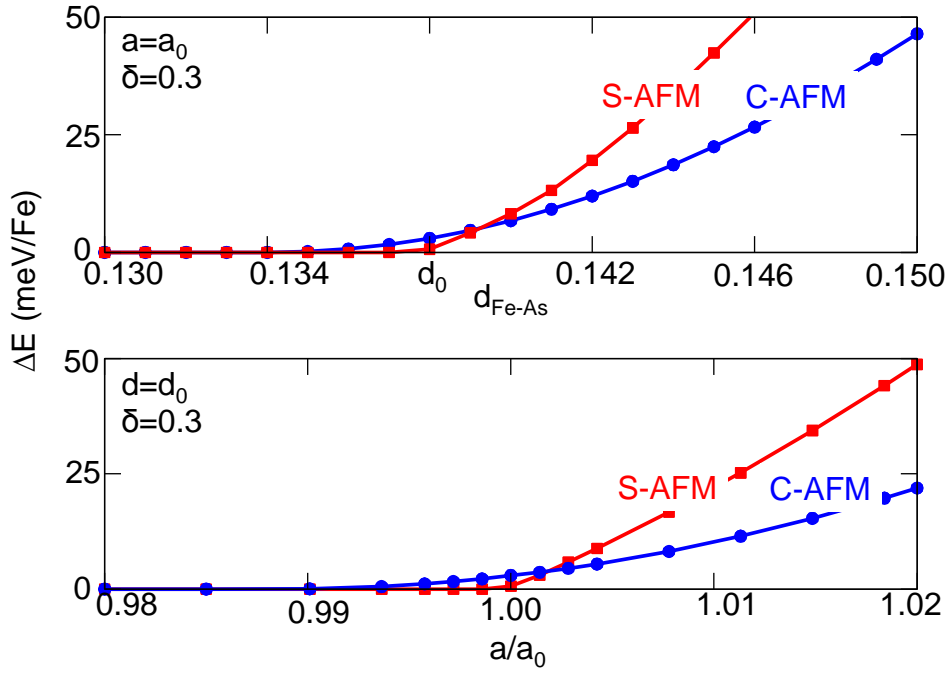


Figure 7.4: (a) The magnetic stabilization energies per Fe atom of C-AFM and S-AFM ordered states relative to NM as a function of  $d_{\text{Fe-As}} = d_0$  for  $a = a_0$  with 30% electron doping. (b) The energies per Fe atom of C-AFM and S-AFM ordered states relative to NM as a function of  $a/a_0$  for  $d_{\text{Fe-As}} = d_0$  with 30% electron doping.

nated by the effective doping and structural details of the FeAs layers. In a QCP scenario, the superconductivity is related to spin fluctuations making it important to understand the magnetic phase diagram as a function of experimentally accessible parameters. The obtained phase diagram implies that the different phases may coexist in a doped LaOFeAs



## Chapter 8

# Understanding the spin Seebeck effect

The ordinary Seebeck effect refers to the generation of an electric voltage  $\Delta V$  by placing a non-magnetic metal in a temperature gradient  $\Delta T$ , as shown in Figure 8.1(a). The induced thermoelectric voltage can be expressed as  $\Delta V = Q\Delta T$ , where for metals the Seebeck coefficient  $Q = -\frac{\pi^2}{3} \frac{k_B^2 T}{e} \frac{\sigma'}{\sigma}$  depends on the details of the electronic structure by way of the conductivity  $\sigma$  and its energy derivative  $\sigma'$ . Extending the Seebeck effect to spins, Uchida *et. al.* applied a temperature gradient to  $\text{Fe}_{19}\text{Ni}_{81}$ , a ferromagnetic (FM) alloy [3]. Naively, they thought that two spin channels would introduce different thermoelectric voltages and consequently a spin voltage would be generated,  $\Delta V_{\uparrow} - \Delta V_{\downarrow} = (Q_{\uparrow} - Q_{\downarrow})\Delta T$ , as shown in Figure 8.1(b). They indeed observed a long-range (millimeter), pure spin voltage at room temperature, which has attracted widespread attention and generated considerable experimental and theoretical discussion. In subsequent studies, this thermally induced spin voltage has been observed in various FM materials such as insulators [140], semiconductors [141] and metals [142]. Its magnitude ranges from  $1\text{nV}$  to  $1\mu\text{V}$ .

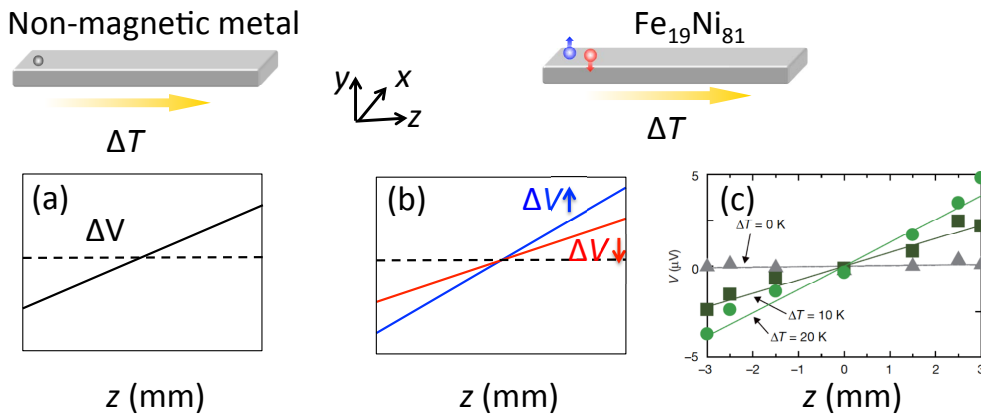


Figure 8.1: Schematic figures of the (a) ordinary Seebeck effect and (b) spin Seebeck effect; (c) experimental signals related to spin voltages, taken from Ref [3].



At the present stage, most researchers in this field believe that the thermal generation of spin voltage is not an artefact, but real; however, no one has come up with a clear understanding of its physical origin. Contrary to the initial suggestion of Uchida *et. al.*, the spin voltage can not be regarded as the result of a simple extension of the Seebeck effect to spins, for the following two reasons.

- If we simply extend the Seebeck effect to spins, the spin voltage will be expressed in terms of a spin accumulation  $\mu_s - \mu_{-s}$  according to the well-established Valet-Fert equation [143]

$$\nabla^2(\mu_s - \mu_{-s}) = \frac{\mu_s - \mu_{-s}}{l_{sf}^2} \quad (8.1)$$

where  $\mu_s$  is the chemical potential;  $l_{sf}$  denotes spin flip diffusion length, which is determined by spin flip scattering. A typical solution of the Valet-Fert equation is  $\mu_s - \mu_{-s} \propto e^{-z/l_{sf}}$ , where the spin accumulation will be suppressed by spin flip scattering and vanish on a length scale of  $l_{sf}$ . For the case of spin injection shown in Figure 8.2, when spin polarized electrons go from a ferromagnetic into a nonmagnetic (NM) metal, there is a spin accumulation around an FM|NM interface. This accumulation only exists in the interface region of length scale of  $l_{sf}$  and vanishes in bulk regions.  $l_{sf}$  is less than 10 nanometer in permalloy and any spin accumulation should vanish on this length scale. How can a thermally induced spin voltage persist up to 1 millimeter?

- In the ordinary Seebeck effect, the generation of a thermoelectric voltage is mediated by free carriers so a thermoelectric voltage can only exist in a conducting material such as a metal or semiconductor. Therefore, the thermally induced spin voltage observed in a ferromagnetic insulator [140] can not be understood from this viewpoint

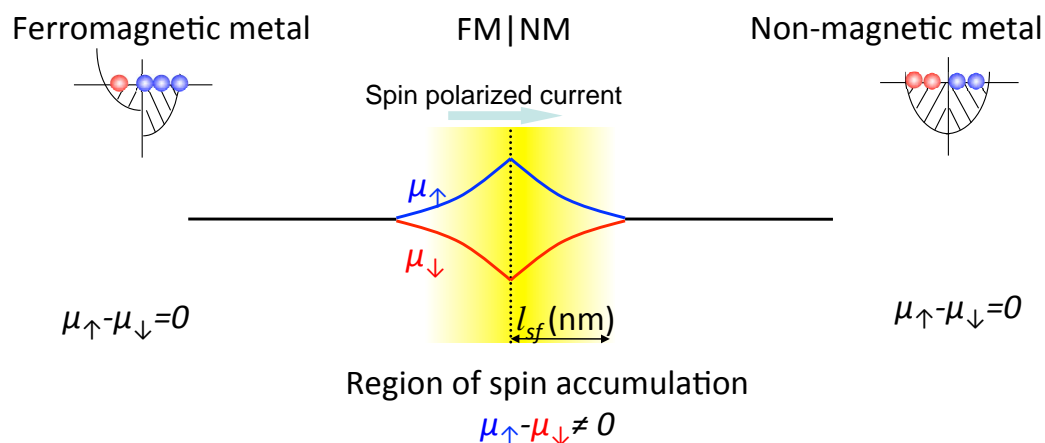


Figure 8.2: Schematic figures of a spin accumulation at an FM|NM interface, when a spin polarized current is injected from the FM into NM

To understand the thermally induced spin voltage, we need to examine other mechanisms besides those leading to “conventional” spin accumulation. In this chapter, we first analyze the definition of a spin voltage. Using a thermodynamic and statistical method, we find that a magnetization potential  $H_s^*$ , which has so far been neglected, will contribute to the spin voltage. The magnetization potential is associated with the thermally induced magnetization gradient and can be expressed in terms of entropy production. We derive the magnetization potentials for two model systems: a two-state system and a free electron gas system. Our results naturally explain why the spin voltage of a ferromagnetic metal is much smaller than that of a ferromagnetic insulator. In addition, we generalize the Valet-Fert equation and show that whereas spin flip scattering suppresses spin accumulation, it mediates the thermal generation of a spin voltage.

## 8.1 Spin Voltage

Spin voltage is the key physical quantity in spintronics. By analogy with charge voltage in electronics, a spin voltage describes an ability to drive the motion of a spin; a gradient of a spin voltage will drive a spin current. In this sense, spin voltage can be defined as  $\mu_s^* - \mu_{-s}^*$ , where  $\mu_s^*$  and  $\mu_{-s}^*$  denote spin related potentials. Here, we identify the spin potential  $\mu_s^*$  as a magneto-electro-chemical potential consisting of three terms: a spin chemical potential  $\mu_s$ , an electric potential  $V$ , and a magnetization potential  $H_s^*$  ( $\mu_B$  is the Bohr magneton) [144],

$$\mu_s^* = \mu_s - eV - \mu_B H_s^* \quad (8.2)$$

The spin chemical potential  $\mu_s$  is (roughly) defined as how much free energy is required to add (or remove) a spin to a system. The chemical potential difference between two spin channels,  $\mu_s - \mu_{-s}$ , accounts for spin accumulation and is widely considered as the key source of spin voltage. For a system with a spin accumulation, the spin with the higher chemical potential will flow (or convert) into the spin channel with the lower chemical potential by spin flip scattering. Therefore, any spin accumulation should vanish on the scale of the spin flip diffusion length  $l_{sf}$ .

The second term, the electric potential  $V$ , is spin independent. It therefore does not directly contribute to a spin voltage. However, it can generate a spin accumulation at an FM|NM interface by driving a spin polarized current as shown in the Valet-Fert analysis [143] and in Figure 8.2. In the published literature, a spin voltage is widely denoted  $\bar{\mu}_s - \bar{\mu}_{-s}$ , where  $\bar{\mu}_s$  is the electro-chemical potential defined as  $\bar{\mu}_s = \mu_s - eV$ . In this definition, a spin voltage only relies on spin accumulation which only exists on a (short) length scale of  $l_{sf}$ .

The third term represents a magnetic contribution to a spin voltage, which has up till now been largely neglected. We will argue that a direct thermodynamic contribution from magnetism (spin distribution) plays a unique role in generating a long range spin voltage. Compared to a typical electrostatic energy  $1eV$  and a thermal energy  $k_B T \sim 0.03eV$  at room temperature, a magnetic energy such as a Zeeman energy

$\mu_B H \sim 5 \times 10^{-5} eV$  is very small even with a large applied magnetic field,  $H = 1T$ . The magnetic energy has consequently been ignored in previous studies [3, 143]. However, in the experiments where a spin Seebeck effect was observed, the magnetic contribution to the spin voltage becomes important for two reasons: (1) there is no electric field involved in the generation of a spin voltage in the open circuit configuration used; (2) for a ferromagnetic material with spontaneous magnetization  $M$ , the magnetic energy mainly comprises exchange energy, which is comparable to thermal energy.

## 8.2 Definition of magnetization potential $H_s^*$

We focus on a ferromagnetic (FM) metal placed in a temperature gradient  $\Delta T$ . The spontaneous magnetization  $M(T)$  of the ferromagnetic metal is a function of the temperature: it decreases with increasing temperature, and vanishes above a certain critical temperature, the Curie temperature  $T_c$ . Since the temperature of the metal is not uniform, we could imagine a nonuniform magnetization  $M(T(r))$ . Intuitively, a nonuniform magnetization will lead to diffusive spin (magnetization) flow from higher magnetization region to lower magnetization region. In order to identify this kind of effective driving force on the spin freedom, we are going to introduce the magnetization potential  $H_s^*$  expressed in terms of the entropy  $S$  produced by a spin (magnetization) current. We note that the magnetization potential  $H_s^*$  arises from nonequilibrium thermodynamics and its gradient  $\nabla H_s^*$  is a thermodynamic force.

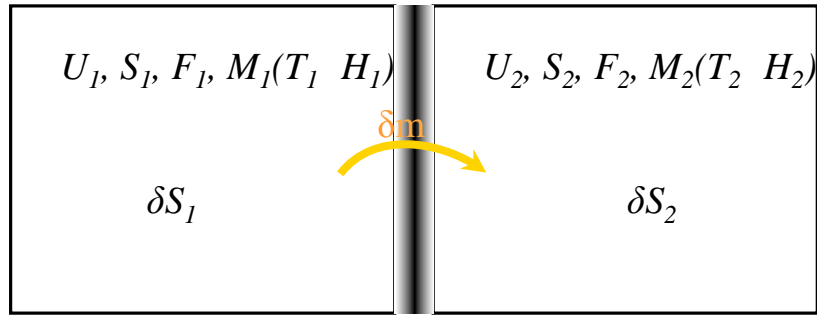
### 8.2.1 Thermodynamic Force

In general, the definition of a thermodynamic force is based on well-established techniques of nonequilibrium thermodynamics [145]. We first consider a composite system composed of two subsystems, and assume the two subsystems are individually in internal equilibrium initially. We focus on an “extensive” parameter such as the magnetization  $M$  with values  $X_1$  and  $X_2$  in the two subsystems. When an infinitesimal amount  $\delta X$  (such as  $\delta m$ ) flows from subsystem 2 ( $X_2 - \delta X$ ) to subsystem 1 ( $X_1 + \delta X$ ), it produces a nonzero total entropy  $\delta S_1 + \delta S_2$ ; the system is not in equilibrium. We can define a thermodynamic (or generalized) force  $\Delta F$  as follows,

$$\Delta F = \frac{\delta(S_1 + S_2)}{\delta X}$$

that drives an irreversible process taking the system toward the equilibrium state.

More specific, as shown in Figure 8.3 we will consider the two subsystems in local equilibrium with  $F, U, S, M(T; H)$ , where  $F$  denotes free energy,  $U$  denotes internal energy,  $S$  denotes entropy,  $M$  denotes magnetization,  $T$  is temperature and  $H$  is magnetic field. When these two inequivalent subsystems start to interact with each other, an instantaneous flow of magnetization  $\delta m$  occurs irreversibly between the two subsystems, producing entropy. (Although the entire system is not in thermodynamic equilibrium, we accept the approximation of “local equilibrium”, which



$$\delta S_1 + \delta S_2 \neq 0 \text{ (nonequilibrium)}$$

Figure 8.3: Two subsystems that are in thermodynamic equilibrium with internal energy  $U$ , entropy  $S$ , free energy  $F$  and magnetization  $M$  as functions of temperature  $T$  and magnetic field  $H$ . Contacting these two subsystems will drive a magnetization flow  $\delta m$  resulting entropy variation  $\delta S$  to two subsystems respectively. (If we only consider magnetic part)

means that thermodynamic quantities such as temperature, magnetization and entropy remain well-defined locally). For instance, consider a flow of magnetization  $\delta m$  from subsystem 1 to 2. The entropy production of subsystem 1,  $\delta S_1$ , is due to a magnetization variation of  $-\delta m$ ; the entropy production of subsystem 2,  $\delta S_2$ , is due to a magnetization variation of  $\delta m$ . The total entropy production caused by this irreversible internal magnetization  $\delta m$  flow is  $\delta S_1 + \delta S_2$ . Here, we can define

$$(1/T) \times \Delta H^* = \frac{\delta S_1 + \delta S_2}{\delta m}$$

More generally, we can define a magnetization potential

$$H^* = T \times \left( \frac{\delta S}{\delta m} \right)_T \quad (8.3)$$

The gradient of  $H^*$  ( $\Delta H^*$  in the discrete case,  $\nabla H^*$  in a continuum case) is a thermodynamic force driving a magnetization (or spin) flow  $\delta m$  between two subsystems. Now, our task is to calculate  $\frac{\delta S}{\delta m}$  and obtain some concrete information about the magnetization potential  $H^*$ . We note that  $H_{\pm s}^*$  in (8.2) is  $H_s^* = -H_{-s}^* = 1/2H^*$ .

## 8.2.2 Difficulties

We encounter two basic difficulties when we set out to calculate  $\frac{\delta S}{\delta m}$ .

- How does one define the entropy of a non-equilibrium system? In principle, the entropy  $S$  is well defined for an equilibrium system with magnetization  $M$ . However, an instantaneous variation of magnetization  $\delta m$  will result in a non-equilibrium system. The definition of the entropy of a non-equilibrium system should be carefully studied. We start with the original statistical definition of

entropy (a definition based on particle distributions) and try to map the entropy of the nonequilibrium case onto an equilibrium case.

- How does one obtain the entropy of a ferromagnetic (FM) material. Since a FM system is essentially a many-body interacting system, to calculate its entropy is a difficult task even for the equilibrium case. Here, we try to map it onto a paramagnetic system with an effective external magnetic field  $H$ . In principle, if we assume that  $H$  is a function of the spontaneous magnetization  $M$ , the mapping can be regarded as a simple mean field approximation, capturing the nature of spontaneous magnetization of FM.

### 8.3 Two-state model system

First, we neglect the interaction between magnetic moments for a paramagnetic material. Thus, in the absence of an external magnetic field, the magnetic associated energy  $E$  is equal to zero, and all magnetic moments are randomly oriented in favor of maximizing entropy, which gives rise to zero magnetization. When this paramagnetic material is subjected to an external magnetic field  $H$ , the energy of quantum magnetic moments is  $E_j = -g_j m_j \mu_B H$ ,  $m_j = -j, (-j+1), \dots, j$ . Here we only take the spin magnetic moment into consideration, since orbital magnetic moments are quenched by a crystal field. For instance, when a magnetic moment with spin  $j = 1/2$  are aligned parallel or antiparallel with respect to  $H$ , the magnetic energy is  $E = -\mu_B H$  and  $E = +\mu_B H$  respectively, where  $\mu_B$  is the Bohr magneton.

Now we consider how such a paramagnetic system reaches equilibrium at constant temperature  $T$  and in the presence of an applied external magnetic field  $H$ . Using statistical thermodynamics, we are going to calculate physical quantities such as the free energy  $F$ , entropy  $S$ , magnetization  $m = M/N$ , ( $M$  is the total magnetization,  $N$  is the number of particles), as functions of  $T$  and  $H$ . The entire system only contains two possible magnetic energy states  $E = \mp \mu_B H$ , ignoring other contributions such as the kinetic energy of particles.

#### 8.3.1 Entropy

The partition function  $Z$  is defined as:

$$\begin{aligned} Z &= \sum \exp\left(-\frac{E}{k_B T}\right) \\ &= \exp\left(\frac{\mu_B H}{k_B T}\right) + \exp\left(-\frac{\mu_B H}{k_B T}\right) \\ \frac{\mu_B H}{k_B T} &= \eta \end{aligned}$$

where  $\sum$  sums up all the possible states ( $E = \mp \mu_B H$ ). The distribution function is

$$f = \exp(\mp \eta) / Z$$

$N_+$  is the number of parallel magnetic moments;  $N_-$  is the number of antiparallel magnetic moments;  $N$  is the total number of all magnetic moments,  $N_+ + N_-$ .

$$\begin{aligned} N_+ &= N \times \exp(\eta)/Z \\ N_- &= N \times \exp(-\eta)/Z \end{aligned}$$

Then the magnetization  $m = M/N$  ( $M$  is the total magnetization) is

$$m = \mu_B \frac{\exp(\eta) - \exp(-\eta)}{\exp(\eta) + \exp(-\eta)}$$

Since entropy is the key quantity in this paper, we are going to calculate the entropy  $S$  in two different ways to avoid any misunderstanding.

*Method (1):* The free energy  $F$  is

$$\begin{aligned} F/N &= -k_B T \ln[Z] \\ &= k_B T \ln[\exp(\eta) + \exp(-\eta)] \end{aligned}$$

We use the thermodynamic definition of entropy:

$$\begin{aligned} S/N &= -\frac{\partial(F/N)}{\partial T} \\ &= k_B \ln[\exp(\eta) + \exp(-\eta)] + k_B T \frac{\frac{\partial \eta}{\partial T} \exp(\eta) - \frac{\partial \eta}{\partial T} \exp(-\eta)}{\exp(\eta) + \exp(-\eta)} \\ &= k_B \ln[\exp(\eta) + \exp(-\eta)] - k_B T \frac{H}{k_B T^2} m \\ &= k_B \ln[\exp(\eta) + \exp(-\eta)] - \frac{H}{T} m \end{aligned} \quad (8.4)$$

*Method (2):* We start with a statistical definition of entropy  $S$ , which should also be valid even for the nonequilibrium case.

$$\begin{aligned} S &= k_B \ln \Omega \\ \Omega &= \frac{N!}{N_+! N_-!} \\ \ln \Omega &= \ln N! - \ln N_+! - \ln N_-! \\ &= N \ln N - N - N_+ \ln N_+ - N_+ - N_- \ln N_- - N_- \\ &= N \ln N - N_+ \ln N_+ - N_- \ln N_- \\ &= N \ln N - \{N * \exp(\eta)/Z\} \ln\{N * \exp(\eta)/Z\} \\ &\quad - \{N * \exp(-\eta)/Z\} \ln\{N * \exp(-\eta)/Z\} \\ &= N \ln N - \{N * \exp(\eta)/Z\} \ln N - \{N * \exp(\eta)/Z\} \ln\{\exp(\eta)/Z\} \\ &\quad - \{N * \exp(-\eta)/Z\} \ln N - \{N * \exp(-\eta)/Z\} \ln\{\exp(-\eta)/Z\} \\ &= N * \ln Z - N * \exp(\eta) * \eta/Z + N * \exp(-\eta) * \eta/Z \end{aligned}$$

$$\begin{aligned}
S/N &= k_B \ln\{\exp(\eta) + \exp(-\eta)\} - k_B \frac{\mu_B H}{k_B T} \frac{\exp(\eta) - \exp(-\eta)}{\exp(\eta) + \exp(-\eta)} \\
&= k_B \ln\{\exp(\eta) + \exp(-\eta)\} - \frac{H}{T} m
\end{aligned} \tag{8.5}$$

If  $N_+ = N$  and  $N_- = 0$ , the entropy is minimized,  $S = 0$ ; if  $N_+ = N_- = \frac{1}{2}N$ , the entropy is maximized  $S = Nk_B \ln 2$ . Clearly, the two different methods give consistent results, (8.4) and (8.5).

Using the second (statistical) method, we are going to determine how the entropy change depends on a magnetization variation  $\delta m = \mu_B(\delta N_+ - \delta N_-)/N$ . For simplicity, we assume the total number of magnetic moments  $N$  is unchanged and  $\delta N_+ = -\delta N_- \ll N_+, N_-$ ,

$$\delta N_+/N = -\delta N_-/N = 1/2\delta m$$

$$\begin{aligned}
N_+ &= N * \exp(\eta)/Z + \delta N_+ \\
N_- &= N * \exp(-\eta)/Z + \delta N_-
\end{aligned}$$

$$\begin{aligned}
\ln \Omega &= N \ln N - \{N * \exp(\eta)/Z + \delta N_+\} \ln\{N * \exp(\eta)/Z + \delta N_+\} \\
&\quad - \{N * \exp(-\eta)/Z + \delta N_-\} \ln\{N * \exp(-\eta)/Z + \delta N_-\}
\end{aligned}$$

$$\begin{aligned}
\delta S/k_B &= -\frac{1}{N} \delta N \ln\{N * \exp(\eta)/Z + \delta N_+\} + \frac{1}{N} \delta N \ln\{N * \exp(-\eta)/Z + \delta N_-\} \\
&\quad - \exp(\eta)/Z \ln\{1 + \delta N_+/(N * \exp(\eta)/Z)\} \\
&\quad - \exp(-\eta)/Z \ln\{1 + \delta N_-/(N * \exp(-\eta)/Z)\} \\
&= -\eta(\delta N_+ - \delta N_-)/N \\
&= -\eta \delta m
\end{aligned}$$

Now, we have determined how the the entropy variation  $\delta S$  depends on a magnetization variation  $\delta m$  for the two-state model system,

$$\delta S = -\frac{H}{T} \delta m \tag{8.6}$$

### 8.3.2 Special cases

According to (8.3) and (8.6), the magnetization potential we obtain is  $H^* = -H$ . We will analyze some special cases in order to get a clearer physical picture of why its gradient  $\Delta H^*$  can drive a magnetization flow  $\delta m$  in the system shown in Figure 8.3.

- For a uniform system ( $H_1 = H_2 = H; T_1 = T_2$ ),  $\Delta H^* = 0$ ,  $\delta S = 0 * \delta m$ , there is no magnetization  $\delta m$  flow. Since the entire system is uniform and in equilibrium, we should not expect any flow.

- For a system with a non-uniform temperature ( $H_1 = H_2; T_1 < T_2$ ),  $\Delta H^* = 0$ ,  $\delta S = (\frac{1}{T_2} - \frac{1}{T_1})(-H\delta m)$ , a magnetization current  $\delta m$  will flow from subsystem 1 to 2. The magnetization  $m$  is roughly proportional to  $\frac{H}{T}$ , thus for a uniform magnetic field a low temperature implies high magnetization. So we can explain the existence of a magnetization flow in terms of magnetization diffusion from a high magnetization region to a low magnetization region, despite the magnetic energies  $-H\delta m$  in both regions being equal. Associated with the magnetization flow  $\delta m$ , an energy current  $-H\delta m$  will also flow from subsystem 1 with low temperature to subsystem 2 with high temperature. However  $-H\delta m$  is a negative value, thus heat current will flow from high temperature to low temperature. In summary, the entropy production in this case originates from the heat flow in a non-uniform temperature system.
- For a system with a non-uniform magnetic field ( $H_1 > H_2; T_1 = T_2$ ),  $\Delta H^* = -H_1 + H_2$ ,  $\delta S = \frac{1}{T}(H_1 - H_2)\delta m$  and a magnetization current  $\delta m$  will flow from subsystem 1 to 2. The magnetization  $\langle m \rangle$  in subsystem 1 is larger than in subsystem 2, thus it is natural to accept that the magnetization current flow from 1 to 2.

In summary, for a two-state model system, the magnetization potential is

$$\begin{aligned} H^* &= T \times \left( \frac{\delta S}{\delta m} \right)_T \\ &= -H \end{aligned} \quad (8.7)$$

$H^*$  has the opposite sign to the magnetic field  $H$ .  $\nabla H^*$  can be viewed as a generalized thermodynamic force, which drives a magnetization current.

## 8.4 Free electron gas model system

### 8.4.1 Equilibrium

First of all, we will discuss the free electron gas in the absence of an applied magnetic field  $H$ . We note that some basic notations and assumptions used in this section are taken from a standard textbook [146]. The detailed derivation of this section is shown in the Appendix A. The energy and distribution function is

$$\begin{aligned} \varepsilon(k) &= \frac{\hbar^2 k^2}{2m} \\ f(\varepsilon) &= \frac{1}{\exp(\varepsilon - \mu)/k_B T + 1} \end{aligned} \quad (8.8)$$

The density of states  $g(\varepsilon)$  is

$$\begin{aligned} g(\varepsilon) &= \frac{3}{2} \frac{n}{(\varepsilon_F)^{3/2}} \varepsilon^{1/2} \quad \varepsilon > 0 \\ &= 0 \quad \varepsilon < 0 \end{aligned}$$



The electron density  $n$  and internal energy  $u$  are

$$\begin{aligned} n &= \int_{-\infty}^{\infty} g(\epsilon) f(\epsilon) d\epsilon \\ u &= \int_{-\infty}^{\infty} g(\epsilon) \epsilon f(\epsilon) d\epsilon \end{aligned}$$

Now we are going to calculate the entropy  $S$  in two different ways to avoid any misunderstanding.

*Method (1):* if we use the Sommerfeld expansion for the distribution function  $f$ , the chemical potential  $\mu$  is

$$\mu = \epsilon_F \left( 1 - \frac{1}{3} \left( \frac{\pi k_B T}{2\epsilon_F} \right)^2 \right) \quad (8.9)$$

The internal energy  $u$  is

$$u = \frac{3}{5} n \epsilon_F \left( 1 - \frac{1}{3} \left( \frac{\pi k_B T}{2\epsilon_F} \right)^2 \right)^{5/2} + \frac{3\pi^2}{8} n \frac{(k_B T)^2}{\epsilon_F} \left( 1 - \frac{1}{3} \left( \frac{\pi k_B T}{2\epsilon_F} \right)^2 \right)^{1/2}$$

Varying the temperature by  $\delta T$  would give rise to a variation of energy  $\delta u$ :

$$\delta u = \frac{\pi^2 k_B T}{2 \epsilon_F} n k_B \delta T$$

We use a thermodynamic definition of entropy  $T \delta S = \delta u$  and find

$$S = \frac{\pi^2 k_B T}{2 \epsilon_F} n k_B \quad (8.10)$$

*Method (2):* we next confirm the entropy by using a statistical definition, which is also valid for the nonequilibrium case

$$S = -k_B \sum f_i \ln f_i + (1 - f_i) \ln(1 - f_i) \quad (8.11)$$

where  $\sum$  sums up all the possible states  $i$

$$\begin{aligned} S/k_B &= \sum \ln[1 + \exp(\mu - \epsilon)/k_B T] - \sum \frac{(\mu - \epsilon)/k_B T}{1 + \exp(\epsilon - \mu)/k_B T} \\ &= \frac{1}{k_B T} \frac{n}{\epsilon_F^{3/2}} \mu^{5/2} + \frac{5}{3} \frac{1}{k_B T} \frac{\pi^2}{6} (k_B T)^2 \frac{9}{4} \frac{n}{\epsilon_F^{3/2}} \mu^{1/2} - \frac{n\mu}{k_B T} \end{aligned}$$

Considering (8.9), we obtain

$$S/k_B = \frac{\pi^2 k_B T}{2 \epsilon_F} n \quad (8.12)$$

Clearly, two different methods give consistent results, (8.10) and (8.12), for the free electron gas in the absence of an applied magnetic field.

Now, we model a ferromagnet as a paramagnetic material in an extend magnetic field,  $H$ . The energy of entire system contains a magnetic energy  $\mp\mu_B H$  in addition to the kinetic energy  $p^2/2m$ . In principle, our system is a Pauli-paramagnetic system. The densities of spins parallel ( $n_+$ ) and antiparallel ( $n_-$ ) to the magnetic field are

$$n_{\pm} = \int_{-\infty}^{\infty} g(\epsilon) f_{\pm}(\epsilon) d\epsilon$$

$$f_{\pm}(\epsilon) = \frac{1}{\exp(\epsilon - \mu \mp \mu_B H)/k_B T + 1} \quad (8.13)$$

$$n_+ = \frac{3}{2} \frac{n}{\epsilon_F^{3/2}} \frac{1}{2} \frac{2}{3} (\mu + \mu_B H)^{3/2} + \frac{\pi^2}{6} (k_B T)^2 \frac{3}{2} \frac{n}{\epsilon_F^{3/2}} \frac{1}{4} (\mu + \mu_B H)^{-1/2}$$

$$n_- = \frac{3}{2} \frac{n}{\epsilon_F^{3/2}} \frac{1}{2} \frac{2}{3} (\mu - \mu_B H)^{3/2} + \frac{\pi^2}{6} (k_B T)^2 \frac{3}{2} \frac{n}{\epsilon_F^{3/2}} \frac{1}{4} (\mu - \mu_B H)^{-1/2}$$

We express the magnetization  $m$  as a function of  $H$  and  $T$ :

$$m/\mu_B = (n_+ - n_-)/n \quad (8.14)$$

$$= \frac{3}{2} \frac{1}{\epsilon_F^{3/2}} \frac{1}{2} \frac{2}{3} (\mu + \mu_B H)^{3/2} + \frac{\pi^2}{6} (k_B T)^2 \frac{3}{2} \frac{1}{\epsilon_F^{3/2}} \frac{1}{4} (\mu + \mu_B H)^{-1/2}$$

$$- \frac{3}{2} \frac{1}{\epsilon_F^{3/2}} \frac{1}{2} \frac{2}{3} (\mu - \mu_B H)^{3/2} - \frac{\pi^2}{6} (k_B T)^2 \frac{3}{2} \frac{1}{\epsilon_F^{3/2}} \frac{1}{4} (\mu - \mu_B H)^{-1/2}$$

$$= 3/2 \frac{\mu_B H}{\epsilon_F} - \frac{\pi^2}{16} \left( \frac{k_B T}{\epsilon_F} \right)^2 \frac{\mu_B H}{\epsilon_F} \quad (8.15)$$

In principle, we can calculate the entropy  $S$  by using the statistical definition (8.11). However, the calculation of  $S$  is tedious (We will come up with the exact expression in our future work). Using the Maxwell relations of thermodynamics as well as the expression for  $m(H, T)$  (8.15), we can give a simple expression for  $\left( \frac{\partial S}{\partial m} \right)_T$  of great interests

$$\left( \frac{\partial S}{\partial m} \right)_T = \left( \frac{\partial S}{\partial H} \right)_T \left( \frac{\partial H}{\partial m} \right)_T$$

$$= \left( \frac{\partial m}{\partial T} \right)_H \left( \frac{\partial H}{\partial m} \right)_T$$

$$= - \frac{\frac{\pi^2}{12} \left( \frac{k_B T}{\epsilon_F} \right)^2 H}{1 - \frac{\pi^2}{24} \left( \frac{k_B T}{\epsilon_F} \right)^2 T} \quad (8.16)$$

This result will be used in the discussion below.

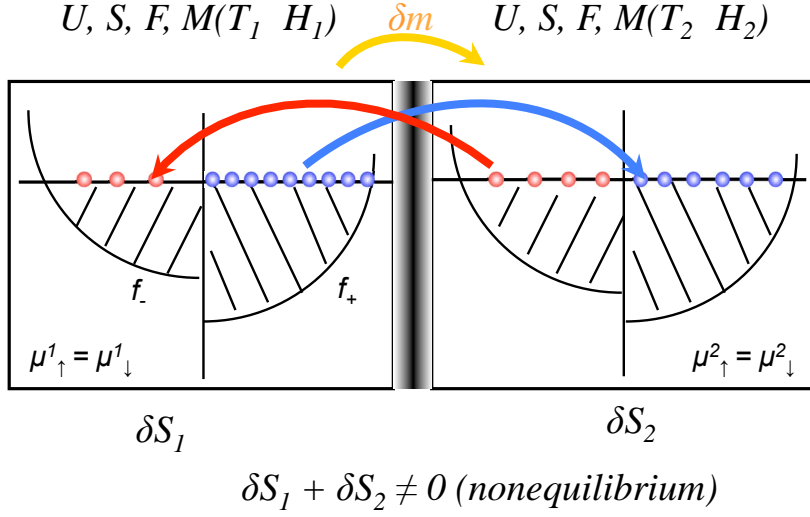


Figure 8.4: We map a ferromagnetic metal onto a paramagnetic free electron gas system with an effective external magnetic field  $H$ . Two paramagnetic free electron gas subsystems ( $T_1 < T_2$ ) are in thermodynamic equilibrium with the spin distribution  $f_{\pm}$  (8.8). Bringing these two subsystems into contact will drive a magnetization flow  $\delta m$  resulting in a nonequilibrium distribution  $\tilde{f}_{\pm}$  and entropy variation  $\delta S$  to two subsystems. (If we only consider the magnetic part)

### 8.4.2 Nonequilibrium

We proceed to discuss the entropy for the nonequilibrium case

$$S = -k_B \sum \tilde{f}_i \ln \tilde{f}_i + (1 - \tilde{f}_i) \ln(1 - \tilde{f}_i)$$

$\tilde{f}_i$  represents the nonequilibrium distribution, in contrast to the equilibrium distribution  $f_{\pm}$  (8.8). In principle, we could calculate the entropy  $S$  exactly, if we knew the  $\tilde{f}_{\pm}(H, T, \delta m)$ , and then discuss the entropy  $\delta S$  induced by a magnetization variation  $\delta m$ . However, we do not know the exact effect of  $\delta m$  on the  $\delta \tilde{f}_i$ . We make an approximation: the electron collision time  $\tau_e$  is extremely small compared to a spin-flip scattering time  $\tau_{sf}$ , and any magnetic (or spin) moments  $\delta m$  which flow from one system to another will immediately reach its individual spin channel's equilibrium, as suggested in Figure 8.4. Even though the whole system is not in equilibrium, we will assume that each spin channel is in its individual equilibrium  $f_+(T, H, n_+ + \delta m/2)$ ,  $f_-(T, H, n_- - \delta m/2)$  (8.13),

$$\begin{aligned} \tilde{f}_+(T, H, \delta m/2) &= f_+(T, H, n_+ + \delta m/2) \\ \tilde{f}_-(T, H, \delta m/2) &= f_-(T, H, n_+ - \delta m/2) \end{aligned} \quad (8.17)$$

Based on this approximation, we can map this nonequilibrium system into an equilibrium system and reduce the magnetization potential  $H^*$  (8.3) to

$$H^* = T \times \left( \frac{\delta S}{\delta m} \right)_T = T \times \left( \frac{\partial S}{\partial m} \right)_T$$

Considering (8.16), we obtain

$$H^* = -\alpha H \quad \text{with} \quad \alpha = \frac{\frac{\pi^2}{12} \left(\frac{k_B T}{\epsilon_F}\right)^2}{1 - \frac{\pi^2}{24} \left(\frac{k_B T}{\epsilon_F}\right)^2} \quad (8.18)$$

Comparing to  $H^*$  (8.7) for the two-state model,  $\alpha$  is a screening factor due to the high degeneracy of electron gas,  $\frac{k_B T}{\epsilon_F} \sim 0.03$  at room temperature.

## 8.5 Generalized Valet-Fert equation

The original Valet-Fert equation [143] (8.1) for spin accumulation is based on the electro-chemical potential  $\bar{\mu}_s = \mu_s - eV$ . In this section, using the magneto-electro-chemical potential  $\mu_s^* = \mu_s - eV + H_s^*$  with the magnetization potential  $H_s^*$  defined in (8.3), we will generalize the Valet-Fert equation. Before embark upon tedious derivation, we anticipate the following results:

- Since spin flip scattering suppresses spin accumulation, chemical potential difference between two spin channels  $\mu_+ - \mu_-$  which describes local spin accumulation, vanishes for distances  $\gg l_{sf}$ .
- Even though spin flip scattering has little effects on an electrostatic potential  $V$ , the electro-chemical potential difference between two spin channels  $\bar{\mu}_+ - \bar{\mu}_- = (\mu_s - eV) - (\mu_{-s} - eV)$  will also vanish for distances  $\gg l_{sf}$  because of cancellation.
- Similarly, we can imagine that spin flip scattering also has little effects on the magnetization potential, because the definition of  $H_s^*$  is based on a local equilibrium assumption in the absence of any local spin accumulation. A spin current (or magnetization flow) only originates from the nonequilibrium nature of the entire system. Moreover, the magnetization potential  $H_s^*$  is spin dependent, unlike the spin-independent electrostatic potential  $V$ . Thus spin voltage  $\mu_+^* - \mu_-^*$  is determined by  $H_s^*$ .

### 8.5.1 Boltzmann Equation

For a detailed derivation of the Valet-Fert equation for the spin accumulation (8.1), the reader is referred to [143]. Here we just sketch the basic ideas and results. We start with the Boltzmann Equation for the distribution function  $f$

$$\frac{\partial f}{\partial t} + \mathbf{v} \cdot \frac{\partial f}{\partial \mathbf{r}} + \mathbf{F} \cdot \frac{1}{\hbar} \frac{\partial f}{\partial \mathbf{v}} = \left(\frac{\partial f}{\partial t}\right)_{\text{collision}}$$

that be written as the sum of the equilibrium Fermi-Dirac distribution  $f^0(v)$  (8.8) and small perturbations

$$f_s(z, \mathbf{v}) = f_s^0(v) + \frac{\partial f_s^0}{\partial \epsilon} \{[\mu^0 - \mu_s(z)] + g_s(z, \mathbf{v})\}$$

where  $\mu^0 - \mu_s(z)$  is an isotropic term expressing the local variations of the chemical potential, accounting for the spin accumulation and  $g_s(z, \mathbf{v})$  is an anisotropic term. The driving force  $\mathbf{F}$  for motion of electrons is the Coulomb force

$$\mathbf{F} = -e\nabla V$$

### 8.5.2 Differences

For a ferromagnetic metal placed in a temperature gradient, the Boltzmann Equation is still valid. However, two modifications are necessary: (1) the distribution function  $f$  will be expanded to include the effect of the temperature gradient; (2) The driving force  $\mathbf{F}$  must be expanded to include the effect of the magnetization potential  $H^*$

$$f_s(z, \mathbf{v}) = f_s^0(v) + \frac{\partial f_s^0}{\partial \epsilon} \left\{ [\mu^0 - \mu_s(z)] + \frac{\epsilon - \mu^0}{T^0} [T^0 - T(z)] + g_s(z, \mathbf{v}) \right\}$$

Considering that a gradient of  $H^*$  will be an effective spin motive force, we expand the Boltzmann Equation

$$\frac{\partial f}{\partial t} + \mathbf{v} \cdot \frac{\partial f}{\partial \mathbf{r}} + (-e\nabla V - \mu_B \nabla H_s^*) \cdot \frac{1}{\hbar} \frac{\partial f}{\partial \mathbf{v}} = \left( \frac{\partial f}{\partial t} \right)_{collision}$$

For a steady system, the first term on the right side disappear. We consider spin-conserving and spin-flip collisions and obtain

$$\begin{aligned} & v_z \frac{\partial f_s}{\partial z}(z, \mathbf{v}) - eE(z)v_z \frac{\partial f^0}{\partial \epsilon}(z, \mathbf{v}) - \mu_B \nabla H_s^* v_z \frac{\partial f^0}{\partial \epsilon}(z, \mathbf{v}) \\ &= \int d^3 v' \delta[\epsilon(v') - \epsilon(v)] P_s[z, \epsilon(v)] [f_s(z, \mathbf{v}') - f_s(z, \mathbf{v})] \\ &+ \int d^3 v' \delta[\epsilon(v') - \epsilon(v)] P_{sf}[z, \epsilon(v)] [f_{-s}(z, \mathbf{v}') - f_s(z, \mathbf{v})] \end{aligned}$$

Where the  $P_s(z, \epsilon)$  and  $P_{sf}(z, \epsilon)$  are, respectively, spin conserving and spin-flip transition probabilities. They are assumed to be isotropic in velocity space, so that  $P_{sf}(z, \epsilon)$  does not transfer momentum between the two spin channels. After a lengthy derivation (see Appendix B), we obtain a generalized Valet-Fert equation

$$\frac{2\sigma'_{-s}}{\sigma'_s + \sigma'_{-s}} \nabla^2 \mu_s^*(z) - \frac{\sigma_{-s}}{\sigma_s} \frac{2\sigma'_s}{\sigma'_s + \sigma'_{-s}} \nabla^2 \mu_{-s}^*(z) = \frac{\mu_s^*(z) - \mu_{-s}^*(z) - H^*}{l_{sf}^2}$$

where  $\sigma$  is the conductivity and  $\sigma'$  its energy derivative. Comparing the generalized equation with the initial Valet-Fert equation (8.1), we find that: (1) in the absence of a magnetization potential ( $H^* = 0$ ), the temperature gradient will modify the equation by adding some factors but not account for a long-range spin voltage; (2) when a magnetization potential  $H^*$  is included, a spin voltage can be expressed as

$$\mu_s^*(z) - \mu_{-s}^*(z) = -H^*$$

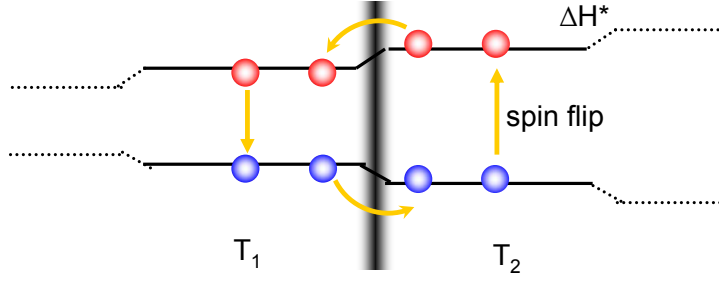


Figure 8.5: Spin flip scattering mediates the thermal generation of a spin voltage

It can be long-range and will not be suppressed by the spin flip scattering. For a ferromagnetic metal, we use (8.18) to make a rough estimate of the magnitude of the spin voltage.

$$\mu_s^*(z) - \mu_{-s}^*(z) \sim \frac{\frac{\pi^2}{24} \left(\frac{k_B T}{\varepsilon_F}\right)^2}{1 - \frac{\pi^2}{24} \left(\frac{k_B T}{\varepsilon_F}\right)^2} \mu_B H$$

$\frac{k_B T}{\varepsilon_F} \sim 0.03$ ,  $\mu_B H \sim k_B T_c$ , thus the estimated thermal spin voltage is small,  $10^{-7} V/K$ .

Inside the sample, the spin voltage is equal to the magnetization potential  $H^*$ . It stems from the magnetization gradient induced by the temperature gradient. Since we accept the local equilibrium approximation, there is no local spin accumulation; a spin current will be driven instead by the magnetization potential  $H^*$ . This irreversible spin current will break the initial local equilibrium spin distribution, and can lead to a spin accumulation quenching the magnetization potential. However, this spin accumulation will be suppressed by spin flip, and consequently the magnetization potential persists, as shown schematically in Figure 8.5.

## 8.6 Summary

In the literature, a spin voltage is widely defined as  $\bar{\mu}_s - \bar{\mu}_{-s}$ , which is associated with spin accumulation. However spin accumulation cannot account for the experimental observations of thermal generation of a long range spin voltage. In this paper, we propose that the magnetic contribution (or spin entropy) plays a key role in generating a long-range spin voltage.

For a FM material in equilibrium, the magnetization can be written as a function of temperature and magnetic field  $M(T, H)$ . Under a temperature gradient, the whole system is in nonequilibrium and an irreversible spin current occurs, even only considering the magnetic part. A well-established result of nonequilibrium thermodynamics is that an irreversible current will increase the total entropy. Therefore, the driving force for the spin current is expressed in terms of entropy production,

$$H^* = T \times \left( \frac{\delta S}{\delta m} \right)_T$$

We studied two model systems and found

$$H^* = -\alpha H$$

where  $H$ , as a function of  $M(T)$ , denotes an effective magnetic field describing the spontaneous magnetization of ferromagnetic materials, and  $\alpha$  denotes a screening factor critically dependent on the thermodynamic and statistical properties of specific materials. Various type of FM materials (such as insulators, semiconductor, and metals) will have very different  $\alpha$ . For a FM metal,  $\alpha$  (8.18) can be so small that the estimated spin voltage is of order  $10^{-7}V$ ; for an insulator,  $\alpha$  such as (8.7) will be much larger. We believe that the  $\alpha$  could explain why the experimentally observed spin voltage ranges from  $1nV$  to  $1\mu V$  depending on materials.

The chemical potential should be generalized to a magneto-electro-chemical potential  $\mu_s^*$

$$\begin{aligned} \mu_s^* &= \mu_s - eV - \mu_B H_s^* \\ \text{with } H_{\pm}^* &= \pm \frac{1}{2} \mu_B H^* \end{aligned}$$

We obtain a generalized Valet-Fert equation in the presence of a temperature gradient as well as a magnetization gradient.

$$\frac{2\sigma'_{-s}}{\sigma'_s + \sigma'_{-s}} \nabla^2 \mu_s^*(z) - \frac{\sigma_{-s}}{\sigma_s} \frac{2\sigma'_s}{\sigma'_s + \sigma'_{-s}} \nabla^2 \mu_{-s}^*(z) = \frac{\mu_s^*(z) - \mu_{-s}^*(z) - H^*}{l_{sf}^2}$$

The spin voltage is

$$\mu_s^*(z) - \mu_{-s}^*(z) = -H^* = \alpha H(M(T))$$

A spin current will return the system back to equilibrium. Without spin flip scattering, the entire system will approach equilibrium where spin voltage vanishes. In this way, spin flip scattering maintains the spin voltage.

# Appendix A

## Free electron gas model system

If we use the Sommerfeld expansion,

$$\begin{aligned} & \int_{-\infty}^{\infty} H(\epsilon) f(\epsilon) d\epsilon \\ = & \int_{-\infty}^{\infty} H(\epsilon) d\epsilon + \frac{\pi^2}{6} (k_B T)^2 H'(\mu) + \frac{7\pi^4}{360} (k_B T)^4 H'''(\mu) + O\left(\frac{k_B T}{\mu}\right)^6 \quad (\text{A.1}) \end{aligned}$$

the relationship between chemical potential  $\mu$  and charge density  $n$ ,

$$\begin{aligned} n &= \int_{-\infty}^{\infty} g(\epsilon) f(\epsilon) d\epsilon \\ &= \int_{-\infty}^{\mu} g(\epsilon) d\epsilon + \frac{\pi^2}{6} (k_B T)^2 g'(\mu) \\ &= \int_{-\infty}^{\epsilon_F} g(\epsilon) d\epsilon + (\mu - \epsilon_F) g(\epsilon_F) + \frac{\pi^2}{6} (k_B T)^2 g'(\mu) \\ &= n + (\mu - \epsilon_F) g(\epsilon_F) + \frac{\pi^2}{6} (k_B T)^2 g'(\epsilon_F) \end{aligned}$$

$$(\mu - \epsilon_F) g(\epsilon_F) + \frac{\pi^2}{6} (k_B T)^2 g'(\epsilon_F) = 0$$

$$\begin{aligned} \mu &= \epsilon_F - \frac{\pi^2}{6} (k_B T)^2 \frac{g'(\epsilon_F)}{g(\epsilon_F)} \\ &= \epsilon_F - \frac{\pi^2}{6} (k_B T)^2 \frac{1}{2\epsilon_F} \\ &= \epsilon_F \left(1 - \frac{1}{3} \left(\frac{\pi k_B T}{2\epsilon_F}\right)^2\right) \quad (\text{A.2}) \end{aligned}$$



The internal energy  $u$  is

$$\begin{aligned}
 u &= \int_{-\infty}^{\mu} H(\varepsilon) d\varepsilon + \frac{\pi^2}{6} (k_B T)^2 H'(\mu) \\
 &= \int_{-\infty}^{\mu} g(\varepsilon) \varepsilon d\varepsilon + \frac{\pi^2}{6} (k_B T)^2 (\mu g'(\mu) + g(\mu)) \\
 &= \int_{-\infty}^{\mu} \frac{3}{2} \frac{n}{\varepsilon_F^{3/2}} \varepsilon^{1/2} \varepsilon d\varepsilon + \frac{\pi^2}{6} (k_B T)^2 \left( \mu \frac{3}{2} \frac{n}{\varepsilon_F^{3/2}} \frac{1}{2} \mu^{-1/2} + \frac{3}{2} \frac{n}{\varepsilon_F^{3/2}} \mu^{1/2} \right) \\
 &= \frac{3}{2} \frac{n}{\varepsilon_F^{3/2}} \frac{2}{5} \mu^{5/2} + \frac{\pi^2}{6} (k_B T)^2 \left( \frac{3}{2} \frac{n}{\varepsilon_F^{3/2}} \frac{1}{2} + \frac{3}{2} \frac{n}{\varepsilon_F^{3/2}} \right) \mu^{1/2}
 \end{aligned}$$

We express  $u$  in terms of temperature,

$$\begin{aligned}
 u &= \frac{3}{2} \frac{n}{\varepsilon_F^{3/2}} \frac{2}{5} \mu^{5/2} + \frac{\pi^2}{6} (k_B T)^2 \left( \frac{3}{2} \frac{n}{\varepsilon_F^{3/2}} \frac{1}{2} + \frac{3}{2} \frac{n}{\varepsilon_F^{3/2}} \right) \mu^{1/2} \\
 &= \frac{3}{2} \frac{n}{\varepsilon_F^{3/2}} \frac{2}{5} (\varepsilon_F (1 - \frac{1}{3} (\frac{\pi k_B T}{2 \varepsilon_F})^2))^{5/2} + \frac{\pi^2}{6} (k_B T)^2 \left( \frac{3}{2} \frac{n}{\varepsilon_F^{3/2}} \frac{1}{2} + \frac{3}{2} \frac{n}{\varepsilon_F^{3/2}} \right) (\varepsilon_F (1 - \frac{1}{3} (\frac{\pi k_B T}{2 \varepsilon_F})^2))^{1/2} \\
 &= \frac{3}{2} \frac{2}{5} n \varepsilon_F (1 - \frac{1}{3} (\frac{\pi k_B T}{2 \varepsilon_F})^2)^{5/2} + \frac{\pi^2}{6} (k_B T)^2 \left( \frac{3}{2} \frac{n}{\varepsilon_F} \frac{1}{2} + \frac{3}{2} \frac{n}{\varepsilon_F} \right) (1 - \frac{1}{3} (\frac{\pi k_B T}{2 \varepsilon_F})^2)^{1/2}
 \end{aligned}$$

Varying temperature  $\delta T$  would give rise to a variation of energy  $\delta u$ :

$$\begin{aligned}
 \delta u &= \frac{3}{2} \frac{2}{5} n \varepsilon_F (1 - \frac{1}{3} (\frac{\pi k_B T}{2 \varepsilon_F})^2)^{3/2} \frac{5}{2} (-\frac{2}{3}) (\frac{\pi k_B}{2 \varepsilon_F})^2 T \delta T \\
 &\quad + \frac{\pi^2}{6} k_B^2 2T \left( \frac{3}{2} \frac{n}{\varepsilon_F} \frac{1}{2} + \frac{3}{2} \frac{n}{\varepsilon_F} \right) (1 - \frac{1}{3} (\frac{\pi k_B T}{2 \varepsilon_F})^2)^{1/2} \delta T \\
 &\quad + \frac{\pi^2}{6} (k_B T)^2 \left( \frac{3}{2} \frac{n}{\varepsilon_F} \frac{1}{2} + \frac{3}{2} \frac{n}{\varepsilon_F} \right) \frac{1}{2} (1 - \frac{1}{3} (\frac{\pi k_B T}{2 \varepsilon_F})^2)^{-1/2} (-\frac{2}{3}) (\frac{\pi k_B}{2 \varepsilon_F})^2 T \delta T \\
 &= \frac{\pi^2 k_B T}{2 \varepsilon_F} n k_B \delta T
 \end{aligned}$$

Using a statistical definition of entropy  $S$ ,

$$S = -k_B \sum_i f_i \ln f_i + (1 - f_i) \ln(1 - f_i)$$

where  $\sum_i$  sums up all possible states  $i$ .

$$\begin{aligned}
S/k_B &= \sum \ln[1 + \exp(\mu - \varepsilon)/k_B T] - \sum \frac{(\mu - \varepsilon)/k_B T}{1 + \exp(\varepsilon - \mu)/k_B T} \\
&= \int_{-\infty}^{\infty} g(\varepsilon) \ln[1 + \exp(\mu - \varepsilon)/k_B T] d\varepsilon - \int_{-\infty}^{\infty} g(\varepsilon) \frac{(\mu - \varepsilon)/k_B T}{\exp(\varepsilon - \mu)/k_B T + 1} d\varepsilon \\
&= \frac{2}{3} \frac{1}{k_B T} \int_{-\infty}^{\infty} g(\varepsilon) \varepsilon \frac{1}{\exp(\varepsilon - \mu)/k_B T + 1} d\varepsilon - \frac{1}{k_B T} \int_{-\infty}^{\infty} g(\varepsilon) (\mu - \varepsilon) \frac{1}{\exp(\varepsilon - \mu)/k_B T + 1} d\varepsilon \\
&= \frac{5}{3} \frac{1}{k_B T} \int_{-\infty}^{\infty} g(\varepsilon) \varepsilon \frac{1}{\exp(\varepsilon - \mu)/k_B T + 1} d\varepsilon - \frac{1}{k_B T} \int_{-\infty}^{\infty} g(\varepsilon) \mu \frac{1}{\exp(\varepsilon - \mu)/k_B T + 1} d\varepsilon \\
&= \frac{5}{3} \frac{1}{k_B T} \int_{-\infty}^{\infty} g(\varepsilon) \varepsilon \frac{1}{\exp(\varepsilon - \mu)/k_B T + 1} d\varepsilon - \frac{n\mu}{k_B T} \\
&= \frac{5}{3} \frac{1}{k_B T} u - \frac{n\mu}{k_B T} \\
&= \frac{5}{3} \frac{1}{k_B T} \left\{ \frac{3}{2} \frac{n}{\varepsilon_F^{3/2}} \frac{2}{5} \mu^{5/2} + \frac{\pi^2}{6} (k_B T)^2 \left( \frac{3}{2} \frac{n}{\varepsilon_F^{3/2}} \frac{1}{2} + \frac{3}{2} \frac{n}{\varepsilon_F^{3/2}} \right) \mu^{1/2} \right\} - \frac{n\mu}{k_B T} \\
&= \frac{1}{k_B T} \frac{n}{\varepsilon_F^{3/2}} \mu^{5/2} + \frac{5}{3} \frac{1}{k_B T} \frac{\pi^2}{6} (k_B T)^2 \frac{9}{4} \frac{n}{\varepsilon_F^{3/2}} \mu^{1/2} - \frac{n\mu}{k_B T}
\end{aligned}$$

Considering (A.2), we obtain

$$\begin{aligned}
S/k_B &= \frac{1}{k_B T} n \varepsilon_F \left( 1 - \frac{1}{3} \left( \frac{\pi k_B T}{2 \varepsilon_F} \right)^2 \right)^{5/2} + \frac{5}{3} \frac{1}{k_B T} \frac{\pi^2}{6} (k_B T)^2 \frac{n}{\varepsilon_F} \left( 1 - \frac{1}{3} \left( \frac{\pi k_B T}{2 \varepsilon_F} \right)^2 \right)^{1/2} \\
&\quad - \frac{n}{k_B T} \varepsilon_F \left( 1 - \frac{1}{3} \left( \frac{\pi k_B T}{2 \varepsilon_F} \right)^2 \right) \\
&= \frac{1}{k_B T} n \varepsilon_F \left( -\frac{1}{3} \left( \frac{\pi k_B T}{2 \varepsilon_F} \right)^2 \right)^{5/2} + \frac{5}{3} \frac{1}{k_B T} \frac{\pi^2}{6} (k_B T)^2 \frac{n}{\varepsilon_F} + \frac{n}{k_B T} \varepsilon_F \frac{1}{3} \left( \frac{\pi k_B T}{2 \varepsilon_F} \right)^2 \\
&= -\frac{5}{6} \frac{n k_B T}{\varepsilon_F} \frac{\pi^2}{4} + \frac{n k_B T}{\varepsilon_F} \frac{5}{3} \frac{9}{4} \frac{\pi^2}{6} + \frac{n k_B T}{\varepsilon_F} \frac{1}{3} \frac{\pi^2}{4} \\
&= \frac{\pi^2}{2} \frac{k_B T}{\varepsilon_F} n
\end{aligned}$$

Now, we apply an external magnetic field  $H$ . Using the Sommerfeld expansion (A.1), we obtain

$$\begin{aligned}
n_+ &= \int_{\mu_B H}^{\mu} \frac{3}{2} \frac{n}{\varepsilon_F^{3/2}} \frac{1}{2} (\varepsilon + \mu_B H)^{1/2} d\varepsilon + \frac{\pi^2}{6} (k_B T)^2 \frac{3}{2} \frac{n}{\varepsilon_F^{3/2}} \frac{1}{4} (\mu + \mu_B H)^{-1/2} \\
&= \frac{3}{2} \frac{n}{\varepsilon_F^{3/2}} \frac{1}{2} \frac{2}{3} (\mu + \mu_B H)^{3/2} + \frac{\pi^2}{6} (k_B T)^2 \frac{3}{2} \frac{n}{\varepsilon_F^{3/2}} \frac{1}{4} (\mu + \mu_B H)^{-1/2}
\end{aligned}$$

Similarly, we obtain

$$\begin{aligned}
n &= n_- + n_+ \\
&= \frac{3}{2} \frac{n}{\epsilon_F^{3/2}} 1/2 \frac{2}{3} (\mu - \mu_B H)^{3/2} + \frac{\pi^2}{6} (k_B T)^2 \frac{3}{2} \frac{n}{\epsilon_F^{3/2}} \frac{1}{4} (\mu - \mu_B H)^{-1/2} \\
&\quad + \frac{3}{2} \frac{n}{\epsilon_F^{3/2}} 1/2 \frac{2}{3} (\mu + \mu_B H)^{3/2} + \frac{\pi^2}{6} (k_B T)^2 \frac{3}{2} \frac{n}{\epsilon_F^{3/2}} \frac{1}{4} (\mu + \mu_B H)^{-1/2} \\
1 &= \frac{(\mu - \mu_B H)^{3/2}}{\epsilon_F^{3/2}} \frac{1}{2} + \frac{\pi^2}{16} (k_B T)^2 \frac{(\mu - \mu_B H)^{-1/2}}{\epsilon_F^{3/2}} \\
&\quad + \frac{(\mu + \mu_B H)^{3/2}}{\epsilon_F^{3/2}} \frac{1}{2} + \frac{\pi^2}{16} (k_B T)^2 \frac{(\mu + \mu_B H)^{-1/2}}{\epsilon_F^{3/2}} \\
1 &= \left( \frac{\mu}{\epsilon_F} - \frac{\mu_B H}{\epsilon_F} \right)^{3/2} \frac{1}{2} + \frac{\pi^2}{16} \left( \frac{k_B T}{\epsilon_F} \right)^2 \left( \frac{\mu}{\epsilon_F} - \frac{\mu_B H}{\epsilon_F} \right)^{-1/2} \\
&\quad + \left( \frac{\mu}{\epsilon_F} + \frac{\mu_B H}{\epsilon_F} \right)^{3/2} \frac{1}{2} + \frac{\pi^2}{16} \left( \frac{k_B T}{\epsilon_F} \right)^2 \left( \frac{\mu}{\epsilon_F} + \frac{\mu_B H}{\epsilon_F} \right)^{-1/2}
\end{aligned}$$

We accept that  $\mu_B H$  is comparable to  $k_B T$ , but  $\frac{\mu_B H}{\epsilon_F} \ll 1$ ,

$$\frac{\mu}{\epsilon_F} = 1 + x$$

$$\begin{aligned}
1 &= \left( 1 + x - \frac{\mu_B H}{\epsilon_F} \right)^{3/2} \frac{1}{2} + \frac{\pi^2}{16} \left( \frac{k_B T}{\epsilon_F} \right)^2 \left( 1 + x - \frac{\mu_B H}{\epsilon_F} \right)^{-1/2} \\
&\quad + \left( 1 + x + \frac{\mu_B H}{\epsilon_F} \right)^{3/2} \frac{1}{2} + \frac{\pi^2}{16} \left( \frac{k_B T}{\epsilon_F} \right)^2 \left( 1 + x + \frac{\mu_B H}{\epsilon_F} \right)^{-1/2} \\
1 &= \left\{ 1 + 3/2 \left( x - \frac{\mu_B H}{\epsilon_F} \right) + \frac{3}{2} * \frac{1}{2} \left( \frac{\mu_B H}{\epsilon_F} \right)^2 \right\} \frac{1}{2} + \frac{\pi^2}{16} \left( \frac{k_B T}{\epsilon_F} \right)^2 \left\{ 1 - \frac{1}{2} \left( x - \frac{\mu_B H}{\epsilon_F} \right) \right\} \\
&\quad + \left\{ 1 + 3/2 \left( x + \frac{\mu_B H}{\epsilon_F} \right) + \frac{3}{2} * \frac{1}{2} \left( \frac{\mu_B H}{\epsilon_F} \right)^2 \right\} \frac{1}{2} + \frac{\pi^2}{16} \left( \frac{k_B T}{\epsilon_F} \right)^2 \left\{ 1 - \frac{1}{2} \left( x + \frac{\mu_B H}{\epsilon_F} \right) \right\} \\
&= 1 + \frac{3}{2} x + \frac{3}{4} \left( \frac{\mu_B H}{\epsilon_F} \right)^2 + \frac{\pi^2}{8} \left( \frac{k_B T}{\epsilon_F} \right)^2
\end{aligned}$$

$$x = -\frac{1}{2} \left( \frac{\mu_B H}{\epsilon_F} \right)^2 - \frac{\pi^2}{12} \left( \frac{k_B T}{\epsilon_F} \right)^2$$

$$\mu = \epsilon_F \left( 1 - \frac{1}{2} \left( \frac{\mu_B H}{\epsilon_F} \right)^2 - \frac{\pi^2}{12} \left( \frac{k_B T}{\epsilon_F} \right)^2 \right)$$

---

Thus magnetization  $\mu_B(n_+ - n_-)/n$  is a function of  $H$  and  $T$ :

$$\begin{aligned}
(n_+ - n_-)/n &= \frac{3}{2} \frac{1}{\epsilon_F^{3/2}} \frac{1}{2} \frac{2}{3} (\mu + \mu_B H)^{3/2} + \frac{\pi^2}{6} (k_B T)^2 \frac{3}{2} \frac{1}{\epsilon_F^{3/2}} \frac{1}{4} (\mu + \mu_B H)^{-1/2} \\
&\quad - \frac{3}{2} \frac{1}{\epsilon_F^{3/2}} \frac{1}{2} \frac{2}{3} (\mu - \mu_B H)^{3/2} - \frac{\pi^2}{6} (k_B T)^2 \frac{3}{2} \frac{1}{\epsilon_F^{3/2}} \frac{1}{4} (\mu - \mu_B H)^{-1/2} \\
&= \frac{1}{2} + 3/2 \left(x + \frac{\mu_B H}{\epsilon_F}\right) \frac{1}{2} + \frac{\pi^2}{16} \left(\frac{k_B T}{\epsilon_F}\right)^2 \left(1 - 1/2 \left(x + \frac{\mu_B H}{\epsilon_F}\right)\right) \\
&\quad - \frac{1}{2} - 3/2 \left(x - \frac{\mu_B H}{\epsilon_F}\right) \frac{1}{2} - \frac{\pi^2}{16} \left(\frac{k_B T}{\epsilon_F}\right)^2 \left(1 - 1/2 \left(x - \frac{\mu_B H}{\epsilon_F}\right)\right) \\
&= 3/2 \frac{\mu_B H}{\epsilon_F} - \frac{\pi^2}{16} \left(\frac{k_B T}{\epsilon_F}\right)^2 \frac{\mu_B H}{\epsilon_F}
\end{aligned}$$



## Appendix B

# Generalized Valet-Fert Equation

We start with the Boltzmann equation

$$\frac{\partial g}{\partial t} + \mathbf{v} \cdot \frac{\partial}{\partial \mathbf{r}} g + \mathbf{F} \cdot \frac{1}{\hbar} \frac{\partial}{\partial \mathbf{k}} g = \left( \frac{\partial g}{\partial t} \right)_{\text{collision}}$$

$f_s(z, \mathbf{v})$  is written by adding up the Fermi-Dirac distribution  $f^0(v)$  and small perturbations.

$$f^0(v) = \frac{1}{\exp(\varepsilon(v) - \mu) / k_B T + 1}$$

$$\begin{aligned} \nabla \cdot f_s(\mathbf{r}, \mathbf{v}) &= \nabla \cdot \frac{1}{\exp(\varepsilon(v) - \mu(\mathbf{r})) / k_B T(\mathbf{r}) + 1} \\ &= \frac{df}{d\eta} \nabla \cdot \{(\varepsilon(v) - \mu(\mathbf{r})) / k_B T(\mathbf{r})\} \\ &= k_B T \frac{df}{d\varepsilon} \nabla \cdot \{(\varepsilon(v) - \mu(\mathbf{r})) / k_B T(\mathbf{r})\} \\ &= -\frac{df}{d\varepsilon} \left\{ \nabla \cdot \mu(\mathbf{r}) + \frac{\varepsilon - \mu}{T} \nabla \cdot T(\mathbf{r}) \right\} \end{aligned}$$

$$f_s(z, \mathbf{v}) = f_s^0(v) + \frac{\partial f_s^0}{\partial \varepsilon} \{[\mu^0 - \mu_s(z)] + g_s(z, \mathbf{v})\}$$

where  $g_s(z, \mathbf{v})$  is the anisotropic term.  $\mu^0 - \mu_s(z)$ , isotropic term expressing the local variations of the chemical potential, accounting for the spin accumulation. If we consider a gradient of  $H^*$  as an effective spin motive force, we obtain

$$\begin{aligned} &v_z \frac{\partial f_s}{\partial z}(z, \mathbf{v}) - eE(z) v_z \frac{\partial f_s^0}{\partial \varepsilon}(z, \mathbf{v}) - \mu_B \nabla H_s^* v_z \frac{\partial f_s^0}{\partial \varepsilon}(z, \mathbf{v}) \\ &= \int d^3 v' \delta[\varepsilon(v') - \varepsilon(v)] P_s[z, \varepsilon(v)] [f_s(z, \mathbf{v}') - f_s(z, \mathbf{v})] \\ &\quad + \int d^3 v' \delta[\varepsilon(v') - \varepsilon(v)] P_{sf}[z, \varepsilon(v)] [f_{-s}(z, \mathbf{v}') - f_s(z, \mathbf{v})] \end{aligned}$$

$$\begin{aligned}
 & v_z \frac{\partial f_s^0}{\partial \epsilon} \frac{\partial \{[\mu^0 - \mu_s(z)] + \alpha_s [T^0 - T(\mathbf{z})] + g_s(z, \mathbf{v})\}}{\partial z} - eE(z) v_z \frac{\partial f_s^0}{\partial \epsilon}(z, \mathbf{v}) - \mu_B \nabla H_s^* v_z \frac{\partial f_s^0}{\partial \epsilon}(z, \mathbf{v}) \\
 = & \frac{\partial f_s^0}{\partial \epsilon} \left\{ v_z \frac{\partial g_s}{\partial z}(z, \mathbf{v}) - v_z \frac{\partial \{ \mu_s(z) - eV(z) + \alpha_s T(\mathbf{z}) + \mu_B H_s^* \}}{\partial z} \right\} \\
 & \int d^3 v' \delta[\epsilon(v') - \epsilon(v)] P_s[z, \epsilon(v)] [f_s(z, \mathbf{v}') - f_s(z, \mathbf{v})] \\
 = & \int d^3 v' \frac{\partial f_s^0}{\partial \epsilon} \delta[\epsilon(v') - \epsilon(v)] P_s[z, \epsilon(v)] [g_s(z, \mathbf{v}') - g_s(z, \mathbf{v})] \\
 = & - \frac{\partial f_s^0}{\partial \epsilon} P_s[z, \epsilon(v)] \int d^3 v' [g_s(z, \mathbf{v}) - g_s(z, \mathbf{v}')|_{v'=v}] \\
 = & - \frac{\partial f_s^0}{\partial \epsilon} \frac{1}{\tau_s} g_s(z, \mathbf{v}) \\
 & \int d^3 v' \delta[\epsilon(v') - \epsilon(v)] P_{sf}[z, \epsilon(v)] [f_{-s}(z, \mathbf{v}') - f_s(z, \mathbf{v})] \\
 = & \int d^3 v' \delta[\epsilon(v') - \epsilon(v)] P_{sf}[z, \epsilon(v)] [\mu_s(z) - \mu_{-s}(z) - g_s(z, \mathbf{v}) + g_s(z, \mathbf{v}')|_{v'=v}] \\
 = & - \frac{\partial f_s^0}{\partial \epsilon} P_{sf}[z, \epsilon(v)] \int d^3 v' [g_s(z, \mathbf{v}) - g_s(z, \mathbf{v}')|_{v'=v}] \\
 & + \frac{\partial f_s^0}{\partial \epsilon} P_{sf}[z, \epsilon(v)] \int d^3 v' [\mu_s(z) - \mu_{-s}(z)] \\
 = & - \frac{\partial f_s^0}{\partial \epsilon} \frac{1}{\tau_{sf}} g_s(z, \mathbf{v}) + \frac{\partial f_s^0}{\partial \epsilon} \frac{\mu_s(z) - \mu_{-s}(z)}{\tau_{sf}} \\
 v_z \frac{\partial g_s}{\partial z}(z, \mathbf{v}) + \left[ \frac{1}{\tau_s} + \frac{1}{\tau_{sf}} \right] g_s(z, \mathbf{v}) = & v_z \frac{\partial \{ \mu_s(z) - eV(z) + \alpha_s T(\mathbf{z}) + \mu_B H_s^* \}}{\partial z} + \frac{\mu_s(z) - \mu_{-s}(z)}{\tau_{sf}} \\
 j_s = & \frac{\sigma_s}{e} \frac{\partial [\mu_s(z) - eV(z) + \alpha_s T(\mathbf{z}) + H_s^*]}{\partial z} \\
 \frac{\partial j_s}{\partial z} = & \frac{\sigma_s}{e} \frac{\mu_s(z) - \mu_{-s}(z)}{l_s^2} \\
 \frac{2\sigma'_{-s}}{\sigma'_s + \sigma'_{-s}} \nabla^2 \mu_s^*(z) - \frac{\sigma_{-s}}{\sigma_s} \frac{2\sigma'_s}{\sigma'_s + \sigma'_{-s}} \nabla^2 \mu_{-s}^*(z) = & \frac{\mu_s^*(z) - \mu_{-s}^*(z) - 2H_s^*}{l_{sf}^2} \\
 \bar{\mu}_s(z) - \bar{\mu}_{-s}(z) = & e^{-z/l_{sf}} \\
 \mu_s^*(z) - \mu_{-s}^*(z) = & 2H_s^*
 \end{aligned}$$

# Bibliography

- [1] A. Ohtomo and H. Y. Hwang, *A high-mobility electron gas at the LaAlO<sub>3</sub>|SrTiO<sub>3</sub> heterointerface*, Nature **427**, 423 (2004).
- [2] Y. Kamihara, T. Watanabe, M. Hirano, and H. Hosono, *Iron-Based Layered Superconductor La[O<sub>1-x</sub>F<sub>x</sub>]FeAs (x~0.05-0.12) with T<sub>c</sub>~26 K*, Journal of American Chemical Society **130**, 3296 (2008).
- [3] K. Uchida, S. Takahashi, K. Harii, J. Ieda, W. Koshibae, K. Ando, S. Maekawa, and E. Saitoh, *Observation of the spin Seebeck effect*, Nature **455**, 778 (2008).
- [4] P. Hohenberg and W. Kohn, *Inhomogeneous Electron Gas*, Phys. Rev. **136**, B864 (1964).
- [5] W. Kohn and L. J. Sham, *Self-Consistent Equations Including Exchange and Correlation Effects*, Phys. Rev. **140**, A1133 (1965).
- [6] D. M. Ceperley and B. J. Alder, *Ground State of the Electron Gas by a Stochastic Method*, Phys. Rev. Lett. **45**, 566 (1980).
- [7] J. P. Perdew and A. Zunger, *Self-interaction correction to density-functional approximations for many-electron systems*, Phys. Rev. B **23**, 5048 (1981).
- [8] J. Hubbard, *Electron Correlations in Narrow Energy Bands*, Proceedings of the Royal Society of London. Series A, Mathematical and Physical Sciences **276**, pp. 238 (1963).
- [9] S. L. Dudarev, G. A. Botton, S. Y. Savrasov, C. J. Humphreys, and A. P. Sutton, *Electron-energy-loss spectra and the structural stability of nickel oxide: An LSDA+U study*, Phys. Rev. B **57**, 1505 (1998).
- [10] <http://en.wikipedia.org/wiki/Perovskitestructure>, (2011).
- [11] M. Imada, A. Fujimori, and Y. Tokura, *Metal-insulator transitions*, Rev. Mod. Phys. **70**, 1039 (1998).
- [12] M. Johnsson and P. Lemmens, *Crystallography and Chemistry of Perovskites*, Handbook of Magnetism and Advanced Magnetic Media;cond-mat/0506606 (2005).



- [13] R. D. Shannon, *Revised Effective Ionic Radii and Systematic Studies of Interatomic Distances in Halides and Chalcogenides*, Acta Crystallographica; <http://abulafia.mt.ic.ac.uk/shannon/radius.php> **A32**, 751 (1976).
- [14] M. Kawasaki, K. Takahashi, T. Maeda, R. Tsuchiya, M. Shinohara, O. Ishiyama, T. Yonezawa, M. Yoshimoto, and H. Koinuma, *Atomic Control of the SrTiO<sub>3</sub> Crystal Surface*, Science **266**, 1540 (1994).
- [15] G. Koster, B. L. Kropman, G. J. H. M. Rijnders, D. H. A. Blank, and H. Rogalla, *Quasi-ideal strontium titanate crystal surfaces through formation of strontium hydroxide*, Applied Physics Letters **73**, 2920 (1998).
- [16] D. A. MacLean, H.-N. Ng, and J. E. Greedan, *Crystal Structure and Crystal Chemistry of the RTiO<sub>3</sub> Perovskites RE = La, Nd, Sm, Gd, Y*, J. Solid State Chem. **30**, 35 (1979).
- [17] M. Cwik, T. Lorenz, J. Baier, R. Müller, G. André, F. Bourée, F. Lichtenberg, A. Freimuth, R. Schmitz, E. Müller-Hartmann, and M. Braden, *Crystal and magnetic structure of LaTiO<sub>3</sub>: Evidence for nondegenerate t<sub>2g</sub> orbitals*, Phys. Rev. B **68**, 060401(R) (2003).
- [18] J. Hemberger, H.-A. K. von Nidda, V. Fritsch, J. Deisenhofer, S. Lobina, T. Rudolf, P. Lunkenheimer, F. Lichtenberg, A. Loidl, D. Bruns, and B. Büchner, *Evidence for Jahn-Teller Distortions at the Antiferromagnetic Transition in LaTiO<sub>3</sub>*, Phys. Rev. Lett. **91**, 066403 (2003).
- [19] Y. Okimoto, T. Katsufuji, Y. Okada, T. Arima, and Y. Tokura, *Optical spectra in (La,Y)TiO<sub>3</sub>: Variation of Mott-Hubbard gap features with change of electron correlation and band filling*, Phys. Rev. B **51**, 9581 (1995).
- [20] [http://en.wikipedia.org/wiki/Crystal\\_field\\_theory](http://en.wikipedia.org/wiki/Crystal_field_theory), (2011).
- [21] E. Pavarini, S. Biermann, A. Poteryaev, A. I. Lichtenstein, A. Georges, and O. K. Andersen, *Mott Transition and Suppression of Orbital Fluctuations in Orthorhombic 3d<sup>1</sup> Perovskites*, Phys. Rev. Lett. **92**, 176403 (2004).
- [22] M. Mochizuki and M. Imada, *Orbital-Spin Structure and Lattice Coupling in RTiO<sub>3</sub> where R = La, Pr, Nd, and Sm*, Phys. Rev. Lett. **91**, 167203 (2003).
- [23] M. Huijben, G. Rijnders, D. H. A. Blank, S. Bals, S. V. Aert, J. Verbeeck, G. V. Tendeloo, A. Brinkman, and H. Hilgenkamp, *Electronically coupled complementary interfaces between perovskite band insulators*, Nature Materials **5**, 556 (2006).
- [24] S. Thiel, G. Hammerl, A. Schmehl, C. W. Schneider, and J. Mannhart, *Tunable Quasi-Two-Dimensional Electron Gases in Oxide Heterostructures*, Science **313**, 1942 (2006).

- [25] A. Brinkman, M. Huijben, M. V. Zalk, J. Huijben, U. Zeitler, J. C. Maan, W. G. V. D. Wiel, G. Rijnders, D. H. A. Blank, and H. HilGenkamp, *Magnetic effects at the interface between non-magnetic oxides*, Nature Materials **6**, 493 (2007).
- [26] N. Reyren, S. Thiel, A. D. Caviglia, L. F. Kourkoutis, G. Hammer, C. Richter, C. W. Schneider, T. Kopp, A.-S. Rüetschi, D. Jaccard, M. Gabay, D. A. Muller, J.-M. Triscone, and J. Mannhart, *Superconducting Interfaces Between Insulating Oxides*, Science **317**, 1196 (2007).
- [27] C. Cen, S. Thiel, G. Hammerl, C. W. Schneider, K. E. Andersen, C. S. Hellberg, J. Mannhart, and J. Levy, *Nanoscale control of an interfacial metal–insulator transition at room temperature*, Nature Materials **7**, 298 (2008).
- [28] A. D. Caviglia, S. Gariglio, N. Reyren, D. Jaccard, T. Schneider, M. Gabay, S. Thiel, G. Hammerl, J. Mannhart, and J.-M. Triscone, *Electric field control of the LaAlO<sub>3</sub>/SrTiO<sub>3</sub> interface ground state*, Nature **456**, 624 (2008).
- [29] M. Ben Shalom, A. Ron, A. Palevski, and Y. Dagan, *Shubnikov–De Haas Oscillations in SrTiO<sub>3</sub>/LaAlO<sub>3</sub> Interface*, Phys. Rev. Lett. **105**, 206401 (2010).
- [30] M. Ben Shalom, M. Sachs, D. Rakhmilevitch, A. Palevski, and Y. Dagan, *Tuning Spin-Orbit Coupling and Superconductivity at the SrTiO<sub>3</sub>/LaAlO<sub>3</sub> Interface: A Magnetotransport Study*, Phys. Rev. Lett. **104**, 126802 (2010).
- [31] A. D. Caviglia, S. Gariglio, C. Cancellieri, B. Sacépé, A. Fête, N. Reyren, M. Gabay, A. F. Morpurgo, and J.-M. Triscone, *Two-Dimensional Quantum Oscillations of the Conductance at LaAlO<sub>3</sub>/SrTiO<sub>3</sub> Interfaces*, Phys. Rev. Lett. **105**, 236802 (2010).
- [32] A. D. Caviglia, M. Gabay, S. Gariglio, N. Reyren, C. Cancellieri, and J.-M. Triscone, *Tunable Rashba Spin-Orbit Interaction at Oxide Interfaces*, Phys. Rev. Lett. **104**, 126803 (2010).
- [33] N. Nakagawa, H. Y. Hwang, and D. A. Muller, *Why some interfaces cannot be sharp*, Nature Materials **5**, 204 (2006).
- [34] W. Siemons, G. Koster, H. Yamamoto, W. A. Harrison, G. Lucovsky, T. H. Geballe, D. H. A. Blank, and M. R. Beasley, *Origin of Charge Density at LaAlO<sub>3</sub> on SrTiO<sub>3</sub> Heterointerfaces: Possibility of Intrinsic Doping*, Phys. Rev. Lett. **98**, 196802 (2007).
- [35] G. Herranz, M. Basletić, M. Bibes, C. Carrétéro, E. Tafra, E. Jacquet, K. Bouzehouane, C. Deranlot, A. Hamzić, J.-M. Broto, A. Barthélémy, and A. Fert, *High Mobility in LaAlO<sub>3</sub>=SrTiO<sub>3</sub> Heterostructures: Origin, Dimensionality, and Perspectives*, Phys. Rev. Lett. **98**, 216803 (2007).

- [36] M. Basletic, J.-L. Maurice, C. Carrétero, G. Herranz, O. Copie, M. Bibes, E. Jacquet, K. Bouzehouane, S. Fusil, and A. Barthélémy, *Mapping the spatial distribution of charge carriers in LaAlO<sub>3</sub>|SrTiO<sub>3</sub> heterostructures*, Nature Materials **7**, 621 (2008).
- [37] K. Yoshimatsu, R. Yasuhara, H. Kumigashira, and M. Oshima, *Origin of Metallic States at the Heterointerface between the Band Insulators LaAlO<sub>3</sub> and SrTiO<sub>3</sub>*, Phys. Rev. Lett. **101**, 026802 (2008).
- [38] P. R. Willmott, S. A. Pauli, R. Herger, C. M. Schlepütz, D. Martoccia, B. D. Patterson, B. Delley, R. Clarke, D. Kumah, C. Cionca, and Y. Yacoby, *Structural Basis for the Conducting Interface between LaAlO<sub>3</sub> and SrTiO<sub>3</sub>*, Phys. Rev. Lett. **99**, 155502 (2007).
- [39] A. Kalabukhov, R. Gunnarsson, J. Börjesson, E. Olsson, T. Claeson, and D. Winkler, *Effect of oxygen vacancies in the SrTiO<sub>3</sub> substrate on the electrical properties of the LaAlO<sub>3</sub>|SrTiO<sub>3</sub> interface*, Phys. Rev. B **75**, 121404(R) (2007).
- [40] A. S. Kalabukhov, Y. A. Boikov, I. T. Serenkov, V. I. Sakharov, V. N. Popok, R. Gunnarsson, J. Börjesson, N. Ljustina, E. Olsson, D. Winkler, and T. Claeson, *Cationic Disorder and Phase Segregation in LaAlO<sub>3</sub>/SrTiO<sub>3</sub> Heterointerfaces Evidenced by Medium-Energy Ion Spectroscopy*, Phys. Rev. Lett. **103**, 146101 (2009).
- [41] T. Fix, F. Schoofs, J. L. MacManus-Driscoll, and M. G. Blamire, *Charge Confinement and Doping at LaAlO<sub>3</sub>-SrTiO<sub>3</sub> Interfaces*, Phys. Rev. Lett. **103**, 166802 (2009).
- [42] M. Sing, G. Berner, K. Goß, A. Müller, A. Ruff, A. Wetscherek, S. Thiel, J. Mannhart, S. A. Pauli, C. W. Schneider, P. R. Willmott, M. Gorgoi, F. Schäfers, and R. Claessen, *Profiling the Interface Electron Gas of LaAlO<sub>3</sub>/SrTiO<sub>3</sub> Heterostructures with Hard X-Ray Photoelectron Spectroscopy*, Phys. Rev. Lett. **102**, 176805 (2009).
- [43] Y. Segal, J. H. Ngai, J. W. Reiner, F. J. Walker, and C. H. Ahn, *X-ray photoemission studies of the metal-insulator transition in LaAlO<sub>3</sub>/SrTiO<sub>3</sub> structures grown by molecular beam epitaxy*, Phys. Rev. B **80**, 241107 (2009).
- [44] R. Pentcheva and W. E. Pickett, *Avoiding the Polarization Catastrophe in LaAlO<sub>3</sub> Overlayers on SrTiO<sub>3</sub>(001) through Polar Distortion*, Phys. Rev. Lett. **102**, 107602 (2009).
- [45] S. A. Pauli, S. J. Leake, B. Delley, M. Björck, C. W. Schneider, C. M. Schlepütz, D. Martoccia, S. Paetel, J. Mannhart, and P. R. Willmott, *Evolution of the Interfacial Structure of LaAlO<sub>3</sub> on SrTiO<sub>3</sub>*, Phys. Rev. Lett. **106**, 036101 (2011).

- [46] S. Chambers, M. Engelhard, V. Shutthanandan, Z. Zhu, T. Droubay, L. Qiao, P. Sushko, T. Feng, H. Lee, T. Gustafsson, E. Garfunkel, A. Shah, J.-M. Zuo, and Q. Ramasse, *Instability, intermixing and electronic structure at the epitaxial heterojunction*, Surface Science Reports **65**, 317 (2010).
- [47] M. Salluzzo, J. C. Cezar, N. B. Brookes, V. Bisogni, G. M. De Luca, C. Richter, S. Thiel, J. Mannhart, M. Huijben, A. Brinkman, G. Rijnders, and G. Ghiringhelli, *Orbital Reconstruction and the Two-Dimensional Electron Gas at the  $\text{LaAlO}_3/\text{SrTiO}_3$  Interface*, Phys. Rev. Lett. **102**, 166804 (2009).
- [48] N. Ogawa, K. Miyano, M. Hosoda, T. Higuchi, C. Bell, Y. Hikita, and H. Y. Hwang, *Enhanced lattice polarization in  $\text{SrTiO}_3/\text{LaAlO}_3$  superlattices measured using optical second-harmonic generation*, Phys. Rev. B **80**, 081106 (2009).
- [49] A. Savoia, D. Paparo, P. Perna, Z. Ristic, M. Salluzzo, F. M. Granozio, U. S. di Uccio, C. Richter, S. Thiel, J. Mannhart, and L. Marrucci, *Polar catastrophe and electronic reconstructions at the  $\text{LaAlO}_3/\text{SrTiO}_3$  interface: Evidence from optical second harmonic generation*, Phys. Rev. B **80**, 075110 (2009).
- [50] C. L. Jia, S. B. Mi, M. Faley, U. Poppe, J. Schubert, and K. Urban, *Oxygen octahedron reconstruction in the  $\text{SrTiO}_3/\text{LaAlO}_3$  heterointerfaces investigated using aberration-corrected ultrahigh-resolution transmission electron microscopy*, Phys. Rev. B **79**, 081405 (2009).
- [51] V. Vonk, M. Huijben, K. J. I. Driessen, P. Tinnemans, A. Brinkman, S. Harkema, and H. Graafsma, *Interface structure of  $\text{SrTiO}_3/\text{LaAlO}_3$  at elevated temperatures studied in situ by synchrotron x rays*, Phys. Rev. B **75**, 235417 (2007).
- [52] A. Ohtomo and H. Y. Hwang, *Growth mode control of the free carrier density in  $\text{SrTiO}_3$  films*, Journal of Applied Physics **102**, 083704 (2007).
- [53] M. S. Park, S. H. Rhim, and J. Freeman, *Charge compensation and mixed valency in  $\text{LaAlO}_3/\text{SrTiO}_3$  heterointerfaces studied by the FLAPW method*, Phys. Rev. B **74**, 205416 (2006).
- [54] J.-M. Albina, M. Mrovec, B. Meyer, and C. Elsässer, *Structure, stability, and electronic properties of  $\text{SrTiO}_3/\text{LaAlO}_3$  and  $\text{SrTiO}_3/\text{SrRuO}_3$  interfaces*, Phys. Rev. B **76**, 165103 (2007).
- [55] R. Pentcheva and W. E. Pickett, *Charge localization or itineracy at  $\text{LaAlO}_3/\text{SrTiO}_3$  interfaces: Hole polarons, oxygen vacancies, and mobile electrons*, Phys. Rev. B **74**, 035112 (2006).
- [56] R. Pentcheva and W. E. Pickett, *Ionic relaxation contribution to the electronic reconstruction at the  $n$ -type  $\text{LaAlO}_3/\text{SrTiO}_3$  interface*, Phys. Rev. B **78**, 205106 (2008).

- [57] R. Pentcheva and W. E. Pickett, *Correlation-Driven Charge Order at the Interface between a Mott and a Band Insulator*, Phys. Rev. Lett. **99**, 016802 (2007).
- [58] R. Pentcheva, M. Huijben, K. Otte, W. E. Pickett, J. E. Kleibeuker, J. Huijben, H. Boschker, D. Kockmann, W. Siemons, G. Koster, H. J. W. Zandvliet, G. Rijnders, D. H. A. Blank, H. Hilgenkamp, and A. Brinkman, *Parallel Electron-Hole Bilayer Conductivity from Electronic Interface Reconstruction*, Phys. Rev. Lett. **104**, 166804 (2010).
- [59] S. Ishibashi and K. Terakura, *Analysis of Screening Mechanisms for Polar Discontinuity for LaAlO<sub>3</sub>/SrTiO<sub>3</sub> Thin Films Based on Ab initio Calculations*, Journal of the Physical Society of Japan **77**, 104706 (2008).
- [60] U. Schwingenschlogl and C. Schuster, *Interface relaxation and electrostatic charge depletion in the oxide heterostructure LaAlO<sub>3</sub>/SrTiO<sub>3</sub>*, Europhys. Lett. **86**, 27005 (2009).
- [61] K. Janicka, J. P. Velev, and E. Y. Tsymbal, *Quantum Nature of Two-Dimensional Electron Gas Confinement at LaAlO<sub>3</sub>/SrTiO<sub>3</sub> Interfaces*, Phys. Rev. Lett. **102**, 106803 (2009).
- [62] Z. Zhong and P. J. Kelly, *Electronic structure induced reconstruction and magnetic ordering at the LaAlO<sub>3</sub>/SrTiO<sub>3</sub> interface*, Europhys. Lett. **84**, 27001 (2008).
- [63] Z. Zhong, P. X. Xu, and P. J. Kelly, *Polarity-induced oxygen vacancies at LaAlO<sub>3</sub>/SrTiO<sub>3</sub> interfaces*, Phys. Rev. B **82**, 165127 (2010).
- [64] Z. S. Popovic, S. Satpathy, and R. M. Martin, *Origin of the Two-Dimensional Electron Gas Carrier Density at the LaAlO<sub>3</sub> on SrTiO<sub>3</sub> Interface*, Phys. Rev. Lett. **101**, 256801 (2008).
- [65] H. Chen, A. Kolpak, and S. Ismail-Beigi, *First-principles study of electronic reconstructions of LaAlO<sub>3</sub>/SrTiO<sub>3</sub> heterointerfaces and their variants*, Phys. Rev. B **82**, 085430 (2010).
- [66] J. Lee and A. A. Demkov, *Charge origin and localization at the n -type SrTiO<sub>3</sub>/LaAlO<sub>3</sub> interface*, Phys. Rev. B **78**, 193104 (2008).
- [67] W.-j. Son, E. Cho, B. Lee, J. Lee, and S. Han, *Density and spatial distribution of charge carriers in the intrinsic n -type LaAlO<sub>3</sub> – SrTiO<sub>3</sub> interface*, Phys. Rev. B **79**, 245411 (2009).
- [68] N. C. Bristowe, E. Artacho, and P. B. Littlewood, *Oxide superlattices with alternating p and n interfaces*, Phys. Rev. B **80**, 045425 (2009).

- [69] J. Verbeeck, S. Bals, A. N. Kravtsova, D. Lamoen, M. Luysberg, M. Huijben, G. Rijnders, A. Brinkman, H. Hilgenkamp, D. H. A. Blank, and G. Van Tendeloo, *Electronic reconstruction at n -type SrTiO<sub>3</sub>/LaAlO<sub>3</sub> interfaces*, Phys. Rev. B **81**, 085113 (2010).
- [70] M. Huijben, A. Brinkman, G. Koster, G. Rijnders, H. Hilgenkamp, and D. H. A. Blank, *Structure-Property Relation of SrTiO<sub>3</sub>/LaAlO<sub>3</sub> Interfaces*, **21**, 1665 (2009).
- [71] H. Chen, A. M. Kolpak, and S. Ismail-Beigi, *Fundamental asymmetry in interfacial electronic reconstruction between insulating oxides: An ab-initio study*, Phys. Rev. B **79**, 161402 (2009).
- [72] S. Kumar and J. van den Brink, *Charge ordering and magnetism in quarter-filled Hubbard-Holstein model*, Phys. Rev. B **78**, 155123 (2008).
- [73] J. Goniakowski, F. Finocchi, and C. Noguera, *Polarity of oxide surfaces and nanostructures*, Rep. Prog. Phys. **71**, 016501 (2008).
- [74] P. E. Blöchl, *Projector augmented-wave method*, Phys. Rev. B **50**, 17953 (1994).
- [75] G. Kresse and D. Joubert, *From ultrasoft pseudopotentials to the projector augmented-wave method*, Phys. Rev. B **59**, 1758 (1999).
- [76] S. B. Zhang and J. E. Northrup, *Chemical potential dependence of Defect Formation energies in GaAs*, Phys. Rev. Lett. **67**, 2339 (1991).
- [77] K. Reuter and M. Scheffler, *Composition, structure, and stability of RuO<sub>2</sub>(110) as a function of oxygen pressure*, Phys. Rev. B **65**, 035406 (2001).
- [78] J. P. Buban, H. Iddir, and S. Ögüt, *Structural and electronic properties of oxygen vacancies in cubic and antiferrodistortive phases of SrTiO<sub>3</sub>*, Phys. Rev. B **69**, 180102 (2004).
- [79] J. Goniakowski, C. Noguera, and L. Giordano, *Prediction of Uncompensated Polarity in Ultrathin Films*, Phys. Rev. Lett. **98**, 205701 (2007).
- [80] L. Zhang, X.-F. Zhou, H.-T. Wang, J.-J. Xu, J. Li, E. G. Wang, and S.-H. Wei, *Origin of insulating behavior of the p -type LaAlO<sub>3</sub>/SrTiO<sub>3</sub> interface: Polarization-induced asymmetric distribution of oxygen vacancies*, Phys. Rev. B **82**, 125412 (2010).
- [81] N. C. Bristowe, P. B. Littlewood, and E. Artacho, *Surface defects and conduction in polar oxide heterostructures*, Phys. Rev. B **83**, 205405 (2011).
- [82] Y. Li, S. N. Phattalung, S. Limpijumnong, and J. Yu, *Oxygen-vacancy-induced charge carrier in n-type interface of LaAlO<sub>3</sub> overlayer on SrTiO<sub>3</sub> (001): interface vs bulk doping carrier*, cond-mat/ arXiv:0912.4805v1 (2009).

- [83] I. Solovyev and N. Hamada,  *$t_{2g}$  versus all 3d localization in  $\text{LaMO}_3$  perovskites ( $M=\text{Ti-Cu}$ ): First-principles study*, Phys. Rev. B **53**, 7158 (1996).
- [84] S. Okamoto and A. J. Millis, *Electronic reconstruction at an interface between a Mott insulator and a band insulator*, Nature **428**, 630 (2004).
- [85] W.-C. Lee and A. H. MacDonald, *Electronic interface reconstruction at polar-nonpolar Mott-insulator heterojunctions*, Phys. Rev. B **76**, 075339 (2007).
- [86] K. M. Rabe and P. Ghosez, *First-principles studies of ferroelectric oxides*, Topics in Applied Physics **105**, 117 (2007).
- [87] E. Pavarini, A. Yamasaki, J. Nuss, and O. K. Andersen, *How chemistry controls electron localization in  $3d^1$  perovskites: a Wannier-function study*, **7**, 188 (2005).
- [88] V. I. Anisimov, F. Aryasetiawan, and A. I. Lichtenstein, *First-principles calculations of the electronic structure and spectra of strongly correlated systems: the LDA +  $U$  method*, J. Phys.: Condens. Matter. **9**, 767 (1997).
- [89] S. Okatov, A. Poteryaev, and A. Lichtenstein, *Structural distortions and orbital ordering in  $\text{LaTiO}_3$  and  $\text{YTiO}_3$* , Europhys. Lett. **70**, 499 (2005).
- [90] G. Kresse and J. Hafner, *Ab-initio Molecular-Dynamics for Liquid-Metals*, Phys. Rev. B **47**, 558 (1993).
- [91] G. Kresse and J. Furthmuller, *Efficient iterative schemes for ab initio total-energy calculations using a plane-wave basis set*, Phys. Rev. B **54**, 11169 (1996).
- [92] P. E. Blöchl, O. Jepsen, and O. K. Andersen, *Improved Tetrahedron Method for Brillouin-Zone Integrations*, Phys. Rev. B **49**, 16223 (1994).
- [93] S. Okamoto, A. J. Millis, and N. A. Spaldin, *Lattice Relaxation in Oxide Heterostructures:  $\text{LaTiO}_3|\text{SrTiO}_3$  Superlattices*, Phys. Rev. Lett. **97**, 056802 (2006).
- [94] M. Huijben, G. Koster, H. J. A. Molegraaf, M. K. Kruize, S. Wenderich, J. E. Kleibeuker, A. McCollam, V. K. Guduru, A. Brinkman, H. Hilgenkamp, U. Zeitler, J. C. Maan, D. H. A. Blank, and G. Rijnders, *High mobility interface electron gas by defect scavenging in a modulation doped oxide heterostructure*, e-print arXiv:cond-mat/1008.1896v1 .
- [95] W. A. Harrison, E. A. Kraut, J. R. Waldrop, and R. W. Grant, *Polar heterojunction interfaces*, Phys. Rev. B **18**, 4402 (1978).
- [96] J. Chakhalian, J. W. Freeland, H.-U. Habermeier, G. Cristiani, G. Khaliullin, M. van Veenendaal, and B. Keimer, *Orbital Reconstruction and Covalent Bonding at an Oxide Interface*, Science **318**, 1115 (2007).

- [97] J. Junquera and P. Ghosez, *Critical thickness for ferroelectricity in perovskite ultrathin films*, Nature **422**, 506 (2003).
- [98] M. F. Chisholm, W. Luo, M. P. Oxley, S. T. Pantelides, and H. N. Lee, *Atomic-Scale Compensation Phenomena at Polar Interfaces*, Phys. Rev. Lett. **105**, 197602 (2010).
- [99] T. Siegrist, S. M. Zahurak, D. W. Murphy, and R. S. Roth, *The parent structure of the layered high-temperature superconductors*, Nature **334**, 231 (1988).
- [100] M. Takano, Y. Takeda, H. Okada, M. Miyamoto, and T. Kusaka, *ACuO<sub>2</sub> (A: alkaline earth) crystallizing in a layered structure*, Physica C **159**, 375 (1989).
- [101] J.-M. Triscone and O. Fischer, *Superlattices of high-temperature superconductors: synthetically modulated structures, critical temperatures and vortex dynamics*, Rep. Prog. Phys. **60**, 1673 (1997).
- [102] A. J. Millis and D. G. Schlom, *Electron-hole liquids in transition-metal oxide heterostructures*, Phys. Rev. B **82**, 073101 (2010).
- [103] V. I. Anisimov, J. Zaanen, and O. K. Andersen, *Band theory and Mott insulators: Hubbard U instead of Stoner I*, Phys. Rev. B **44**, 943 (1991).
- [104] N. Kobayashi, Z. Hiroi, and M. Takano, *Compounds and Phase Relations in the SrO-CaO-CuO System under High Pressure*, J. Solid State Chem. **132**, 274 (1997).
- [105] N. Motoyama, H. Eisaki, and S. Uchida, *Magnetic Susceptibility of Ideal Spin 1/2 Heisenberg Antiferromagnetic Chain Systems, Sr<sub>2</sub>CuO<sub>3</sub> and SrCuO<sub>2</sub>*, Phys. Rev. Lett. **76**, 3212 (1996).
- [106] G. Koster, A. Brinkman, H. Hilgenkamp, A. J. H. M. Rijnders, and D. H. A. Blank, *High-T<sub>c</sub> superconducting thin films with composition control on a sub-unit cell level; the effect of the polar nature of the cuprates*, J. Phys.: Condens. Matter. **20**, 264007 (2009).
- [107] D. Vaknin, E. Caignol, P. K. Davies, J. E. Fischer, D. C. Johnston, and D. P. Goshorn, *Antiferromagnetism in (Ca<sub>0.85</sub>Sr<sub>0.15</sub>)CuO<sub>2</sub>, the parent of the cuprate family of superconducting compounds*, Phys. Rev. B **39**, 9122 (1989).
- [108] N. Pavlenko, I. Elfimov, T. Kopp, and G. A. Sawatzky, *Interface hole doping in cuprate-titanate superlattices*, Phys. Rev. B **75**, 140512 (2007).
- [109] M. A. Hossain, J. D. F. Mottershead, D. Fournier, A. Bostwick, J. L. McChesney, E. Rotenberg, R. Liang, W. N. Hardy, G. A. Sawatzky, I. S. Elfimov, D. A. Bonn, and A. Damascelli, *In situ doping control of the surface of high-temperature superconductors*, Nature Physics **4**, 527 (2008).



- [110] H. Takahashi, K. Igawa, K. Arii, Y. Kamihara, M. Hirano, and H. Hosono, *Superconductivity at 43 K in an iron-based layered compound LaO<sub>1-x</sub>F<sub>x</sub>FeAs*, Nature **453**, 376 (2008).
- [111] F. Hunte, J. Jaroszynski, A. Gurevich, D. C. Larbalestier, R. Jin, A. S. Sefat, M. A. McGuire, B. C. Sales, D. K. Christen, and D. Mandrus, *Two-band superconductivity in LaFeAsO<sub>0.89</sub>F<sub>0.11</sub> at very high magnetic fields*, Nature **453**, 903 (2008).
- [112] X. H. Chen, T. Wu, G. Wu, R. H. Liu, H. Chen, and D. F. Fang, *Superconductivity at 43 K in SmFeAsO<sub>1-x</sub>F<sub>x</sub>*, Nature **453**, 761 (2008).
- [113] C. de la Cruz, Q. Huang, J. W. Lynn, J. Li, W. Ratcliff II, J. L. Zarestky, H. A. Mook, G. F. Chen, J. L. Luo, N. L. Wang, and P. Dai, *Magnetic order close to superconductivity in the iron-based layered LaO<sub>1-x</sub>F<sub>x</sub>FeAs systems*, Nature **453**, 899 (2008).
- [114] G. F. Chen, Z. Li, D. Wu, G. Li, W. Z. Hu, J. Dong, P. Zheng, J. L. Luo, and N. L. Wang, *Superconductivity at 41 K and Its Competition with Spin-Density-Wave Instability in Layered CeO<sub>1-x</sub>F<sub>x</sub>FeAs*, Phys. Rev. Lett. **100**, 247002 (2008).
- [115] Z.-A. Ren, G.-C. Che, X.-L. Dong, J. Yang, W. Lu, W. Yi, X.-L. Shen, Z.-C. Li, L.-L. Sun, F. Zhou, and Z.-X. Zhao, *Superconductivity and phase diagram in iron-based arsenic-oxides ReFeAsO<sub>1-δ</sub> (Re = rare-earth metal) without fluorine doping*, Europhys. Lett. **83**, 17002 (2008).
- [116] J. Dong, H. J. Zhang, G. Xu, Z. Li, G. Li, W. Z. Hu, D. Wu, G. F. Chen, X. Dai, J. L. Luo, Z. Fang, and N. L. Wang, *Competing orders and spin-density-wave instability in La(O<sub>1-x</sub>F<sub>x</sub>)FeAs*, Europhys. Lett. **83**, 27006 (2008).
- [117] Y. Nakai, K. Ishida, Y. Kamihara, M. Hirano, and H. Hosono, *Evolution from Itinerant Antiferromagnet to Unconventional Superconductor with Fluorine Doping in La(O<sub>1-x</sub>F<sub>x</sub>)FeAs Revealed by As and La Nuclear Magnetic Resonance*, J. Phys. Soc. Jpn. **77**, 073701 (2008).
- [118] Y. Kohama, Y. Kamihara, M. Hirano, H. Kawaji, T. Atake, and H. Hosono, *Ferromagnetic spin fluctuation in LaFeAsO<sub>1-x</sub>F<sub>x</sub>*, Phys. Rev. B **78**, 020512(R) (2008).
- [119] A. J. Drew, F. L. Pratt, T. Lancaster, S. J. Blundell, P. J. Baker, R. H. Liu, G. Wu, X. H. Chen, I. Watanabe, V. K. M. A. D. K. K. M. Rossle, and C. Bernhard, *Coexistence of Magnetic Fluctuations and Superconductivity in the Pnictide High Temperature Superconductor SmFeAsO<sub>1-x</sub>F<sub>x</sub> Measured by Muon Spin Rotation*, Phys. Rev. Lett. **101**, 097010 (2008).
- [120] R. H. Liu, G. Wu, T. Wu, D. F. Fang, H. Chen, S. Y. Li, K. Liu, Y. L. Xie, X. F. Wang, R. L. Yang, L. Ding, C. He, D. L. Feng, and X. H. Chen, *Anomalous*

- Transport Properties and Phase Diagram of the FeAs-Based SmFeAsO<sub>1-x</sub>F<sub>x</sub> Superconductors*, Phys. Rev. Lett. **101**, 087001 (2008).
- [121] K. Haule, J. H. Shim, and G. Kotliar, *Correlated Electronic Structure of LaO<sub>1-x</sub>F<sub>x</sub>FeAs*, Phys. Rev. Lett. **100**, 226402 (2008).
- [122] C. Cao, P. J. Hirschfeld, and H.-P. Cheng, *Proximity of antiferromagnetism and superconductivity in LaFeAsO<sub>1-x</sub>F<sub>x</sub>: Effective Hamiltonian from ab initio studies*, Phys. Rev. B **77**, 220506(R) (2008).
- [123] F. Ma and Z.-Y. Lu, *Iron-based layered compound LaFeAsO is an antiferromagnetic semimetal*, Phys. Rev. B **78**, 033111 (2008).
- [124] D. J. Singh and M.-H. Du, *Density Functional Study of LaFeAsO<sub>1-x</sub>F<sub>x</sub>: A Low Carrier Density Superconductor Near Itinerant Magnetism*, Phys. Rev. Lett. **100**, 237003 (2008).
- [125] L. Boeri, O. Dolgov, and A. A. Golubov, *Is LaFeAsO<sub>1-x</sub>F<sub>x</sub> an Electron-Phonon Superconductor?*, Phys. Rev. Lett. **101**, 026403 (2008).
- [126] T. Yildirim, *Origin of the 150-K Anomaly in LaFeAsO: Competing Antiferromagnetic Interactions, Frustration, and a Structural Phase Transition*, Phys. Rev. Lett. **101**, 057010 (2008).
- [127] Z. P. Yin, S. Lebegue, M. J. Han, B. P. Neal, S. Savrasov, and W. E. Pickett, *Electron-Hole Symmetry and Magnetic Coupling in Antiferromagnetic LaFeAsO*, Phys. Rev. Lett. **101**, 047001 (2008).
- [128] I. I. Mazin, M. D. Johannes, L. Boeri, K. Koepernik, and D. J. Singh, *Problems with reconciling density functional theory calculations with experiment in ferropnictides*, Phys. Rev. B **78**, 085104 (2008).
- [129] I. I. Mazin and M. D. Johannes, *A key role for unusual spin dynamics in ferropnictides*, cond-mat/ (2008), arXiv:0807.3737.
- [130] G. Giovannetti, S. Kumar, and J. van den Brink, *Mott state and quantum critical points in rare-earth oxypnictides RO<sub>1-x</sub>F<sub>x</sub>FeAs (R = La, Sm, Nd, Pr, Ce)*, Physica B **403**, 3653 (2008).
- [131] I. I. Mazin, D. J. Singh, M. D. Johannes, and M. H. Du, *Unconventional Superconductivity with a Sign Reversal in the Order Parameter of LaFeAsO<sub>1-x</sub>F<sub>x</sub>*, Phys. Rev. Lett. **101**, 057003 (2008).
- [132] K. Kuroki, S. Onari, R. Arita, H. Usui, Y. Tanaka, H. Kontani, and H. Aoki, *Unconventional Pairing Originating from the Disconnected Fermi Surfaces of Superconducting LaFeAsO<sub>1-x</sub>F<sub>x</sub>*, Phys. Rev. Lett. **101**, 087004 (2008).
- [133] G. Xu, H. Zhang, X. Dai, and Z. Fang, *Electron-hole Asymmetry and Quantum Critical Point in Hole-doped BaFe<sub>2</sub>As<sub>2</sub>*, cond-mat/ 0807.1401 (2008).

- [134] N. D. Mathur, F. M. Grosche, S. R. Julian, I. R. Walker, D. M. Freye, R. K. W. Haselwimmer, and G. G. Lonzarich, *Magnetically mediated superconductivity in heavy fermion compounds*, Nature **394**, 39 (1998).
- [135] T. Moriya and K. Ueda, *Antiferromagnetic spin fluctuation and superconductivity*, Rep. Prog. Phys. **66**, 1299 (2003).
- [136] P. Monthoux, D. Pines, and G. G. Lonzarich, *Superconductivity without phonons*, **450**, 1177 (2007).
- [137] P. Quebe, L. J. Terbuhte, and W. Jeitschko, *Quaternary rare earth transition metal arsenide oxides RTAsO ( $T = \text{Fe, Ru, Co}$ ) with ZrCuSiAs type structure*, J. Alloys Compd. **302**, 70 (2000).
- [138] S. Lebègue, *Electronic structure and properties of the Fermi surface of the superconductor LaOFeP*, Phys. Rev. B **75**, 035110 (2007).
- [139] H.-H. Wen, G. Mu, L. Fang, H. Yang, and X. Zhu, *Superconductivity at 25K in hole-doped ( $\text{La}_{1-x}\text{Sr}_x$ )OFeAs*, Europhys. Lett. **82**, 17009 (2008).
- [140] K. Uchida, J. Xiao, H. Adachi, J. Ohe, S. Takahashi, J. Ieda, T. Ota, Y. Kajiwara, H. Umezawa, H. Kawai, G. E. W. Bauer, S. Maekawa, and E. Saitoh, *Spin Seebeck insulator*, Nature Materials **9**, 894 (2010).
- [141] C. M. Jaworski, J. Yang, S. Mack, D. D. Awschalom, J. P. Heremans, and R. C. Myers, *Observation of the spin-Seebeck effect in a ferromagnetic semiconductor*, Nature Materials **9**, 898 (2010).
- [142] F. L. Bakker, A. Slachter, J.-P. Adam, and B. J. van Wees, *Interplay of Peltier and Seebeck Effects in Nanoscale Nonlocal Spin Valves*, Phys. Rev. Lett. **105**, 136601 (2010).
- [143] T. Valet and A. Fert, *Theory of the perpendicular magnetoresistance in magnetic multilayers*, Phys. Rev. B **48**, 7099 (1993).
- [144] M. Johnson and R. H. Silsbee, *Thermodynamic analysis of interfacial transport and of the thermomagnetolectric system*, Phys. Rev. B **35**, 4959 (1987).
- [145] H. B. Callen, *Thermodynamics*, Wiley, New York Sec. 17.6 (1960).
- [146] N. W. Ashcroft and N. D. Mermin, *Solid State Physics*, Thomson Learning (1976).

# Summary

Oxide interfaces and ultrathin films exhibit new physical phenomena, which do not exist in corresponding bulk materials. What are the origins of the phenomena? To answer this question is the initial motivation of our research. As stated in Chapter 1, our research follows a strategy. First, we obtain a thorough and comprehensive understanding of the bulk materials; second, we figure out an instability of the interfaces and ultrathin films; third, we propose new states that can resolve the instability and lead to the new physical phenomena.

In the case of LAO thin films grown on STO substrates, the polar discontinuity at the LAO|STO interface will induce a large internal electric field, leading to a polar instability of the whole system. All theoretical studies in literature (including our DFT calculations in chapter 3) agree that charge transfer is one way to compensate the internal electric field and resolve the instability. However, it is not an energetically favorable way, as we stated in Chapter 4. We find that formation of oxygen vacancies will be a more energetically favorable way to stabilize the system. Our finding suggests that the LAO|STO interfaces can not be ideal, and formation of oxygen vacancies or other defects should be included. Following this logic, in Chapter 6 we predict a novel chain-type structure of SrCuO<sub>2</sub> ultrathin films. This structure is observed by some preliminary experiments of IMS group.

In Chapter 5 we propose GdFeO<sub>3</sub>-like rotation of TiO<sub>6</sub> octahedra at the n-type interface between cubic perovskite LAO and STO. The rotation results in a new characteristic buckling of the Ti-O-Ti bonding at the interface, which has been observed by a recent transmission electron microscopy experiment (Jia *et al.* [50]).

In Chapter 7 we identify a magnetic phase diagram of La[O<sub>1-x</sub>F<sub>x</sub>]FeAs as a function of three key parameters: the doping  $x$ , the FeAs in-plane lattice constant  $a$ , and the distance  $d$  between the Fe and As planes. The undoped parent compound LaOFeAs is a poor metal with a stripe antiferromagnetic (AFM) ground state but with increasing F doping a transition to a checkerboard AFM or non-magnetic ground state occurs. The magnetic transition can be understood in terms of density of states of the parent compound close to the Fermi level.

In Chapter 8, we find that a thermally induced magnetization gradient will give rise to an effective long-range spin motive force  $H^*$  in terms of entropy production. We find that (1)  $H^*$  critically depends on the thermodynamic and statistical properties of specific materials; (2) spin flip scattering can not suppress  $H^*$ . Our results probably explain the spin Seebeck effect.



# Acknowledgements

I would like to acknowledge all those who made it possible for me to complete this thesis.

First of all, I would like to express my sincere gratitude to my supervisor, Prof. Paul J. Kelly, for your continuous guidance and support throughout my Ph.D study. Thank you, Paul. I learned from you what is good science and how to be a good scientist. Your comments on various scientific topics are always insightful. Your serious attitude to science is very impressive; I still remember once you complained about my results, “*the bandwidth in your figure is 2.1eV, instead of 2 eV, according to my ruler*”. I hope I will be an O.K.Andersen-type scientist as you are. More importantly, I learned from you how to write a scientific paper. Your comments and suggestions on my manuscripts are very helpful, and sometimes they are even longer than the manuscripts themselves. I also would like to thank you and your wife Andrea for the new year parties in your house.

Geert Brocks, thank you for interesting discussions and remarks that helped me to clarify many scientific problems such as the double counting problem of LDA+U. Els, thank you for helping me a lot to deal with the Dutch and university bureaucracy. Usually, I come to your office and start our conversation, “*hello, Els, I need your help*”.

Qinfang and Pengxiang, my brothers in CMS, thank you for helping me and being my friends. I cherish our friendship; as Paul said, we are the Terrific Three. Danny, my belgian friend, thanks for your understanding and respect of chinese culture. I enjoyed our talks about science and life in China and Europe. Anton, thank you for solving my computer problems and keeping our cluster running efficiently. Menno, thank you for helping me to deal with dutch documents such as the application form of peuterspeelzaal for my daughter. Zhe and Yi, thank you for offering me a very useful thesis template, reading my manuscripts, and giving me many valuable suggestions and comments. Suleyman, thanks for sharing your successful experience in applying for postdoc fellowships. Deniz, thank you for our useful discussions about VASP. Diana, thank you for organizing CMS lectures, soccer matches, and Christmas dinners. Thijs, thanks for your helps in the Psi-k meeting in Berlin. New comers at the group, Rien, Elmer, Mojtaba, Taher, Omar, thank you for making the life so enjoyable. All CMSers, thanks for the good time we had together.

I would like to thank the members of IMS, ICE, NE, QEM groups who greatly helped me with discussions, advices and new ideas. I would like to thank Gertjan Koster, Guus Rijnders, Mark Huijben, Hans Boschker, Josee Kleibeuker, Gerwin

## Acknowledgements

---

Hassink, Hajo Molegraaf, Michelle Kruize, Jeroen Blok, Bouwe Kuiper, Alexander Brinkman, Hans Hilgenkamp, M. van Zalk, Sander Wenderich, Wilfred Wiel, Erik Slooten, and Mark Golden. I also would like to thank Jeroen van den Brink for discussion about FeAs-based superconductors and thank Gerrit Bauer for discussion about the spin Seebeck effect.

Many thanks to my friends that I met during my stay in Twente. Mingliang and Lingling, my badminton mentor and my friends, thank you for teaching me how to play badminton. I am very lucky to have you two as my friends. Making friends with you, I have incredibly improved my social ability (because of Mingliang's talkative ability?). Li Nan and Liu Jun, thanks for playing badminton and Wii together. We are the best Man's double in Twente (Mingliang may disagree). Thanks Liu Jun for the delicious "egg+rice". Li Chen and Yuanyuan, thanks for good trips and dinners we had together. I still hope I can get the chance to show my cooking ability. Jiwu and yanbo, thanks for being my friends.

Finally, Yanhui, I would like to thank you deep in my heart for giving me the most valuable the biggest support I could get. Taking care of our two daughters is a much tougher task than writing a thesis.

# List of publications

1. *Electronic-structure-induced reconstruction and magnetic ordering at the  $\text{LaAlO}_3|\text{SrTiO}_3$  interface*  
**Zhicheng Zhong\*** and Paul J. Kelly  
Euro. Phys. Lett. 84, 27001 (2008). (Cited~30; EPL Best of 2009 collection)
2. *Polarity-induced oxygen vacancies at  $\text{LaAlO}_3|\text{SrTiO}_3$  interfaces*  
**Zhicheng Zhong\***, P. X. Xu, and Paul J. Kelly  
Phys. Rev. B 82, 165127 (2010)
3. *Prediction of thickness limits of ideal polar ultrathin films*  
**Zhicheng Zhong\***, G. Koster, and Paul J. Kelly  
(submitted to Phys. Rev. Lett.)
4. *Magnetic phase diagram of FeAs based superconductors*  
**Zhicheng Zhong\***, Qinfang Zhang, P. X. Xu, and Paul J. Kelly  
arXiv:0810.3246v1
5. *Understanding the spin Seebeck effect*  
**Zhicheng Zhong\***, Z. Yuan, and Paul J. Kelly  
(in preparation)
6. *Internal electric field in  $\text{SrTiO}_3|\text{LaAlO}_3$  heterostructures probed with HAX-PES and DFT calculations*  
E. Slooten, **Zhicheng Zhong**, H. Molegraaf, S. de Jong, F. Masee, E. van Heumen, M. Gorgoi, G. Rijnders, D. Blank, M. Huijben, Paul. J. Kelly, and M. S. Golden  
(to be submitted)
7. *Correlation driven metal insulator transition as a function of thickness in  $\text{SrRuO}_3$  films*  
Wolter Siemons, Jeroen Blok, **Zhicheng Zhong**, Paul J. Kelly, Guus Rijnders, Dave H. A. Blank, and Gertjan Koster  
(to be submitted)



## List of publications

---

8. *Electrostatic doping of graphene through ultrathin hexagonal boron nitride films*

Menno Bokdam, Petr A. Khomyakov, Geert Brocks, **Zhicheng Zhong**, and Paul J. Kelly

Nano Letter (accepted)

9. *Enhancement of polarization in a spin-orbit coupling quantum wire with a constriction*

Jun-Feng Liu, **Zhicheng Zhong**, Lei Chen, Dingping Li, Chao Zhang, and Zhongshui Ma

Phys. Rev. B 76, 195304 (2007)

\* the corresponding author

# Curriculum vitae



Name: Zhicheng Zhong  
Date of birth: Dec 18<sup>th</sup> 1982  
Nationality: P. R. China  
Date of Ph.D: Oct 12<sup>th</sup> 2011 (Expected)

## Education

- 2005-2011 Ph.D. in Theoretical Solid State Physics,  
University of Twente, Enschede, the Netherlands  
Thesis: “*Instability, the driving force for new physical phenomena*”  
Supervisor: Prof. Paul J. Kelly
- 2002-2005 Master of Science in Condensed Matter Theory,  
Peking University, Beijing, P.R. China  
Thesis: “*Electronic transport in a spin-orbit coupling quantum wire with a constriction*”
- 1998-2002 Bachelor of Science in Applied Physics,  
Special Class for the Gifted Young,  
Shanghai Jiaotong University, Shanghai, P.R. China.